Sevda Abadpour

Modeling Backscattering Behavior of Vulnerable Road Users Based on High-Resolution Radar Measurements

SKIT Scientific Publishing

Sevda Abadpour

Modeling Backscattering Behavior of Vulnerable Road Users Based on High-Resolution Radar Measurements

Karlsruher Forschungsberichte
aus dem Institut für Hochfrequenztechnik und Elektronik

Herausgeber: Prof. Dr.-Ing. Thomas Zwick
Prof. Dr. Ing. Ahmet Cagri Ulusoy

Band 103

Modeling Backscattering Behavior of Vulnerable Road Users Based on High-Resolution Radar Measurements

by
Sevda Abadpour

Karlsruher Institut für Technologie
Institut für Hochfrequenztechnik und Elektronik

Modeling Backscattering Behavior of Vulnerable Road Users
Based on High-Resolution Radar Measurements

Zur Erlangung des akademischen Grades einer Doktorin der
Ingenieurwissenschaften von der KIT-Fakultät für Elektrotechnik und
Informationstechnik des Karlsruher Instituts für Technologie (KIT)
genehmigte Dissertation

von Sevda Abadpour, M.Sc.

Tag der mündlichen Prüfung: 18. Juli 2023
Hauptreferent: Prof. Dr.-Ing. Thomas Zwick
Korreferent: Prof. Dr.-Ing. Nils Pohl

Editor's Preface

An accurate perception and recognition of the vehicle environment by sensors is one of the keys to safe autonomous driving. Radar sensors play an essential role here, as radar provides good images independent of weather and light conditions. Radar technology is thus ideally suited, in conjunction with optical sensors such as cameras and lidar sensors, to provide good coverage of the vehicle environment at all times. State-of-the-art radar systems have a high resolution in terms of distance and Doppler, but the lateral resolution is, due to physical constraints, significantly lower than that of optical systems. Consequently, this challenge is an essential part of current research and development. On the other hand, the knowledge about the radar backscattering of objects in road traffic is insufficient for the new upcoming radar systems with increased lateral resolution. Only measurements that characterize the objects as an overall target exist. However, since novel radar sensors are capable of resolving cars and even two-wheeled vehicles and pedestrians laterally into more than a single pixel, higher-resolution backscatter models of these traffic objects are needed. This is exactly where the work of Dr.-Ing. Sevda Abadpour comes in. In her dissertation, Ms. Abadpour has developed important scientific principles for high-resolution radar measurement and modeling of objects in road traffic scenarios. The work is based on a high-resolution RCS measurement system and is primarily dedicated to the most vulnerable road users, pedestrians, and two-wheelers. Her RCS measurement system with mechanical angular scanning has an aperture angle of $1.3°$. Since the measurements are extremely time-consuming and are also susceptible to unintentional movements of the object under test, they were carried out with people and a dummy. It could be shown that the dummy represents reality very well, which makes the generation of extensive measurement data much easier. The extensive measurement campaigns carried out as part of this work provide a valuable basis for developing future radar systems for autonomous driving. In additional measurement campaigns, dynamic measurements of moving pedestrians were performed. This made it possible to assign realistic RCS values to the separately moving scattering cen-

ters of the persons for the first time. In her work, Dr. Sevda Abadpour presents important RCS measurement results of vulnerable road users. I am sure that her work will draw much attention in the autonomous driving and radar sensor community worldwide. For Dr. Abadpour, with her broad technical skills, I wish her further much success in her career.

Prof. Dr.-Ing. Dr. h.c. Thomas Zwick

- Institute Director -

Zusammenfassung

Bei der Weiterentwicklung der Technologie des autonomen Fahrens (AD) ist die Beschaffung zuverlässiger dreidimensionaler Umgebungsinformationen eine unverzichtbare Aufgabe, um ein sicheres Fahren zu ermöglichen. Diese Herausforderung kann durch den Einsatz von Fahrzeugradaren zusammen mit optischen Sensoren, z. B. Kameras oder Lidars, bewältigt werden, sei es in der Simulation oder in konventionellen Tests auf der Straße. Das Betriebsverhalten von Fahrzeugradaren kann in einer Over-the-Air (OTA) Vehicle-in-the-Loop (ViL) Umgebung genau bewertet werden. Für eine umfassende experimentelle Verifizierung der Fahrzeugradare muss jedoch die Umgebung, insbesondere die gefährdeten Verkehrsteilnehmer (VRUs), möglichst realistisch modelliert werden. Moderne Radarsensoren sind in der Lage, hochaufgelöste Erkennungsinformationen von komplexen Verkehrszielen zu liefern, um diese zu verfolgen. Diese hochauflösenden Erkennungsdaten, die die reflektierten Signale von den Streupunkten (SPs) der VRUs enthalten, können zur Erzeugung von Rückstreumodelle genutzt werden.

Darüber hinaus kann ein realistischeres Rückstreumodell der VRUs, insbesondere von Menschen als Fußgänger oder Radfahrer, durch die Modellierung der Bewegung ihrer Extremitäten in Verkehrsszenarien erreicht werden. Die Voraussetzung für die Erstellung eines solchen detaillierten Modells in verschiedenen Situationen sind der Radarquerschnitt (RCS) und die Doppler-Signaturen, die sich aus den menschlichen Extremitäten in einer bewegten Situation ergeben. Diese Daten können durch die gesammelten Radardaten aus hochauflösenden RCS-Messungen im Radial- und Winkelbereich gewonnen werden, was durch die Analyse der Range-Doppler-Spezifikation der menschlichen Extremitäten in verschiedenen Bewegungen möglich ist. Die entwickelten realistischen Radarmodelle können bei der Wellenausbreitung im Radarkanal, bei der Zielerkennung und -klassifizierung sowie bei Datentrainingsalgorithmen zur Validierung und Verifizierung der Kfz-Radarfunktionen eingesetzt werden.

Anschließend kann mit dieser Bewertung die Sicherheit von fortschrittlichen Fahrerassistenzsystemen (ADAS) beurteilt werden.

Daher wird in dieser Arbeit ein hochauflösendes RCS-Messverfahren vorgeschlagen, um die relevanten SPs verschiedener VRUs mit hoher radialer und winkelmäßiger Auflösung zu bestimmen. Eine Gruppe unterschiedliche VRUs wird in statischen Situationen gemessen, und die notwendigen Signalverarbeitungsschritte, um die relevanten SPs mit den entsprechenden RCS-Werten zu extrahieren, werden im Detail beschrieben. Während der Analyse der gemessenen Daten wird ein Algorithmus entwickelt, um die physischen Größen der gemessenen Testpersonen aus dem extrahierten Rückstreumodell zu schätzen und sie anhand ihrer Größe und Statur zu klassifizieren. Zusätzlich wird ein Dummy-Mensch vermessen, der eine vergleichbare Größe wie die vermessenen Probanden hat. Das extrahierte Rückstreuverhalten einer beispielhaften VRU-Gruppe wird für ihre verschiedenen Typen ausgewertet, um die Übereinstimmung zwischen virtuellen Validierungen und der Realität aufzuzeigen und den Genauigkeitsgrad der Modelle sicherzustellen. In einem weiteren Schritt wird diese hochauflösende RCS-Messtechnik mit der Motion Capture Technologie kombiniert, um die Reflektivität der SPs von den menschlichen Körperregionen in verschiedenen Bewegungen zu erfassen und die Radarsignaturen der menschlichen Extremitäten genau zu schätzen. Spezielle Signalverarbeitungsschritte werden eingesetzt, um die Radarsignaturen aus den Messergebnissen des sich bewegenden Menschen zu extrahieren. Diese nachbearbeiteten Daten ermöglichen es der Technik, die zeitlich variierenden SPs an den Extremitäten des menschlichen Körpers mit den entsprechenden RCS-Werten und Dopplersignaturen einzuführen. Das extrahierte Rückstreumodell der VRUs enthält eine Vielzahl von SPs. Daher wird ein Clustering-Algorithmus entwickelt, um die Berechnungskomplexität bei Radarkanalsimulationen durch die Einführung einiger virtueller Streuzentren (SCs) zu minimieren. Jedes entwickelte virtuelle SCs hat seine eigene spezifische Streueigenschaft.

Abstract

During the evolvement of autonomous driving technology, obtaining reliable three-dimensional environmental information is an indispensable task in approaching safe driving. This challenge can be confronted by utilizing automotive radars together with optical sensors, e.g., cameras or lidars, either in simulation or conventional real-road testing. The operational behavior of automotive radars can be precisely evaluated in an over-the-air vehicle-in-the-loop environment. However, a comprehensive experimental verification of the automotive radars requires modeling its surrounding, specifically vulnerable road users (VRUs), as realistic as the real test environment. Advanced radar sensors are able to deliver highly resolved detection and recognition information from complex traffic targets to track them. These high-resolution detection data, containing the reflected signals from the scattering points of VRUs, can generate their backscattering models.

Furthermore, a more realistic backscattering model of the VRUs, especially humans as pedestrians or bikers, can be achieved by modeling the movement of their extremities in traffic scenarios. The prerequisite for generating such a detailed model in different situations is the radar cross section (RCS) and Doppler signatures of a human in motion. This information can be retrieved by the collected radar data from high-resolution RCS measurements in the radial and angular domains, which is attainable after analyzing the range-Doppler specification of human extremities in various motions. The developed realistic radar models can be employed in radar channel wave propagation, target recognition and classification, and data training algorithms for the validation and verification of automotive radar functionality. Subsequently, this evaluation can assess the safety of advanced driver assistance systems.

This thesis proposes a high-resolution RCS measurement technique to determine the relevant scattering points of different VRUs with high radial and angular resolution. A diverse group of VRUs is measured in static situations, and necessary signal processing steps are described in details to extract the

relevant scattering points with corresponding RCS values. During this analysis of the measured data, an algorithm is developed to estimate the physical sizes of the measured test persons from the extracted backscattering model and classify them based on their size and stature. Additionally, a dummy human is measured, which has a comparable size to one of the measured test persons. The extracted backscattering behavior of an exemplary VRU group is evaluated for its different types to indicate the consistency between virtual validations and reality and ensure the accuracy level of the models. In a later step, this high-resolution RCS measurement technique is combined with motion capture technology to collect the reflectivity of the scattering points from the human body regions in different motions and accurately estimate radar signatures of human extremities. Dedicated signal processing steps are utilized to extract the radar signatures from the measurement results of the human in motion. This post-processed data enables the technique to introduce the time-varying scattering points on the human body's extremities with the corresponding RCS values and Doppler signatures. The extracted backscattering model of VRUs contains a plurality of scattering points. Thus, a clustering algorithm is developed to minimize computational complexity in radar channel simulations by introducing some virtual scattering centers. Each developed virtual scattering center has its own specific scattering characteristic. Finally, the key achievements of this thesis are summarized.

Acknowledgement

I would like to express my gratitude and appreciation to my supervisor and the head of the institute, Prof. Dr.-Ing. Dr. h.c. Thomas Zwick. His continuous guidance, invaluable advice, and overall insights in this field have made this journey a wonderful experience for me. He was always willing and enthusiastic to help throughout the research project, as well as professional and personal life.

I am also pleased to say thank you to Prof. Dr. Ing. Nils Pohl for being my examiner. His research and publications were always sources of inspiration to me. It was a great pleasure to have him on the examination committee. I would especially thank him and his team, at Institute for Integrated Systems at Ruhr-University Bochum, for providing the radar sensor. I am genuinely grateful to him and his team for investing their valuable time.

Furthermore, I would thank Dr.-Ing. Mario Pauli and M.Sc. Sören Marahrens for the nice teamwork and M.Sc. Theresa Antes, for reviewing my dissertation and for constructive critique on this topic. I am deeply grateful to Dr. Christian Schyr from AVL Deutschland GmbH, Karlsruhe, for his dedicated support and guidance during our collaboration to establish a measurement setup from the combination of an automotive radar sensor and MoCap technology. Also, I would appreciate Mr. Martin Hennrich and Mr. Florian Klein from HHVision, Cologne, for supporting the measurement campaigns that utilized the MoCap technology and must be conducted in the motion Lab environment. I am thankful to Prof. Dr. Georg Müller from Institute for Pulsed Power and Microwave Technology (IHM) at Karlsruhe Institute of Technology (KIT) for providing the test environment. I also thank Mr. Joaquim Fortuny from European Microwave Signature Laboratory at the Joint Research Center of the European Commission, Ispra, Italy (JRC), for providing the anechoic chamber for RCS measurement.

This Ph.D. work was funded by the German Federal Ministry of Education and Research (BMBF) through the Virtuelle Validierung CAD Japan-Germany

Contents

Abbreviations and Symbols

Abbreviations

ADAS   Advanced Driver Assistance Systems

AD   Autonomous Driving

AoA   Angle of Arrival

BMBF   Bundesministerium für Bildung und Forschung

CAD   Computer Aided Design

CNN   Convolutional Neural Network

CL   Clutter Level

DCNN   Deep Convolutional Neural Network

EFE   Enhanced Frequency Evaluation

EM   Electromagnetic

Euro NCAP European New Car Assessment Program

FDTD   Finite-Difference-Time-Domain

FEM   Finite Element Method

FFT   Fast Fourier Transform

FMCW   Frequency-Modulated Continuous-Wave

FoV   Field of View

FOT	Field Operational Test
GANs	Generative Adversarial Networks
GO	Geometrical Optics
HiL	Hardware-in-the-Loop
HR	High-Resolution
HPBW	Half-Power Beamwidth
IEEE	Institute of Electrical and Electronics Engineers
IF	Intermediate Frequency
IHE	Institut für Hochfrequenztechnik und Elektronik
IHM	Institut für Hochleistungsimpuls- und Mikrowellentechnik
ISAR	Inverse Synthetic Aperture Radar
IMUs	Inertial Measurement Units
KIT	Karlsruher Institut für Technologie
MoM	Method of Moments
MoCap	Motion Capture technology
PO	Physical Optics
OUT	Object Under Test
OTA	Over-the-Air
PTFE	Polytetrafluoroethylene
RTS	Radar Target Simulator
RCS	Radar Cross Section
RCU	Radar Control Unit

RUB	Ruhr-Universität Bochum
SiGe	Silicon Germanium
SiL	Software-in-the-Loop
SNR	Signal to Noise Ratio
SLL	Sidelobe Level
SPs	Scattering Points
SC	Scattering Center
SCs	Scattering Centers
SP	Scattering Point
TCR	Trihedral Corner Reflector
UDP	User Datagram Protocol
ViL	Vehicle-in-the-Loop
VNA	Vector Network Analyzers
VRU	Vulnerable Road User
VRUs	Vulnerable Road Users
VCO	Voltage Control Oscillator
XiL	X-in-the-Loop
n-D	n Dimensional

Mathematical and Physical Constants

$\pi = 3.14159\ldots$ Archimedes' constant

$k = 1.380649 \times 10^{-23}\,\mathrm{J/K}$ Boltzmann's constant

$c_0 = 2.9991310^8\,\mathrm{m/s}$ Propagation speed of the EM wave in the air

Latin Symbols and Variables

Lower case

α	Ramp slope
β	Azimuthal rotation angle of VRU
θ	Radar system scanning angle in elevation direction
λ	Wavelength
ε_r	Relative permittivity
φ	Radar system scanning angle in azimuth direction
τ	Delay Time
a	Inner height of the TCR
f	Frequency
f_{if}	Intermediate frequency
$f_{\mathrm{if,max}}$	Maximum intermediate frequency
$f_{\mathrm{if,min}}$	Minimum intermediate frequency
f_b	Beat frequency
f_D	Doppler frequency
h	Head height of the person under test
t	Time
w_h	Head width of the person

(x_R'', y_R'', z_R'') Extracted coordinates of right side of the human body region
under process

(x_L'', y_L'', z_L'') Extracted coordinates of left side of the human body region
under process

(x_i'', y_i'', z_i'') Extracted coordinates of ith scattering point in coordinate system
whose origin is the center of the object

Upper case

Δf Bandwidth

$\vec{C}_i$ Coordinates of the ith scattering point assuming the radar sensor
as the origin of the spherical coordinate system

$\vec{C}_i'$ Coordinates of the ith scattering point in coordinate system
whose origin is the center of the object

G Antenna Gain

H Height of test environment

H_{Meas} Estimated height of every human body region from the extracted
radar model

H_p Height of the person under study

L Length of test environment

N_{Meas} Measured noise level of the Radar system

NF Noise Figure

OL   Object list matrix

P Total number of the extracted scattering points

P_N Noise power at the receiver

P_{Rx} Received power

P_{Tx} Transmit power

R   Distance between the center of the object under test and the feed

	antenna
RCS_i	the measured RCS value for the ith extracted scattering point
$S_{Meas,i}$	Measured level of the signal in the place of the ith scattering point
SNR	Signal-to-Noise ratio of the Radar system
$SNR_{Meas,i}$	The measured Signal-to-Noise ratio for the ith scattering point
SP	Scattering point matrix
$\vec{SP}_i$	Coordinates of the ith scattering point in Cartesian coordinate system
T_{sweep}	Chirp Time of an FMCW signal
T_{abs}	Absolute temperature of the test environment
W	Width of test environment
W_{Meas}	Estimated width of every human body region from the extracted radar model

1 Introduction

1.1 Background and Motivation

It is well known that the validation and verification (V&V) process is of utmost importance to approaching safe driving in the field of autonomous driving (AD). Furthermore, the safety process of AD can be inherently ensured by the safety of vulnerable road users (VRUs), which necessitates a reliable perception and understanding of the environment. Therefore, the advanced driver assistance system (ADAS), including a set of incorporated cameras, lidars, and radar sensors, is embedded in self-driving vehicles to increase the safety requirements of AD systems. Among all the intelligent components of AD systems, the radar sensor has a key role in providing high-robustness data from the environment, especially against weather conditions. This data is not only effective in warning for AD systems but also evaluates their safe functionality.

Moreover, it is critical to ensure the robust, stable, and reliable functionality of the AD systems before releasing them. To assist this development, there is a high demand for virtual validation test approaches, X-in-the-Loop (XiL), before the on-road testing. XiL test approaches are different emulations of software and hardware under all contingencies. These emulation systems include software-in-the-loop (SiL), hardware-in-the-loop (HiL) simulations, and over-the-air (OTA) vehicle-in-the-loop (ViL).

However, the realistic results of the field operational tests (FOT) are worthwhile; this validation approach provides unsafe scenes for other traffic participants and requires a huge effort, e.g., several million kilometers of trial driving [MGLW15, KW16]. A further drawback of FOT is scarcely reproducible and controllable, especially with changing the automotive sensor configuration and software. In contrast with FOT, XiL validation test methods offer the capability of simulating traffic situations, even critical ones, in laboratory conditions. Subsequently, the real operation of the radar systems can be evaluated with

sufficient degrees of resilience and reliable conditions. A dedicated radar target simulator (RTS), like the one developed in [DKK+21, SSGW21], can generate multiple radial and angle-resolved targets to perform the emulation of standard and complex environments authentically. The detailed modeling of the real traffic targets, e.g., car, motorcycle, and VRUs, is an necessary prerequisite for developing such RTSs. Realistic target modeling demands the knowledge of the backscattering behavior of the targets to distribute their scattering points (SPs). Only in this case, the radar wave propagation result is comparable with the sensor response in the real environment.

Modeling the behavior of the VRUs in complex urban scenarios is essential in order to address the two accretive necessities, i.e., identify them in a timely manner and predict hazardous situations. It is worth emphasizing that the VRUs include different traffic participants, e.g., motorcyclists, cyclists, users of electric scooters, and, in particular, pedestrians [RMGI22, SMKM15]. Since the mentioned objects have an agile behavior in traffic scenarios, their motion modeling in the traffic scenarios must be done with the highest possible interdependence. Furthermore, the wave propagation simulation of traffic scenarios can approach more realistic results by implementing the accurate backscattering model of traffic participants in the simulation tools. It can be done by utilizing different numerical methods [CC14, SFGT+11, BE12, BE10, SBW08]. However, this entails a high-resolution CAD model and leads to a very high computational effort, and subsequently, the simulation cannot be done in real-time. The solution for approaching the accurate scattering model of VRUs is to execute high-resolution RCS measurements in radial, angular, and micro-Doppler domains, which can also speed up the simulations.

The current advancements in microwave technology enable automotive radars to collect high-accuracy and high-resolution data from the surrounding of the host vehicle by receiving multiple reflections per target and measurement cycles. These environmental data can be used for object detection, tracking, classification, and localization to generate an understanding of the environment in range, azimuth, elevation, and velocity domains. This means that the collected environmental data by the advanced automotive radar is in 4-D domain. Consequently, autonomous vehicles can perceive the traffic environment more realistically, consistently, and credible. A significant benefit of this type of data is developing a precise radar model of VRUs which shows their backscattering behavior similar to the real environment. Moreover, the unique accuracy of the collected data

from the radar measurement allows the development of radar models, including their micro-Doppler signatures. This type of extracted radar model can further improve image-based target classification methods together with the available methods based on mm-Wave radar data [CGS21,SHDW18,LYLK17,RKK+15]. The existing target classification approaches, with traditional and modern imaging radars, exploit the radar data, including distributed RCS data classification for traditional range-detection radar, Doppler signature analysis, 2-D range-azimuth angle radar images classification for radars capable of scanning in the azimuth direction, and 3-D radar images for radars with both azimuth and elevation direction beam-scanning ability. Further applications of the extracted radar models are in data training for machine learning methods, e.g., generative adversarial networks (GANs) [IADW18,EGA19,AOK19] and decision-making in the motion planning of automated vehicles. Another advantage of developing a high-resolution radar model for VRUs is terminating the safety gaps in the protection of VRUs, especially pedestrians [GKZ+20].

A higher authenticity in real traffic scenario simulations can be achieved by implementing radar models of the VRUs more precisely and highly resolved. Considering the large variety of potential VRUs and their different types in each group of VRUs, it is worth to investigate the radar models of the different VRUs. A further investigation of the backscattering behavior for different types of exemplary VRUs can provide a benchmark for modeling reality which prevents any failure and inaccuracy in the modeling process. This leads to a reduction of the residual risk related to the functionality of the radar models in wave propagation simulations and deep learning applications.

Moreover, it is of evident interest to develop the backscattering models for the VRUs, which include their motions, especially for pedestrians and bikers. These motions can be precisely observed with modern mm-Wave radar systems since human movements cause Doppler modulations in radar signatures [VDG03,PJM+14,SSM+17,ARMSF18,PHO+18,DFW18]. Developing radar models of human activities enables radar wave propagation simulations to thoroughly investigate the functionality of automotive radars, even in complex traffic situations [SKM+13]. The micro-Doppler signatures of human activities can be predicted based on the electromagnetic (EM) simulation and measurements, as reported in [PJM+12,PJ12,CLHW06,Che08,NZ15,SRV18,DHR+20]. However, this type of modeling entails excessive computational requirements, specifically in time-varying geometries, and it is not adequate to model the

motion of human extremities with angular resolutions. It should be noted that the optical motion capture facilities [PJM+12] can gather realistic data on movement in human extremities. Another drawback of the mentioned method in literature arises from not containing the multipath interactions across different parts of the human body regions and shadowing effects. Subsequently, these disadvantages reduce the authenticity of the methods. The high-resolution RCS measurement can address those issues by determining the SPs of human extremities with their corresponding RCS values and Doppler signatures in range and angular directions.

1.2   Scope and Objective of the Thesis

As discussed, preparing the 3-D model of the VRUs is critical to employ in wave propagation simulation of traffic scenarios. For this purpose, high-resolution RCS measurements are executed in radial, angular, and Doppler domains. The angular domain of this accurate model includes the different viewing angles of the VRU by the radar sensor and the angular scanning area of the radar in both azimuth and elevation directions. Addressing the discussed safety issues, this dissertation proposes a high-resolution RCS measurement technique to extract the highly resolved radar model of the VRUs. In this context, Chapter 2 presents the necessary fundamentals for reliably modeling VRUs in the virtual environment, i.e., radar wave propagation simulation based on geometrical optics (GO), ray-tracing techniques, and high-resolution RCS measurement techniques. Subsequently, Chapter 3 discusses the proposed high-resolution RCS measurement technique and the necessary calibration steps. This chapter also evaluates the measured RCS patterns of the VRUs which demonstrates only the integral value as a scattering behavior of the entire object.

Then, the signal processing steps for extracting the SPs from the collected measurement data are explained in Chapter 4. This chapter describes the dedicated radar measurements for the volunteer test persons of different sizes, a dummy human, a bicycle, a bicyclist, a motorcycle, a motorcyclist, and a typical car. These measurements are conducted to scan the VRUs at different viewing angles and different radar scanning angles. The extracted radar model of the measured VRUs is analyzed in this chapter. In the next step, the required signal processing chain is discussed to estimate the location of human body parts in

the measured radar models and approximate the physical sizes of measured test persons. Besides, the backscattering behavior of the measured human dummy is investigated in comparison with a test person of similar size. The last section of Chapter 4 investigates the measured radar models of a motorcyclist with three different types of motorcycles to realize the various number of high-resolution RCS measurements in each group of VRUs.

Chapter 5 begins with explaining the necessary fundamentals to extract the spatial distribution of the projected SPs of a human in motion and their corresponding accurate radar signatures. In the next step, the discussed high-resolution measurement setup is combined with the motion capture (MoCap) technology to collect the radar data of human movement in different situations. Then, the mandatory postprocessing steps on the collected radar raw data are presented and verified to extract the range-velocity radar signature of human motion accurately. As a proof of concept, the dedicated measurements are conducted on a test person with various movements. The person under test is dressed up in a MoCap suit with the attached MoCap trackers to different body regions. Then, the requisite calibration measurement and intended signal processing chain are described to approach reliable modeling of a human in motion. Finally, this chapter investigates the extracted radar signature of human activities, i.e., range-velocity information, to utilize it in the backscattering modeling of human motions and develop a highly realistic model.

In Chapter 6, this dissertation is followed by proposing a clustering algorithm for summarizing the extracted radar models from the high-resolution measurement results. Accordingly, the backscattering behavior of VRUs is presented by the virtual scattering centers (SCs) and their corresponding RCS specifications. The introduced virtual scattering models can be employed in wave propagation simulation to minimize the computational effort. It is demonstrated that the proposed algorithm can also be applied to the plurality of SPs, which is gathered by RCS simulations in ray-tracing tools. Chapter 7 concludes with a brief discussion on the achievement of this work. Figure 1.1 shows the workflow of the dissertation and also summarizes the application of the extracted radar models for developing highly realistic models.
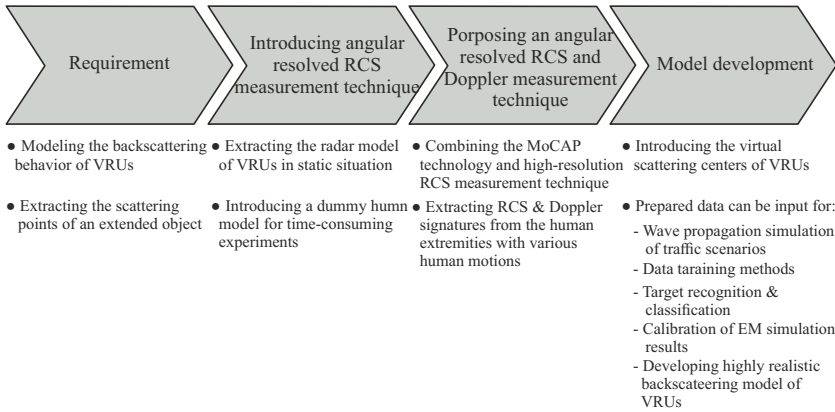
Figure 1.1: Block diagram of the workflow in this dissertation to obtain the backscattering behavior of the radar targets. It also shows the applications of the extracted radar signatures for model development.

2 Fundamentals

2.1 Radar Channel Wave Propagation Simulation

Knowledge of wave propagation phenomena in traffic scenarios is crucial to determine the propagation channel characteristics in real traffic scenes. For this purpose, the radar responses must be investigated according to the virtual scenarios in an environmental simulation [MMH18]. The EM wave propagation modeling in radar channels can be approximated based on different numerical methods, e.g., the method of moments (MoM), the finite-difference-time-domain (FDTD) method, and the finite element method (FEM) [AJG00, MMH18, SBW08]. However, the mentioned numerical methods involve a high discretization of the environment, taking into account the working frequency of the automotive radar sensors at the range of 76-81 GHz. Consequently, the radar targets and simulation environment are considered electrically large objects, which cause pretty large requirements and computational time.

A physical optics (PO) approach [DSWW00] is used in the form of several ray-based methods to address this issue and model the EM wave propagation in complex environments. The proposed ray-based techniques include ray-tracing [Gla89, ZFW02], ray-launching [ZHK98], imaging [Rem93, Kle93, MLD94], or a combination of ray launching and imaging [CJ95, CJ96]. These proposed ray optical methods can analyze the reflections at the plane boundaries, either rectangular sections or tessellate the complex structures into many polygons [CJ96, HCC98]. Development in ray-optical methods makes it possible to calculate the EM fields coherently without restriction in the structure of the surface under analysis and also model the multipath reflections [Mau05, FMKW06, SW09, CH02]. The geometrical optics (GO) is exploited for modeling the environment and radar targets [Bal12].

In more advancement, a hybrid approach can be proposed, which implements the scattering process of the radar targets in a ray-tracing simulation tool to

approach an accurate analysis of the radar channels and, concurrently, a real-time wave propagation. Additionally, the characterization of radar targets, based on their back-scattering behavior, can obtain realistic wave propagation results [PTWM17].

2.2 Radar Target Characterization in Wave Propagation Simulations

It is important to characterize the radar targets for modeling in wave propagation simulations as realistic as the real test environment. For this purpose, the radar targets must be described by scattered EM waves from the illuminated dielectric or metallic body of the targets. The amount of this scattering phenomenon is typically represented by the RCS value, which is the level of the scattered power in a considered direction after impinging by a plane wave. Figure 2.1 shows the geometry of the scattering process when the transmitter of the radar (Tx) illuminates its target by a plane wave, and the reflected signals are collected by the receiver antenna (Rx) at the distance of r_{Rx}. The schematic is depicted as a bistatic radar arrangement. The scalar RCS value of the target in a specified direction can be calculated by the ratio of the scattered power to the incident power per unit solid angle when the target is located in the far field [Bal05]. Therefore,

$$
\text{RCS} = \lim_{r_{Rx} \to \infty} 4\pi r_{Rx}{}^2 \frac{\left\| \vec{E}_s \right\|^2}{\left\| \vec{E}_i \right\|^2}
\tag{2.1}
$$

where $\vec{E}_s$ is the scattered EM field of the target after being affected by the incident field of $\vec{E}_i$.

Equation 2.1 calculates the scalar value of the RCS without considering the influence of wave polarization and phases. The mentioned effects can be considered by calculating the complex scattering matrix [WG98]. The scalar RCS value can be computed by Equation 2.1 for simple shaped 2-D radar targets,
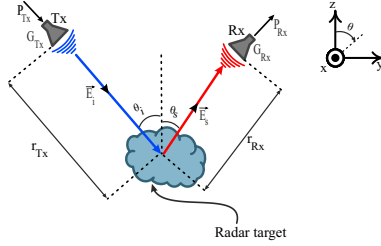
Figure 2.1: Schematic of scattering process for derivation of RCS from the radar target with arbitrary shape. The transmission process, including transmitted (blue) and received (red) signals, and coordinate system are demonstrated.

although it is more complicated for complex 3-D radar targets. The prediction of overall scattered power from a complex target is difficult since it includes different backscattering phenomena, i.e., specular reflection, energy diffraction from the corners, and creeping waves and resonant parts of the target [WG98, Bal12]. Accordingly, the theoretical RCS estimation for the complex targets requires an intricate calculation which makes it impracticable [LKKL16]. Thereby, it becomes imperative to prepare a RCS measurement facility for the targets with different sizes and shapes, which can collect the scattering data of the target at various viewing angles.

The scattering phenomena of complex radar targets can be also explained by the radar equation for the bistatic case [Bal05] as

$$P_{Rx} = \frac{P_{Tx} G_{Tx} G_{Rx} \lambda^2}{(4\pi)^3 \, r_{Tx}^2 \, r_{Rx}^2} RCS \tag{2.2}$$

where P_{Rx} is the received power by the radar, P_{Tx} is the transmit power, G_{Rx} is the antenna gain of the receiver, λ is the wave length, r_{Tx} is the distance between the Tx antenna and target, and r_{Rx} is the distance between the Rx antenna and target. For a monostatic radar[1], the target is observed at same

---

[1] Transmitter and receiver are juxtaposed.

direction of incident wave and the same antenna is configured for transmission and reception. That means,

$$
\begin{aligned}
r_{Tx} &= r_{Rx} = R, \\
G_{Tx} &= G_{Rx} = G.
\end{aligned}
\tag{2.3}
$$

Since, a monostatic radar configuration is mostly utilized in mm-wave automotive radar applications, therefore it is useful to evaluate the received power by the sensor. For the monostatic case, P_{Rx} can be described by comparing Equations 2.2 and 2.3 as

$$
P_{Rx} = \frac{P_{Tx} G^2 \lambda^2}{(4\pi)^3 \, R^4} RCS.
\tag{2.4}
$$

It should be noted that the calculated RCS values in the monostatic case are usually referred to as a normalized backscattering coefficient [GD07], which can be computed by calibration measurements for standard radar targets. Furthermore, the RCS calculation is considered on the effective cross-sectional surface of the target; therefore, it is reported in units of dBsm.

2.3 RCS Measurement Techniques

The scattering data from the radar targets can be obtained with a dedicated measurement setup which is the purpose of RCS measurements. In this measurement setup, the target should be located in a range where the incident wave can achieve an acceptable plane wave uniformity. Then, the EM signals of desired frequency have to be generated for incident radiation on the target under measurement. The receiver antenna collects the backscattered waves from the target to store the data for later postprocessing and detect the target. In high-frequency applications, a transceiver is embedded in the EM wave radiation instrument to utilize the up and down conversion principle. The radar targets are illuminated under different viewing angles in the real application of automotive radar. Therefore it is mandatory to collect the scattering data of the

target from its various viewing angles. A rotating stage enables the measurement setup to emulate all possible target orientations. In addition to the test objects, the standard calibration targets, e.g, sphere and corner reflector, are required for normalization measured RCS values and characterization the test environment. The RCS values of the standard radar targets can be calculated analytically [RSH10]. Figure 2.2 shows a schematic of a typical RCS measurement setup in the anechoic chamber in which the unwanted reflected EM waves from the test environment are attenuated to a specific level.
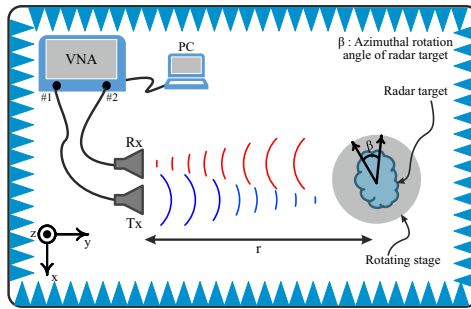

Figure 2.2: Schematic of a basic RCS measurement setup. The EM wave is produced by VNA and the transmitted and received signals are indicated with blue and red color, respectively.

The conventional approach for the EM wave generation in the RCS measurements uses either vector network analyzers (VNA) or radar sensors. Utilizing the VNA in the measurement setup enables measurement data acquisition, including the phase and polarization information in a laboratory environment. Accordingly, these measurement results can introduce the complex RCS matrix.

The RCS of the target is conventionally analyzed based on different parameters, i.e., down-range distance, cross-range distance, the radar viewing angle, and the radar transmitting frequency [Tic90]. For time-varying targets, the movement of the target causes geometrical changes, which consequently gives rise to fast variation in the RCS values of the target. The dynamic effect of the RCS values cannot be measured with the classical measurement methods which use the VNA since it necessitates a long measurement time [LKKL16, BGSC10]. Furthermore, frequency-modulated continuous wave (FMCW) is the utilized modulation technique in automotive radar applications. Using FMCW radar

11

systems, which continuously transmit several successive EM waves, enables to sample the fast variations of the target under test. In this context, the next sections describe the calculation of the parameters for the RCS calculation from the measurement data with an FMCW radar.

2.3.1   Signal to Noise Ratio calculation of an FMCW Radar

According to the principle and implementing procedure of FMCW radar, the received power (P_{Rx}) can be computed using the signal-to-noise ratio (SNR) of the radar [Sko01, TEV13]. The SNR is defined as

$$\text{SNR} = \frac{P_{Rx}}{P_N} \tag{2.5}$$

where P_N is the noise power. P_N for an FMCW radar is

$$P_N = \frac{k \, T_{abs} \, \text{NF}}{T_{Sweep}} \tag{2.6}$$

where k is the Boltzmann's constant, T_{abs} is the absolute temperature of the test environment, NF is the noise figure of the sensor, and T_{Sweep} is the chirp time. In the FMCW radar, the RCS value of the radar target can be calculated from the received signal. The power received by the sensor is described by the radar equation for the monostatic case in Equation 2.4 and can be calculated using the SNR of the radar sensor where P_N is the noise power at the receiver.

2.3.2   Range and Doppler Estimation Using FMCW Radar

Nowadays, SiGe semiconductor technology facilitates the realization of compact ultra-wideband radar transceivers in the millimeter-wave (mm-wave) band [PRM+09, PJA12]. This high carrier frequency radar can achieve the highest resolution at reasonable costs, which enables high precision distance and movement determination, enhanced target recognition, and higher ranging reso-

lution [AWE22]. In this context, a monostatic FMCW (frequency-modulated continuous wave) radar sensor is utilized to measure the range and Doppler of the radar targets in this work. This section provides a brief theoretical overview of FMCW radars to determine the range, velocity, and angle of radar targets. Figure 2.3 shows the simplified block diagram, only the main RF components are depicted here, of the used FMCW radar in this work.
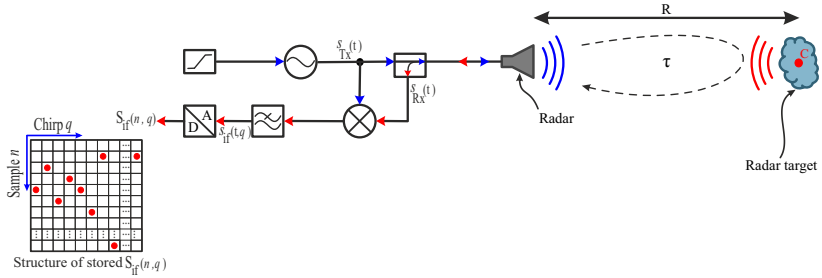

Figure 2.3: Simplified block diagram for the transmitted (blue) and received (red) signals of a monostatic FMCW radar system. The structure of the stored IF data is also illustrated in the direction of slow- and fast-time axis.

As shown in Figure 2.3, the transmitter (Tx) generates a frequency chirp signal by a frequency synthesizer. It is a frequency modulated signal with the carrier frequency of f_0, also called the sweep center frequency of FMCW radar. The transmitted signal [$s_{Tx}(t)$] can be explained by

$$s_{Tx}(t) = A_{Tx} \cos(2\pi f_0 t \pm \frac{1}{2}\alpha t^2), \ 0 \le t \le T_{sweep} \qquad (2.7)$$

where A_{Tx} is the amplitude of the transmitted signal, α is the ramp slope which is the quotient of the ramp bandwidth (Δf), and the ramp time (T_{sweep}). This chirp signal can be in the form of either a sawtooth-shaped frequency modulation signal or a triangular waveform with two ramps of opposite slopes, shown in Figures 2.4 and 2.5, respectively. In the case of a sawtooth-shaped chirp, it can be either a down ramp or an up ramp, and sign $\pm$ in the equations applies to an up ramp and a down ramp, respectively. The full ramp period (T) consists of the ramp duration time (T_{sweep}) and its dwell time. It should be

noted that Figures 2.4 and 2.5 illustrate the specification of the chirp signals in time–frequency domain representation.

Then, the signal $s_{\text{Tx}}(t)$ radiates via the antenna into free space and, after impinging the radar target, which is located in the range of R, reflected back and collected by the same antenna. It is assumed that the radar target is a single point scattering object and produces a round trip propagation delay of τ in the receiver (Rx). The collected signal in the receiver $[s_{\text{Rx}}(t)]$ is the delayed and damped copy of the transmitted signal, which can be written as

$$s_{\text{Rx}}(t) = A_{\text{Rx}} \cos(2\pi f_0(t - \tau) \pm \frac{1}{2}\alpha(t - \tau)^2),\ 0 \le t \le T_{\text{sweep}} \qquad (2.8)$$

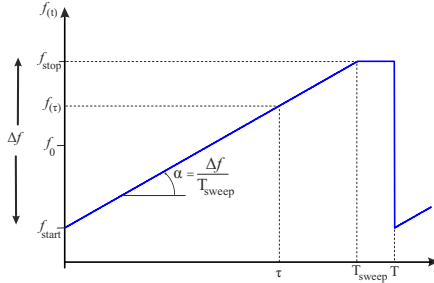where A_{Rx} is the amplitude of received signal.

Figure 2.4: A sawtooth-shaped chirp signal with up ramp with full ramp period of T_{sweep} and ramp duration of T_{sweep}. The frequency chirp runs between f_{start} and f_{stop}.

After receiving the reflected signal, the mixer combines $s_{\text{Tx}}(t)$ and $s_{\text{Rx}}(t)$ and then the upconverted version of the signal is filtered out. The downconverted version of the received signal is utilized as the IF signal (Intermediate Frequency) of a monostatic FMCW radar and can be written as

$$s_{\text{if}}(t) = A_{\text{if}} \cos(\alpha\tau t \pm 2\pi f_0\tau - \frac{1}{2}\alpha\tau^2),\ 0 \le t \le T_{\text{sweep}} \qquad (2.9)$$
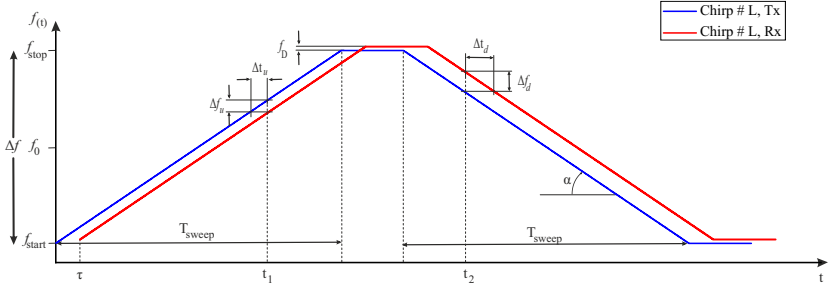
Figure 2.5: A triangular chirp signal consisting of two up and down ramps with opposite slopes. The frequency chirp runs between f_{start} and f_{stop}. The transmitted (blue) and received (red) frequencies of a triangular waveform consist of two ramps of opposite slopes, both with a duration of T_{sweep}. Note that the chirp (L, Rx) is drawn with a small positive Doppler shift of f_D.

where A_{if} is the amplitude of IF signal. The transmitted waveform of an FMCW radar contains M consecutive ramps; therefore, the idealized IF signal is a two-dimensional (2-D) signal and can be defined by

$$s_{\text{if}}(t, q) = s_{\text{if}}(t + (q - 1)T_{\text{sweep}}), \ q \in \mathbb{Z}, \ 1 \le q \le M. \qquad (2.10)$$

where q is ramp index number. That means that the collected IF signal $[s_{\text{if}}(t, q)]$ by an FMCW radar is a function of time (t) and ramp index number (q). It enables the radar to detect multiple targets in its field of view (FoV), which is located in the range of $\text{R}(t)$. Each individual ramp signal of $s_{\text{if}}(t, q)$ is sampled with the sampling rate of the radar ADC (f_s), which results in N samples for each ramp within the time duration of T_{sweep}

$$N = f_s \cdot T_{\text{sweep}}. \qquad (2.11)$$

Accordingly, the analog IF signal is converted to the digital signal, and its resulting samples are stored in a two-dimensional matrix of the size $N \times M$.

15

The collected data from the M ramp signals are saved row-wise with a slow-time[2] index of q, and the samples of every individual ramp are stored in the columns of the matrix with a fast-time [3] index of n. Figure 2.3 also illustrates the structure of 2-D matrix for storing the sampled IF signal of the FMCW radar $[S_{if}(n, q)]$ as a function of fast- and slow-time indexes.

As discussed in [ASW20, ASP$^+$14, AVC$^+$14, PJK$^+$19, PP21], highly accurate and robust distance measurements can be done based on FMCW radar data. The intermediate frequency evaluation (FE) technique is utilized to analyze the collected IF signal from the radar measurement and estimate the range of the radar target. The classical FE technique can be applied to analyze the sawtooth shape modulation signal, denoted as the basic frequency evaluation (BFE) technique in this work. Therefore, the represented time–frequency domain chirp signal (Figure 2.4), with one directional ramp, is investigated for the range estimation. The curve equation in Figure 2.4 can be written as

$$f(t) = \alpha \cdot t + f_{start} \tag{2.12}$$

and equation 2.13 shows a typical relationship for determining the slope of the ramp

$$\alpha = \frac{f(\tau) - f_{start}}{\tau} = \frac{\Delta f}{T_{sweep}} \tag{2.13}$$

Considering the propagation speed of the EM wave in the air (c_0), the accurate distance between the target and the radar can be computed by

---

[2] Measurement with ramp duration time ($\frac{1}{T_{sweep}}$).

[3] Corresponding to the sampled IF data with the sampling rate of the radar ADC (f_s) to collect samples within the time duration of each ramp.

$$R(\tau) = \frac{c_0}{2} \cdot \tau = \frac{c_0}{2} \cdot \frac{f(\tau) - f_{\text{start}}}{\alpha}$$
$$= \frac{c_0}{2} \cdot \frac{f_R(q)}{\alpha}$$

(2.14)

where $f_R(q)$ is the the corresponding intermediate frequency in the radar data which is reflected by the target. Therefore, the range of the targets to the radar can be calculated after determining their corresponding IF on the fast-time axis. For this purpose, the signal processing chain of the BFE technique is shown in Figure 2.6(a). In the first step of the algorithm, the stored 2-D IF is preprocessed by windowing. Then, the spectral estimation is improved by implementing zero padding, which increases the frequency display resolution. The resulting signal $[S_{\text{if}}(n, q)]$ is processed by the fast Fourier transform (FFT) to define the spectrum of the FFT, $\underline{S}_{\text{if}}(k, q)$, where k is the IF index. Finally, the CFAR algorithm is applied on the magnitude of $\underline{S}_{\text{if}}(k, q)$ to detect the related IF in the radar data, which corresponds to the location of the radar target. Subsequently, the ranges of the radar targets are calculated by employing the detected IF frequencies in Equation 2.14.

Since the extracted IF data from the traditional sawtooth waveform can not directly estimate the Doppler frequency of the radar targets, this type of waveform is not beneficial in the approximation of the radial velocity of the target. Therefore, a triangular chirp signal is utilized in the radar measurement, and its ramps have the same ramp duration with opposite slopes [LLHL16]. This technique can enhance the BFE algorithm to analyze the stored IF data matrix and reveal the range and velocity of the radar targets. The enhanced frequency evaluation (EFE) algorithm can calculate the range and velocity of the radar targets by not-shifted intermediate frequency and Doppler shift estimation during two adjacent up and down ramps in the collected radar data. Figure 2.6(b) shows the signal processing chain of the EFE algorithm. First, the algorithm uses the sampled IF data $[S_{\text{if}}(n, q)]$ from the measurement with triangular-shaped frequency chirps as an input. Then the algorithm separates up ramps and down ramps of the collected IF data to store them in two matrices $S_{\text{if,u}}(n, q)$ and $S_{\text{if,d}}(n, q)$, respectively. By applying the BFE algorithm on $S_{\text{if,u}}(n, q)$ and $S_{\text{if,d}}(n, q)$, the EFE algorithm computes $\Delta f_u(q)$ and $\Delta f_d(q)$. As shown in Fig. 2.5, $\Delta f_u(q)$ and $\Delta f_d(q)$ can be calculated from the difference between the IF data of two
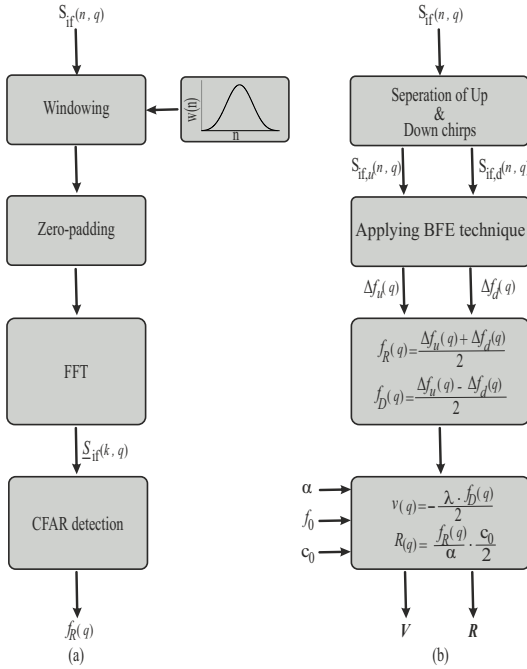
Figure 2.6: (a) Signal processing chain for determining the related IF in the location of the object under test by the BFE technique. (b) Signal processing chain of the EFE technique for estimating the range and velocity of the radar target from the collected radar raw data. A combination of two frequency chirps is processed individually by BFE.(Figure based on [2], ©IEEE).)

successive ramps with the same slope. In this context, the equation for two successive L^{th} and $L+1^{th}$ chirps, stored in the IF data matrix, can be written as

$$f_L(t) = \begin{cases} \alpha\, t + f_{start}, & 0 \leq t \leq T_{sweep} \\ -\alpha\,(t - T_{sweep}) + f_{stop}, & T_{sweep} \leq t \leq 2T_{sweep} \end{cases} \tag{2.15}$$

$$f_{L+1}(t) = \begin{cases} \alpha\,(t - \tau) + f_{\text{start}} + f_D, & \tau \leq t \leq T_{\text{sweep}} + \tau \\ -\alpha(t - \tau - T_{\text{sweep}}) + f_{\text{stop}} + f_D, & T_{\text{sweep}} + \tau \leq t \leq 2T_{\text{sweep}} + \tau \end{cases}$$
(2.16)

in $t = t_1$:

$$f_L(t_1) = \alpha\, t_1 + f_{\text{start}},$$
$$f_{L+1}(t_1) = \alpha\,(t_1 - \tau) + f_{\text{start}} + f_D$$
(2.17)

in $t = t_2$:

$$f_L(t_2) = -\alpha\,(t_2 - T_{\text{sweep}}) + f_{\text{stop}},$$
$$f_{L+1}(t_2) = -\alpha\,(t_2 - T_{\text{sweep}} - \tau) + f_{\text{stop}} + f_D$$
(2.18)

From comparing Equations 2.17 - 2.18 for up ramp and down the ramp, it can be written

$$\Delta f_u = \alpha\,\tau - f_D,$$
$$\Delta f_d = \alpha\,\tau + f_D$$
(2.19)

and the related intermediate frequency (f_R) and Doppler shift (f_D) can be computed by

$$f_R = \frac{\Delta f_u + \Delta f_d}{2},$$
$$f_D = \frac{\Delta f_u - \Delta f_d}{2}.$$
(2.20)

The EFE algorithm applies Equation 2.20 on the calculated $\Delta f_u(q)$ and $\Delta f_d(q)$ for extracting the corresponding IF frequency to range [$f_R(q)$] and Doppler shift [$f_D(q)$] from the qth chirp in the fast-time measurement data. Accordingly, the

algorithm determines the range $[R(q)]$ and the velocity $[v(q)]$ of the radar targets in each chirp by

$$
\begin{aligned}
R(q) &= \frac{f_R(q)}{\alpha} \cdot \frac{c_0}{2}, \\
v(q) &= -\frac{\lambda \cdot f_D(q)}{2}.
\end{aligned}
\tag{2.21}
$$

Finally, the algorithm stores the estimated range and velocity of each chirp in the range matrix ($\mathbf{R}$) and the velocity matrix ($\mathbf{V}$) based on the fast-time index.

3 Angular Resolved RCS Measurement Setup

This chapter discusses the construction of an angular resolved measurement setup based on an FMCW radar sensor for high-resolution monostatic RCS measurements in the radial and angular domain. The radar two-way radiation characteristics are extracted by measuring the well-known standard targets, initially. The results of the subsequent RCS measurements can be correctly interpreted on the condition that the radiation pattern of the own radar system is known. Subsequently, different calibration steps are discussed to validate the measurement setup and correctly extract the radial, angular, velocity, and RCS signatures of a typical VRU.

3.1 High-Resolution mm-Wave Radar Sensor

This work utilizes a radar sensor (as shown in Figure 3.1(a)) that is developed by Ruhr University Bochum (RUB) and fabricated in Infineon's B7HF200 SiGe automotive production technology [PJK+18, PJK+19]. All electronic components of the radar sensor are packaged into a metallic housing with a single micro USB interface for power and data transmission [PJK+18]. The realized sensor is an FMCW radar, based on an ultra-wideband voltage control oscillator (VCO), a low-noise highly linear PLL synthesizer, and a receiver with a tunable ultra-wide bandwidth in the range of 25 GHz around the center frequency of 80 GHz. The software of the sensor allows the user to configure its working parameters within the given range, e.g., the working bandwidth, center frequency, the slop and direction of the ramps inside each chirp, and chirp duration time [PJK+18]. The radar sensor is configured to have a bandwidth of 5 GHz and a center frequency of 78.5 GHz during the measurements, which conforms with the equivalent automotive radar bands. The spatial resolution (ΔR) of an FMCW radar is limited by its bandwidth and can be calculated by

(a)   (b)

Figure 3.1: (a) The utilized radar sensor in high-resolution RCS measurement setup in this work. (b) The designed lens antenna which mounts on the radar and focuses its main beam for high-resolution measurements.

$$\Delta R = \frac{c_0}{2\Delta f} = 3\,\text{cm} \tag{3.1}$$

where c_0 is the propagation speed of the electromagnetic wave in the air and Δf is the bandwidth of the transmitted radar signal. This allows high-resolution radar measurements with a radial resolution of 3 cm. In this work, a standard horn antenna with 20 dBi gain is connected to the waveguide port of the radar for the RCS measurements. Furthermore, the proposed high-resolution measurement setup needs to have an angular scanning capability in such a way that the effective radiation pattern of the radar can be reinforced in a desired direction and suppressed in other directions. That can be achieved either by mechanical or electronic beam scanning methods, which steers the direction of the main beam of the radar antenna. In the constructed setup, the mechanical beam scanning is utilized to approach the desired high level gain, favorite scan coverage, and angular resolution and prevent side lobe interference and mutual coupling effects [GMR15]. Mechanical scanning can steer the direction of the main lobe by moving the feeding antenna along the focal plane [ZGWF22]. Therefore, a dielectric PTFE (polytetrafluoroethylene) lens with a diameter of 205 mm is designed and mounted on the radar sensor (as shown in Figure 3.1(b)) for focusing the main beam with high gain. Afterward, the combination of the radar sensor and the lens antenna is mounted on a two-axis motorized turn-tilt

table to enable the measurement setup for mechanical scanning with desired coverage area.

The radar control unit (RCU) takes control of the rotation direction of the Radar system or radar with the utilization of the embedded turn-tilt table in its setup. The motorized turn-tilt table enables the radar sensor to rotate in both azimuth and elevation directions with the required angular resolution. Figure 3.2 shows the schematic of the setup for the RCU. This setup also comprises the mm-wave FMCW radar sensor, a laptop, a two-axis stepper motor controller, a two-axis motorized turn-tilt table, and a power supply. The laptop sends the initialization message to the turn-tilt table and radar sensor before starting the measurement procedure, and their communication is done via USB interfaces. The angular-dependent radar raw data is collected by controlling the turn-tilt table during the measurement process. Furthermore, the RCU controls the included rotating stage in the measurement setup to scan the different viewing angles of the object under test based on the assigned configuration, which is explained in Section 3.9.
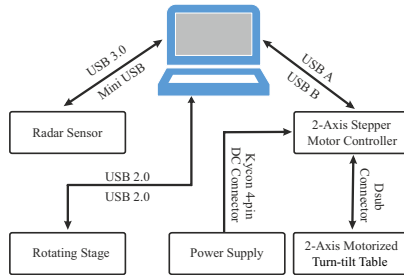

Figure 3.2: Block diagram of the radar control unit (RCU). (Figure based on [1], ©IEEE.)

Throughout the rest of this work, the radar together with the corresponding high-focusing PTFE lens antenna will be called the "Radar system" and the radar sensor will be named as "radar" to avoid any confusion. Before starting any measurement process, it is crucial to assess the source of the uncertainty in the measurement results to achieve reliable results. The traceability of the uncertainty in the measurement results can be attained by evaluating the uncertainty sources in the measurement processes and quantities. Therefore, this chapter continues with pre-measurement steps for distinguishing the uncer-

tainty sources in the results and following a systematic measurement process. The defined pre-measurement steps in this work analyze the two-way radiation pattern, gain, and noise level of the Radar system.

3.2 Measuring the Two-way Radiation Pattern of the radar

As the first pre-measurement step, the two-way radiation pattern of the radar is measured. The two-way radiation pattern of a radar sensor can be utilized to analyze the reflection angle of the incident waves, the half-power beamwidth (HPBW), and the first sidelobe level (SLL). The measurement is conducted in an anechoic chamber in the Institute of Radio Frequency Engineering and Electronics (IHE) at KIT with dimension of $7.4\,\mathrm{m}\times5\,\mathrm{m}\times3.9\,\mathrm{m}$ ($L\times W\times H$). The schematic of the measurement setup is depicted in Figure 3.3(a). The antenna feed of the radar is aligned to the center of the object under test (C) and the distance between them is denoted as R. As shown in Figure 3.3, the radar is capable of scanning the test environment in both azimuth (φ) and elevation (θ) directions by utilizing the motorized turn-tilt table with tunable resolution angles of $\Delta\varphi$ and $\Delta\theta$, respectively. Figure 3.3(b) shows the coordinate system of the radar and illustrates the azimuth and elevation directions. The azimuth angle (φ) is defined as the angle in the xy-plane around the z-axis, where $\varphi = 0°$ is in direction of the y-axis. The elevation angle (θ) is the angle in the yz-plane around the x-axis, where $\theta = 0°$ points in direction of the y-axis. The origin of the coordinate system is the phase center of the feeding horn antenna of the radar.

Figure 3.4 shows the details of the measurement setup in the anechoic chamber using a metallic sphere with a radius of 17.8 cm as a standard calibration object. The sphere is hovered at range of R = 4.7 m in the test setup. The center of the sphere is aligned to the main beam of the radar and this direction is defined as the azimuth angle of 0° and the elevation angle of 0°. The radar scans the area of ±40° in azimuth and ±20° in elevation to measure the two-way pattern measurement with step width of 1°.

Figures 3.5 show the measured beam pattern of the radar using the 20 dBi horn antenna in azimuth and elevation directions. The depicted pattern in Figure
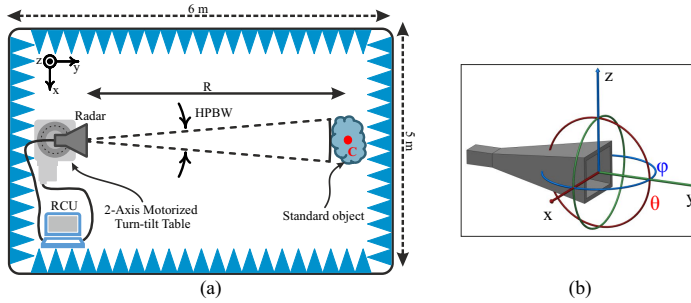
Figure 3.3: (a) Block diagram of measurement setup to extract the two-way radiation pattern of the radar using a sphere as a standard object. (b) The radar coordinate system which defines the rotation angles of the radar in azimuth (φ) and elevation (θ) directions.
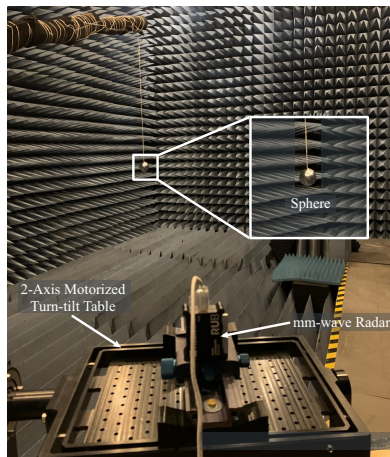

Figure 3.4: Setup for measuring the two-way radiation pattern of radar using a standard object in the anechoic chamber at KIT.

3.5(a) shows that the measured HPBW of the radar sensor is 18° which is in good agreement with the HPBW of the horn antenna. Additionally, the measured first SLL of the radar is around −16.67 dB in the azimuth direction. The plotted pattern in Figure 3.5(b) demonstrates that the patterns in elevation and azimuth directions are almost the same.
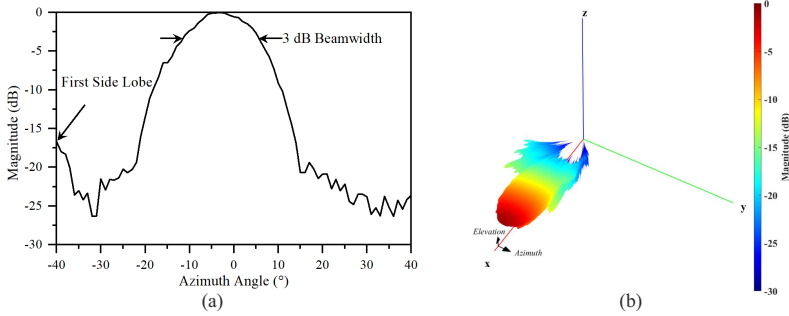

Figure 3.5: (a) Measured two-way radiation pattern of the radar equipped with the horn antenna in azimuth ±40° with 1° step width. (b) Measured two-way radiation pattern of the radar in the scanning area of ±40° in azimuth and ±20° in elevation directions.

Notwithstanding that the 3 cm radial resolution of the radar (calculated by Equation 3.1) is adequate for the range resolution of the radar, its HPBW of 18° is not appropriate for the high-resolution measurement. Consequently, the measured radar data can not be utilized to extract detailed scattering models of complex traffic objects since the VRU is illuminated as a whole by the radar in a measurement distance of more than 3 m. This means that the collected radar data does not have the ability to distinguish between multiple reflection points in angular directions and results in an integral RCS value of the object under test in the related viewing angle by the radar.

As discussed in Section 3.1, a dielectric PTFE lens is designed to focus the main beam of the radar. The proposed lens antenna is mounted on the feeding horn antenna of the radar sensor, as shown in Figures 3.6 and 3.7, so that its phase center is placed inside one of the ellipsoidal focal points of the lens. That transforms the wide main beam into a narrow main beam with a HPBW of 1.3°, which enhances the gain to 40.5 dBi. Section 3.3 discusses the measured and simulated radiation specification of the Radar system in more detail.
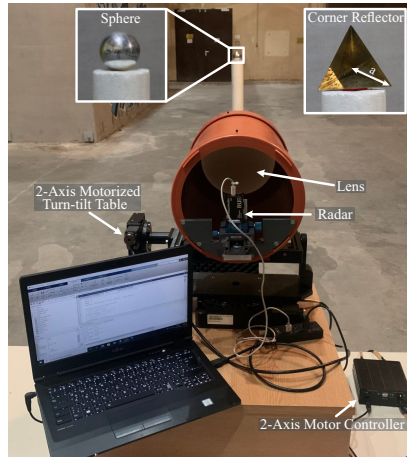
Figure 3.6: Setup for measuring the two-way radiation pattern of the Radar system using a sphere as a standard object as well as the RCS value of a trihedral corner reflector to calculate the RCS calibration factor. In the real environment, not an anechoic chamber. (Figure based on [1], ©IEEE).
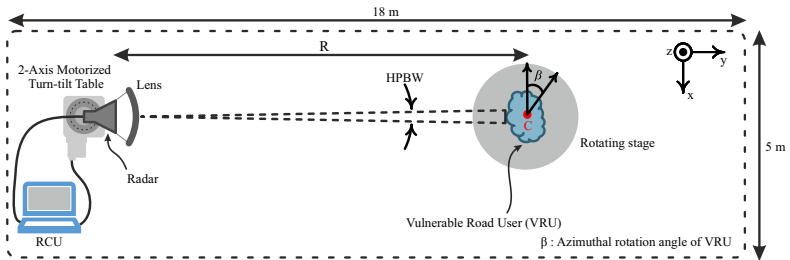

Figure 3.7: Block diagram of measurement setup to detect the scattering points of VRU with its azimuthal rotation angle (β) for radar model extraction. (Figure based on [1], ©IEEE).

27

3.3   Measuring the Two-way Radiation Pattern of the Radar system

After examining the two-way radiation pattern of the radar sensor, this section investigates the radiation pattern of the Radar system, which is constructed from the combination of the radar and lens antenna. The simulated radiation pattern of the proposed lens antenna fed by 20 dBi horn antenna is depicted in Figures 3.8. The simulation is done with the commercially available electromagnetic simulation software CST Studio Suit 2019 (DASSAULT SYSTEMES, Germany). As observed in Figure 3.8(a), the designed lens antenna achieves a HPBW of 1.3° with the gain of 40.47 dBi. Figure 3.8(b) shows the designed antenna system has a pencil-beam and is able to focus the Radar system main beam in both azimuth and elevation directions.
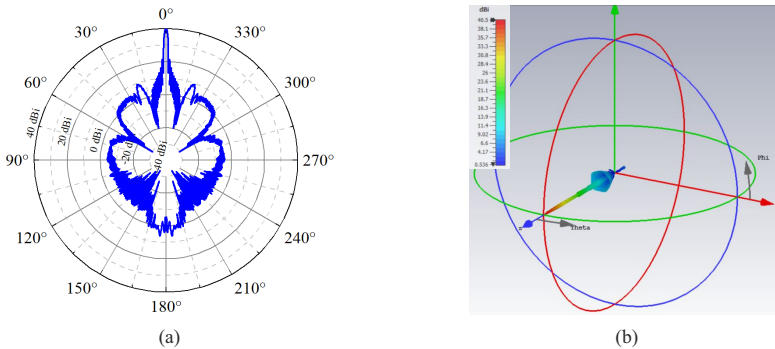

(a)

(b)

Figure 3.8: The simulated radiation pattern of the designed lens fed by the horn antenna of the radar (a) in the focusing plane with $\theta = 90°$, and (b) in the focusing direction with $\varphi = 180°$ and $\theta = 90°$.

The two-way radiation pattern of the constructed Radar system is measured to assess its HPBW and first SLL. A large hall, provided by the Institute for Pulsed Power and Microwave Technology (IHM) at KIT, is considered for the radar test setup and the monostatic RCS measurements. The radar measurements are conducted in a section of the hall with the dimension of $18\,\text{m} \times 5\,\text{m} \times 30\,\text{m}$ ($L \times W \times H$). Figure 3.7 shows the block diagram of the measurement setup. As shown in Figure 3.7, R is the distance between the center of the object

under test (C) and the feed antenna of the Radar system. Further details of the measurement setup in the test environment are depicted in Figure 3.6.

A standard sphere with a radius of 9 cm is located on a Rohacell stand in the range of R = 9 m in the test setup. The Rohacell stand has a permittivity of $\varepsilon_r \approx 1$, which prevents unwanted reflections during the measurement. The main beam of the Radar system is aligned to the center of the sphere, and this direction is defined as the azimuth angle of 0° and the elevation angle of 0°. The Radar system scans the area of ±20° in focusing plane of $\theta = 0°$ and ±10° in the focusing plane of $\varphi = 0°$. The scanning resolution of the radar is 0.1° step width. The scanned area in the azimuth and elevation directions, covers the size of all measured[4] VRUs in this work. The two-way radiation pattern of the Radar system is extracted from the collected radar data and depicted in Figure 3.9.
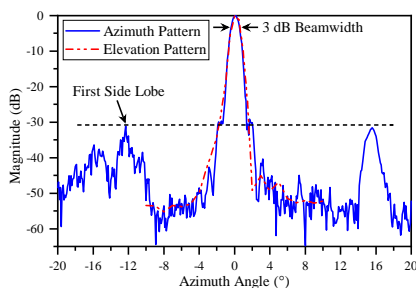

Figure 3.9: The measured two-way radiation pattern of the Radar system in azimuth and elevation directions. (Figure based on [1], ©IEEE).

Figure 3.9 shows the measured pencil-beam pattern of the Radar system in the azimuth and elevation directions. It is observed that the HPBW of the Radar system is 1.3°, and its first SLL is −31.2 dB in azimuth and elevation directions. Furthermore, the patterns in both directions are almost the same due to the rotational symmetry of the lens. There was the metallic equipment in the test environment, which could not be removed, and it gave rise to the distortions in negative azimuth angles. These distortions are distinguishable at the left side of the radiation pattern in the azimuth direction.

---

[4] The maximum measured dimensions are 5 m in azimuth direction and 2.5 m in elevation direction.

In one further step, the test environment is scanned to extract the pencil-beam of the Radar system from the measurement data. The scanning area is set to ±20° in azimuth and ±5° in elevation with step width of 0.5°. The measured pencil-beam is shown in Figure 3.10, which is in good agreement with the simulated pattern in Figure 3.8(b).
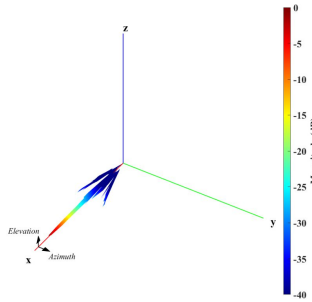

Figure 3.10: Measured pencil-beam of the radar equipped with the lens antenna, which scans the test environment in azimuth and elevation directions.
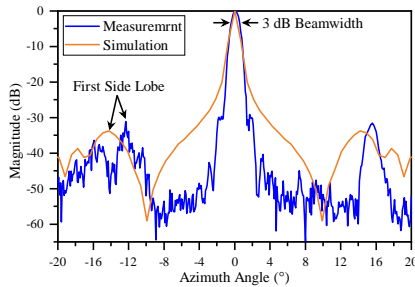

Figure 3.11: Comparison of the measured and simulated two-way radiation pattern of the Radar system.

As one of the preliminary steps, the measured two-way radiation pattern of the radar equipped with the lens is verified by the simulation results in Figure 3.8(a). The comparison of the measured and simulated patterns is inspected in Figure 3.11 to investigate the focusing capabilities of the Radar system. The HPBW of the Radar system is estimated 1.3° in both patterns. It can be noticed

that the first SLL in both patterns is less than -31.2 dB, and they occur at almost the same azimuth angle ($\sim 2°$ difference). This comparison shows a very good match between the measured and simulated patterns around the 6 dB beam-width area. Furthermore, the first SLL is better than -30 dB and located around $\pm 14°$. The angular resolution needed in the high-resolution measurement setup is maximum $1°$, and accordingly, the agreement between the simulation and measurement is good enough in that interval.
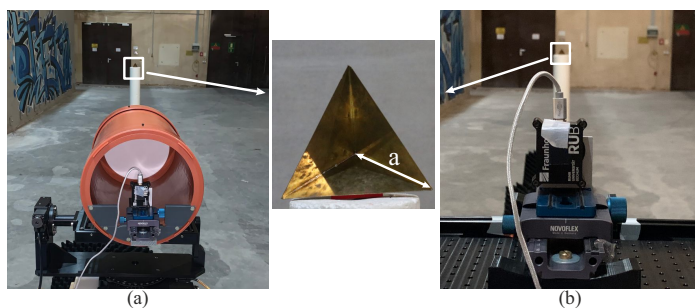

(a)   (b)

Figure 3.12: Setup for estimating the gain of the Radar system. Two measurements are done for a TCR with the size of 4.4 cm in the (a) presence and (b) absence of the lens antenna which is placed in the same range from the antenna feed.

To estimate the gain of the Radar system from the measurement results, a standard trihedral corner reflector (TCR) with the inner height (a) (shown in Figure 3.12) of 4.4 cm is positioned in the measurement setup. It is located in the range of R = 9.06 m from the radar, as shown in Figures 3.12. The utilized TCR in the assigned range is considered as a single scattering point for both the radar and Radar system. The center of the TCR is aligned with the main beam of the radar, and then the radar data is collected in the presence (Figure 3.12(a)) and absence (Figure 3.12(b)) of the focusing lens antenna. The collected raw data is depicted in Figure 3.13. The gain of the Radar system ($G_{Rad-sys}$) can be predicted by comparing the magnitude of the signals (ΔMag) in the detected range of TCR and with the following equation

$$G_{\text{Rad-sys}} = G_{\text{radar}} + \frac{1}{2}\Delta Mag$$
$$= 20\,\text{dB}i + \frac{1}{2}41\,\text{dB} \tag{3.2}$$
$$= 40.5\,\text{dB}i$$

where G_{radar} is the gain of the mounted horn antenna on the top of the radar. Therefore, the Radar system has an overall gain of 40.5 dBi, which is in excellent agreement with the reported value from the simulation (40.47 dBi).
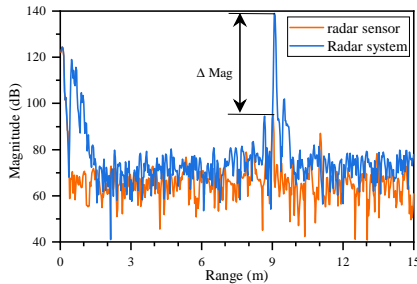

Figure 3.13: Comparison between the reflected signal level in presence and absence of the lens antenna from the positioned TCR in the test environment.

3.4 Examining the Angular Resolution of the Constructed Radar system

Another critical specification for high-resolution RCS measurement is the capability of the Radar system to resolve two equally large objects which are located in the same radial range but at different angles. The angular resolution of the Radar system indicates the minimum distance between two close objects to separate from each other clearly. Accordingly, an experiment is conducted by utilizing two identical TCRs with the size of a = 7.9 cm to determine the angular resolution of the Radar system. Figure 3.14 shows the schematic of

the measurement setup in which the TCRs are positioned in the radial range of $R' = R'' = 9$ m from the radar and their centers are aligned to each other in the distance of $d = 15$ cm. The main beam of the Radar system is pointed in the direction of a perpendicular line to the segment line passing through the centers of TCRs, and the intersection points between them are called (C). The setup of the measurement in the test environment is shown in the inset of Figure 3.15.
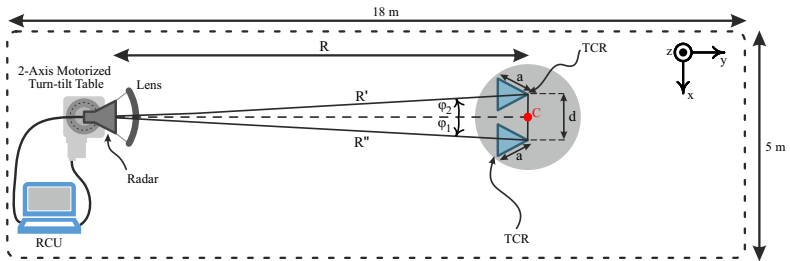

Figure 3.14: Block diagram of measurement setup to inspect the angular resolution of the Radar system. Dimensions of the drawing are not to scale.

The test environment is scanned in the azimuth area of $\pm 10°$ with step $\Delta\varphi = \pm 0.5°$ and elevation angle of $\theta = 0°$. The two-way radiation pattern from the collected radar data in this measurement is depicted in Figure 3.15, and the inset shows the details of the measurement setup in the test environment. The radiation pattern demonstrates that two objects are located in $\varphi_1 = 0.5°$ and $\varphi_2 = -0.5°$. They are resolvable since they have been separated by the HPBW of the Radar system. That means the angular resolution is $1°$ which is roughly the same as the HPBW of the Radar system. This experiment verifies that the Radar system is able to resolve two identical objects with a minimum angular separation of $1°$ or equivalently minimum separation distance of 15 cm at the range of $R = 8.99$ m.

Table 3.1 lists the technical specifications and configurations of the Radar system. Consequently, the proposed Radar system provides the prerequisites for high-resolution radar measurements of VRUs. The radar sensor has a ramp duration time of 4.1 ms and a sweep PLL dwell time of 0.9 ms. Therefore, the full ramp cycle of the sensor is 5 ms. An integration time of 5 s is applied
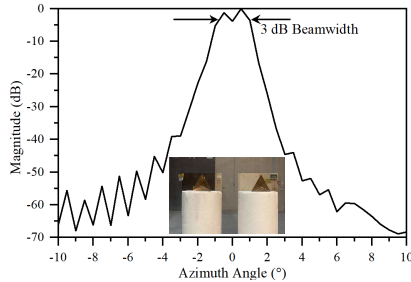
Figure 3.15: Measured radiation pattern from the experiment with two identical TCRs with the size of 7.9 cm, which are located in the radial range of 9 m from the radar. The TCRs are detected in azimuth angles of $0.5°$ and $-0.5°$. The setup of the measurement in the test environment is shown in the inset.

for each θ and φ movement in the RCU configuration in order to damp the vibrations.

Calibration steps play an essential role in a radar measurement setup to determine its technical specifications and configurations and, subsequently, guarantee high accuracy in detection. A complete calibration process of a radar system consists of internal calibration and external calibration steps. Internal calibration examines the radar system for the characteristics of its electronic components, which reveals the system errors, e.g., frequency offset. External calibration is considered as end-to-end calibration. Internal calibration is performed by using a test signal, whereas external calibration involves the measurement of the return signal from the standard radar targets with a known RCS value [RSH10]. Therefore, Sections 3.6 - 3.8 discuss the required calibration steps to achieve reliable RCS data from the constructed high-resolution measurement setup.

3.5 Gain variation of the Radar system

The gain of the Radar system can change over the different radial ranges of the object under test since the object is at a distance below the far-field boundary. Hence, this range dependency is investigated by the calibration measurements. To quantify the influence of this effect, the explained experiment in Section 3.3

Table 3.1: Radar System Technical Specification (Table based on [1, 2]).

Parameter	Radar system Specification
Center Frequency (f_0)	78.5 GHz
Bandwidth (Δf)	5 GHz
HPBW	1.3° in Azimuth and Elevation directions
Ramp Time (T_{sweep})	4.1 ms (saw tooth)
Antenna Gain	40.5 dBi
Transmit Power (P_{Tx})	−6 dBm
Noise Figure (NF)	20 dB
Ramp Slope (α)	±1.25 MHz/µs
ADC Sampling Rate (f_s)	1 MS/s
Integration Time for both θ and ϕ	5 s
Integration Time for β	60 s

has been done for the same TCR but at two different distances from the radar sensor (R = 6.81 m and 9.12 m). The gain of the Radar system ($G_{\text{Rad-sys}}$) can be predicted from the collected raw data and following Equation 3.2.

Figures 3.16 shows the magnitude of the signal from the collected raw data at the different ranges and their comparison (ΔMag). The ΔMag has estimated 41 dB (Figure 3.16(a)) and 43 dB (Figure 3.16(b)) when the corner reflector is located in the range of 9.12 m and 6.81 m, respectively. Accordingly, the gain does not depend on the range for the given ranges. Besides, the most considered VRUs, in this work are shorter than 2 m and will be located at a distance of 9 m from the radar. As a matter of fact, the total range variation in this distance for the pre-defined object is within ±0.6 % range (±5.5 cm) and, accordingly, the magnitude variation over the object surface is within ±0.05 dB. Therefore, the gain of the Radar system is range independent for the given assumptions, although the object is in a range below the far-field boundary.
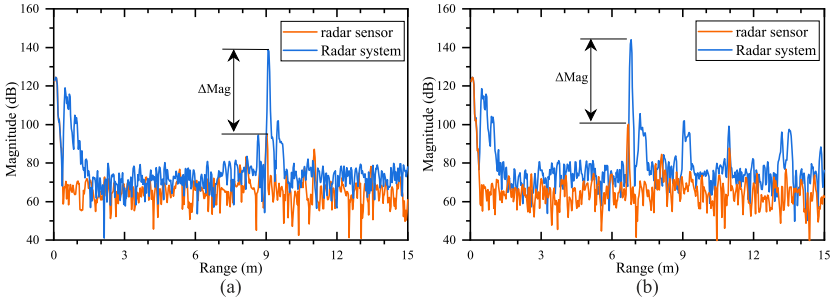
Figure 3.16: Comparison between the measured signal level of a corner reflector at two different ranges, (a) R = 9.12 m, and (b) R = 6.81 m from the Radar system. For each distance a comparison between the radar sensor and Radar system shows the gain. The comparison proofs that the gain is independent of the range.

It is worth emphasizing that the size of the object is considerably small compared to the range. As an example, the maximum elevation sweep is within ±8° since the maximum height of VRUs under scan, in this work, is 2 m. Consequently, the other assumptions in this thesis, e.g, range independency of the antenna gain, are also valid, and the size of all patches is almost the same from the Radar system point of view.

3.6 Measuring the Noise Level of the utilized Radar system

The transmitted signal from a radar undergoes thermal noise in radar electronics, interference signals from the environment, and the reflected signal itself is affected by the radar targets until it is returned [PTWM17]. This section analyzes the noise level of the proposed Radar system and additionally the radar. The rest of the effects are discussed in the following sections.

The internal noise level of a radar sensor can be calculated from the reflected signals when there is not any reflecting target in its field of view (FoV). For this purpose, the signal level of the radar and Radar system is measured when their main beam ($\varphi = 0°$ and $\theta = 0°$) are pointing toward the sky. Figures 3.17 show

the radar and Radar system in the measurement setup for their internal noise level calculation.

Figure 3.17: Setup for measuring the internal noise level of the (a) radar, and (b) Radar system. The main beam of the radar is pointed to the sky.
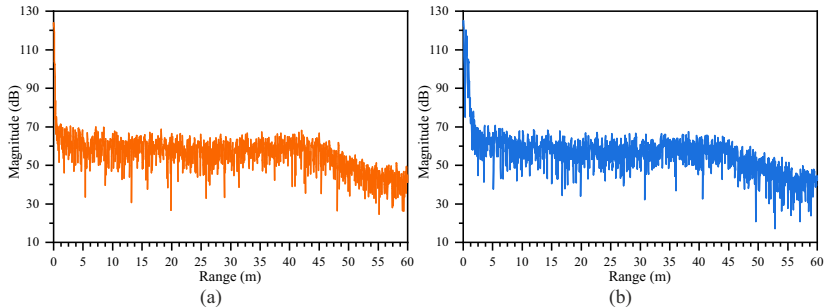

Figure 3.18: Measure signal for the noise level calculation of the (a) radar and (b) Radar system.

The measured signal levels are depicted in Figures 3.18. The observed reflections at the ranges below 5 m show the influence of back reflections in the waveguide port of the radar in Figure 3.18(a) and additionally, from the lens antenna in Figure 3.18(b). Consequently, the noise level is calculated from the measured signal levels in the range of $15 - 40$ m where there is no gain variation in the radar receiver. The measured noise level (N_{Meas}) can be estimated by

$$N_{\text{Meas}} = 20 \log(\sigma) \tag{3.3}$$

where σ is the standard deviation of the measured signal level. The standard deviation of a random variable vector $\mathbf{A}$ made up of signal magnitude of N observations is defined as

$$\sigma = \sqrt{\frac{1}{N-1} \sum_{i=1}^{N} |\mathbf{A}_i - \mu|^2} \tag{3.4}$$

where μ is the mean of $\mathbf{A}$

$$\mu = \frac{1}{N} \sum_{i=1}^{N} \mathbf{A}_i. \tag{3.5}$$

Finally, the measured noise level of the radar ($N_{\text{Meas,rad}}$) is 52.75 dB and the Radar system ($N_{\text{Meas,Rad-sys}}$) is 52.93 dB. As it is expected, $N_{\text{Meas,rad}}$ and $N_{\text{Meas,Rad-sys}}$ are in good agreement.

3.7 RCS Calibration Factor

A calibration of the measured RCS values is crucial to achieve normalized RCS data during the radar measurements. For this reason, measuring the RCS of a standard TCR is one of the necessary prerequisite to prepare an actuate high-resolution RCS measurement setup. A calibration factor for the measured RCS values can be calculated by comparing the measured RCS value of the TCR and its analytical value. The analytical RCS of a standard TCR can be estimated [RSH10] by

$$RCS = \frac{(4\pi)a^4}{3\lambda^2} \tag{3.6}$$

where a is the inner height of the TCR, as shown in Figure 3.6, and λ is the wave length.

In this work, a TCR with the size of 4.4 cm is chosen for the calibration factor experiment since it can be seen as a single point scatterer in the measurement setup (Figure 3.6). In this experiment, the TCR is positioned at the range of R = 9.0 m from the radar, and its main beam is aligned to the TCR center. Then, the scanning range is set to ±10° in the azimuth direction and 0° in the elevation direction, considering the size of the TCR. Its analytical RCS value is calculated to be 0.3 dBsm by using Equation 3.6. Figure 3.19 shows the measured signal level (S_{Meas}) when the Radar system is pointing to the center of the TCR ($\varphi = 0°$, $\theta = 0°$) under test.
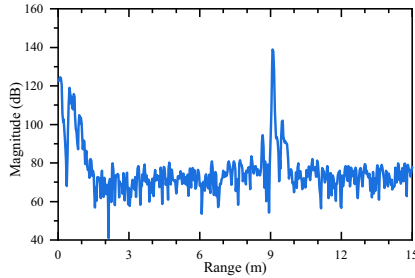

Figure 3.19: Measured signal level of a TCR with the size of 4.4 cm is positioned in the main beam of the Radar system corresponding to the azimuth angle of 0° and elevation angle of 0°.

By utilizing the Equation 2.5, the measured SNR (SNR_{Meas}) of the Radar system in the presence of the TCR can be estimated by

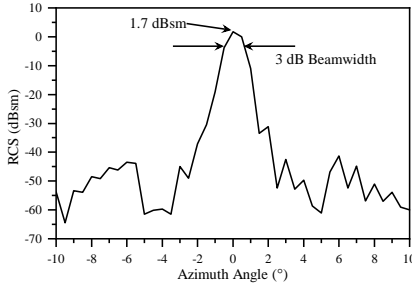$$SNR_{Meas} = \frac{S_{Meas}}{N_{Meas}} \tag{3.7}$$

Figure 3.20: The measured RCS value for a TCR with the size of 4.4 cm which is positioned in the main beam of the radar system in the azimuth scanning area of ±10°. The TCR is detectable in 0° azimuth angle and corresponds to the main beam of the Radar system. (Figure based on [1], ©IEEE).

where S_{Meas} is the measured level of the signal in the place of the object (Figure 3.19) and N_{Meas} is the measured noise level of the Radar system in Section 3.6. By comparing Equations 2.4 - 2.6, the measured RCS value (RCS_{Meas}) can be followed by

$$RCS_{\text{Meas}} = \frac{(4\pi)^3 \; R^4 \; k \; T_{\text{abs}} \; \text{NF}}{P_{\text{Tx}} \; G^2_{\text{Rad-sys}} \; T_{\text{Sweep}} \; \lambda^2} SNR_{\text{Meas}}. \tag{3.8}$$

The measured RCS value is approximated to 1.7 dBsm from the reflected signal level and following Equation 3.8. Consequently, the difference between the measured and analytical RCS values is assigned as the calibration factor of the measurement setup, which is −1.4 dBsm. The measured RCS pattern of the TCR is depicted in Figure 3.20 in the azimuth scanning area of ±10° from the collected radar data. As illustrated in Fig. 3.20, the TCR is detected at an azimuth angle of 0° and is within the HPBW area of the Radar system.

Comparison of simulation and measurement results, presented in Figures 3.9, 3.11, and 3.20, also reveals the effect of incident wave direction on the received signal from standard objects (sphere and corner reflector). Accordingly, the two-way radiation pattern of the Radar system and measurement calibration factor

are extracted. That can verify and quantify the effect of the backscattering behavior of each patch based on the incidence angle.

3.8 Clutter Level Measurement

Characterization of the test environment is critical to achieving a reliable perception and understanding of the backscattering behavior of VRUs under test. One step of the calibration is characterizing the test environment. As discussed in Section 3.6, the collected signal by the receiver antenna of the radar contains echoes from unwanted objects in the test environment. This is also known as the clutter of the environment. The environment clutter level (CL) can be defined as the maximum measured RCS value in the absence of the test object in the test environment. An exemplary measurement setup for collecting the radar data and characterization the test environment is shown in Figure 3.21.
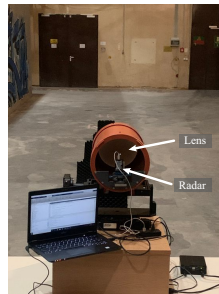

Figure 3.21: Exemplary setup for measuring the clutter level of the test environment. The Radar system scans the test environment in the absence of any object.

In this work, the background clutter level measurements are performed in the same range of the Radar system experiments and the same rotation stage scanning angles. Also, the rotation stage is located in the same place where the object under the test will be located. Accordingly, the RCS values from the background are computed for each θ, φ, β, and R voxel. A threshold level (TH) is introduced in the evaluation of the measurement results with the object. Then, the RCS values which are at least 10 dB above floor level (TH = $CL + 10$ dB) are considered as the RCS value of the object under test. In this manner, it

can be ensured that only the relevant RCS values to the object under test are considered for modeling its backscattering behavior. Further details of the clutter level measurements are discussed while analyzing the measurement results in Chapters 4 and 5.

It is worth noting that the measured RCS values are independent of the distance between the object and the sensor, which is thoroughly inspected in Section 3.5. However as explained in Section 3.9, it depends on the FoV of the Radar system.

3.9   Extracting the Scattering Points of the VRUs

Considering the 3.82 mm wavelength at the operating frequency of the Radar system, the VRUs are electrically large objects involving multiple reflections. Additionally, the HPBW of the Radar system illuminates only a part of the VRU. As a consequence, the RCS values depend on the observation angles by the radar sensor, which is the relative orientation of the radar and the VRU (corresponding to β in Figure 3.7). Therefore, it is indispensable to conduct the radar measurements for different rotation angles β of the object under test, in addition to Radar system scanning angles θ and φ, to study and model the backscattering behavior of VRU. It is worth mentioning that in these measurements, the total considered scattering parameters consist of θ, φ, and β. Only in this case, the reconstructed radar models from the collected radar data come closer to the real application of an automotive radar since, in the real-world application, the VRU is illuminated under different viewing angles, e.g., stepping into the street from the sidewalk or moving in the direction of traffic.

For measuring the high-resolution monostatic RCS of the VRUs, the object under test is placed in front of the Radar system on the rotating stage. The height of the Radar system is adjusted at approximately half the height of the object under test and toward its center. After assigning measurement setup configuration, the object under test is rotated around the z-axis with an adjustable azimuthal resolution angle ($\Delta\beta$) over the whole 360° azimuthal rotation angle. The schematic of the measurement setup for extracting the high-resolution radar model of the VRUs is similar to the one shown in Figure 3.7. The details of the setup for measuring different VRUs in the test environment are shown in Figure 3.22. The scanning area of the Radar system in elevation (θ) and azimuth (φ) directions is calculated according to the size of the object under

test and the range (R) with a step width of $\Delta\theta$ and $\Delta\varphi$. Further details for every measurement setups, i.e., the Radar system scanning angles, their resolutions, azimuthal rotation angles, and, the step width of the azimuthal rotation angles, are discussed in Chapters 4 and 5.

Figure 3.22: Setup for monostatic high-resolution RCS measurement of VRUs to extract their radar model (dummy human is placed on top of the rotating stage for extracting its scattering points) (Figure based on [1], ©IEEE).

In Figure 3.22, the measurements are performed by locating the object under test on the rotating stage at a distance of R = 9 m from the Radar system. Then, the radar collects the spatial distribution of the scattering points (SPs) of the VRU. As a proof of concept, the reconstructed radar images corresponding to multiple rotation angles are depicted and analyzed in Chapters 4 and 5. Moreover, an integration time of 60 s is applied for each β rotation in the RCU configuration. Accordingly, the integration time for the Radar system movement has been presented in Table 3.1.

In a different approach based on the inverse synthetic aperture radar (ISAR) technique, in the literature like [PMR17], Pieraccini *et al.* used the setup consisting of a standard horn antenna and network analyzer which illuminates the target with the antenna boresight and rotates the target. In contrast, current work employs a radar sensor for the radar measurements and also accounts for

illumination with slant incidence, which is closer to the real-world application. Furthermore, the main difference between the current work and the ISAR technique reported by Pieraccini [PMR17] lies in the scanning method. In the present work, three different scanning parameters (azimuth, elevation, and azimuthal rotation angle of VRUs) are considered to generate an accurate 3-D radar model of the object. In this case, the effect of incidence wave angle on the elementary surfaces of the object is also included. In several traffic scenarios, the incident angle to the VRU from the radar may not be perpendicular, e.g., when the VRU steps into the street from the side of the road. Therefore, the effect of incidence angle plays an important role and cannot be simply ignored. In the ISAR technique, just two different scanning parameters are considered, i.e., rotation and height (elevation). Therefore, the collected signals correspond to the elementary surfaces at orthogonal incidence angles, and the information corresponding to the rest of the object is lost. The ISAR method considers each elementary surface as an omnidirectional object, whereas the current work is more general and assumes the elementary surfaces as multidirectional objects with a particular RCS pattern. In principle, an ISAR technique as proposed in [PMR17] may also be feasible, but considering the given assumptions about the incidence angle, it would not result in a shorter measurement time.

3.10 RCS Patterns of VRUs in the Absence of the Lens Antenna

Considering the 5-D results, i.e., range, azimuth, elevation, rotation angles, and RCS values, in this work and 3-D, i.e., range, rotation angles, and RCS on the former researches [BCC+14, CC14, SKM+13], the results cannot be directly compared. Nevertheless, as a secondary step for calibration and validation of the measurement results, an experiment is defined on the human object when the lens is removed from the Radar system. In this setup, the object is considered as a single scattering point. Then, the extracted RCS pattern can be compared with the reported ones in the literature [BCC+14, CC14, SKM+13, YTN05].

Figure 3.23(a) shows the setup for the RCS pattern measurement of a human (with the height of 170 cm and shoulder width of 40 cm) in the anechoic chamber and far-filed of the radar. The distance between the person under test and the radar sensor is 5.7 m. The measured RCS pattern for an exemplary human is

depicted in Figure 3.23(b) and shows that the measured RCS values have a maximum value of 0 dBsm and a minimum value of −16.6 dBsm. It can be observed that the measured RCS pattern is in good agreement with the reported patterns in [BCC+14, CC14].
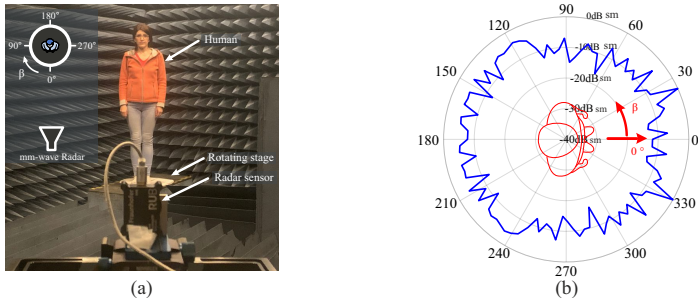

(a)   (b)

Figure 3.23: (a) Setup for measuring the RCS pattern of a human. The measurement is performed within an anechoic chamber, and a human stand on top of the rotating stage to measure its RCS over different azimuthal angles (β). (b) Measured RCS pattern of a human at the measurement setup when the lens antenna is removed (Figure based on [1], ©IEEE).

This experiment is repeated for a bicyclist and motorcyclist by utilizing a dummy rider [FJM13] with similar backscattering behavior to a person. The measurements are performed over 360° azimuthal rotational angle of the object under test. Regarding the dimension of the anechoic chamber in IHE and the size of the dummy riders, it is unfeasible to conduct the RCS pattern measurement in the far field of the riders. Therefore, the experiments are conducted in the radar test environment. Figures 3.24(a) and 3.25(a) show a dummy rider in the setup for measuring the RCS pattern of an exemplary bicyclist and motorcyclist, respectively. The center of the dummy rider is positioned in range of 9 m from the radar.

The measured RCS patterns of dummy bicyclist and motorcyclist are shown in Figures 3.24(b) and 3.25(b). It can be noticed that the measured RCS values over bicyclist azimuthal angle change between −12 and 13 dBsm, which are in good agreement with measured values in [BCC+14]. The measured RCS values of a motorcyclist vary between −7 and 8 dBsm from Figure 3.25(b) which are expected values in comparison with the reported values in [SFGT+11].
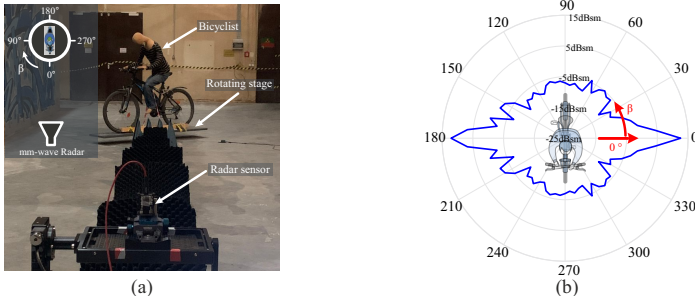
45

Figure 3.24: (a) Setup for measuring the RCS pattern of a bicyclist. The measurement is performed when a dummy bicyclist is mounted on top of the rotating stage to measure its RCS over different azimuthal angles (β). (b) Measured RCS pattern of a bicyclist at the measurement setup when the lens antenna is removed.

However, the reported measurements in [SFGT$^+$11] have been performed in the frequency range 23-27 GHz.
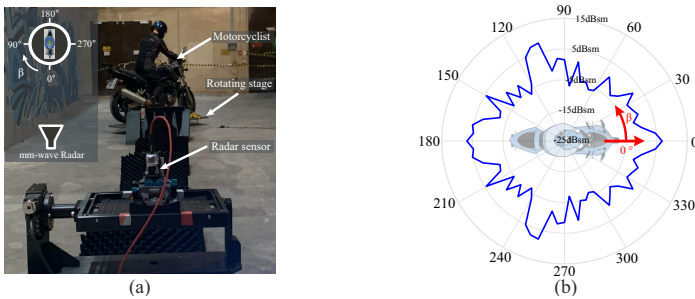

Figure 3.25: (a) Setup for measuring the RCS pattern of a motorcyclist. The measurement is performed when a dummy motorcyclist is mounted on top of the rotating stage to measure its RCS over different azimuthal angles (β). (b)Measured RCS pattern of a motorcyclist at the measurement setup when the lens antenna is removed.

From Figures 3.23, 3.24, and 3.25, it can be concluded that the information from the RCS patterns is not enough for accurate wave propagation simulation since the RCS values of different VRUs are similar in some azimuthal angles. These results do not recognize the type of VRUs, and subsequently, reduce

46

the accuracy of the backscattering behavior and radar model of the VRUs. The results discussed in this section also demonstrate the necessity of high-resolution RCS measurements for developing realistic VRU models.

4 Radar Signature Characterization of Static VRUs

As discussed in the previous chapter, the constructed measurement setup enables the collection of unprocessed raw data corresponding to the different values of θ, ϕ, β, and the distance between the radar sensor and the center of the object under test (R). These data can be used to reconstruct the 3-D extension of the VRUs and determine the location of different SPs on their body precisely. In this context, the current chapter explains the utilized algorithm and the necessary signal processing steps for extracting the radar model of the measured objects based on the collected radar raw data. The measured objects in this chapter are in a static situation. Accordingly, dedicated measurements are arranged to scan the different sized volunteer persons, a dummy human, a bicyclist, a motorcyclist, and a typical car. The measurements are performed in different view angles of the Radar system. Then, the approximated surface contour and the extracted radar model of the VRUs under study are presented with a special algorithm. The chapter continues with analyzing the radar model of the different humans and dummy human to predict the location of human body parts and estimate the detailed sizes of the measured models. The last part of the chapter compares the specifications of the measured radar model of the dummy human with a person having a similar size. Additionally, it briefly discusses target classification based on the extracted radar models from the measurement.

4.1 Algorithm for Extracting the 3-D Extension of Targets from the Collected Data

This section describes the utilized processing steps to extract the scattering points corresponding to each combination of the measurement parameters. The collected raw data of the Radar system corresponds to the sampled IF data
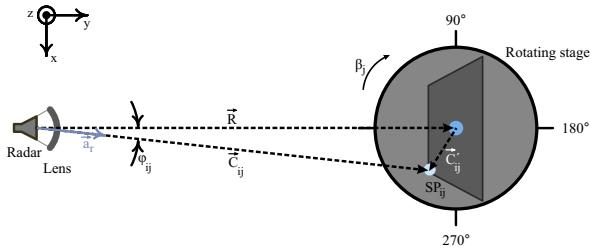
Figure 4.1: An object under test where its front side is illuminated by the Radar system with a description of the relevant geometry and the coordinate system (Figure based on [1], ©IEEE).

$[S_{\mathrm{if}}(\varphi_{ij}, \theta_{ij}, \beta_j)]$ of the radar from measuring the object under test in every azimuthal rotation angle (β_j) with a step width of $\Delta\beta$. Furthermore, the Radar system scans each viewing side of the object under test in the range of $\pm\varphi_{ij}$ in azimuth and $\pm\theta_{ij}$ in elevation directions with a step width of $\Delta\varphi$ and $\Delta\theta$, respectively. The coordinate systems of the measurement setup and its relevant geometry is shown in Figure 4.1. The radar sensor is assumed as the origin of the spherical coordinate system and the position $(\vec{C}_{ij})$ of each scattering point $(\vec{SP}_{ij})$ in this coordinate system can be written as

$$\vec{C}_{ij} = \begin{bmatrix} C_{ij} & \varphi_{ij} & \theta_{ij} \end{bmatrix} \tag{4.1}$$

where φ_{ij} and θ_{ij} are the certain azimuth and elevation angles of the ith detected scattering point (SP_{ij}) in the viewing angle of β_j. Considering the geometry in Figure 4.1, the position $(\vec{C_{ij}}')$ of the ith scattering point in the coordinate system whose origin is the center of the object, can be obtained by

$$\vec{C}_{ij} = \vec{R} + \vec{C'}_{ij} \tag{4.2}$$

where $\vec{R}$ is the vector connecting the radar sensor to the center of the object under test. Therefore, $\vec{C_{ij}}'$ can be followed by

$$
\begin{aligned}
\vec{C}'_{ij} &= \left\| \vec{C}_{ij} \right\| \vec{a}_r - R\vec{a}_y \\
&= \begin{bmatrix} x'_{ij} & y'_{ij} & z'_{ij} \end{bmatrix}
\end{aligned}
\tag{4.3}
$$

where $\vec{a}_y$ and $\vec{a}_r$ are the unit vectors in the Cartesian and spherical coordinate systems, respectively, and x'_{ij}, y'_{ij}, z'_{ij} are the SP_{ij} location in the radar coordinate system. The sensor height and elevation angle of each scattering point (θ_{ij}) influence the z component of $\vec{C}'_{ij}$. Finally, the SP_{ij} location in the VRU coordinate system can be described using the azimuthal rotation angle β_j and the standard rotation axis matrix as

$$
\begin{bmatrix} x''_{ij} \\ y''_{ij} \\ z''_{ij} \end{bmatrix} = \begin{bmatrix} cos(\beta_j) & sin(\beta_j) & 0 \\ -sin(\beta_j) & cos(\beta_j) & 0 \\ 0 & 0 & 1 \end{bmatrix} \begin{bmatrix} x'_{ij} \\ y'_{ij} \\ z'_{ij} \end{bmatrix}
\tag{4.4}
$$

where x''_{ij}, y''_{ij}, z''_{ij} are the coordinates of the ith scattering point in the VRU Cartesian coordinate system and radar viewing angle of β_j. Therefor, it can be expressed as

$$
S\vec{P}_{ij} = \begin{bmatrix} x''_{ij} & y''_{ij} & z''_{ij} \end{bmatrix}.
\tag{4.5}
$$

The extracted coordinates in the VRU coordinate system can be utilized to generate the radar model of the object and evaluate its 3-D RCS profile. That means the RCS value corresponding to the each extracted scattering point (RCS_{ij}) is

$$
RCS_{ij} = f(\varphi_{ij}, \theta_{ij}, \beta_{ij}).
\tag{4.6}
$$

As discussed in previous chapters, the collected raw data of the high-resolution monostatic RCS measurements contains the received power by the Radar system (P_{Rx}). By comparing Equation 3.8 and the geometry of the setup in Figure 4.1, the measured RCS value (RCS_{ij}) in the place of the ith extracted scattering point and radar viewing angle of β_j, can be calculated by

$$\text{RCS}_{ij} = \frac{(4\pi)^3 \left\| \vec{C}_{ij} \right\|^4 k\, T_{\text{abs}}\, \text{NF}}{P_{\text{Tx}}\, G_{\text{Rad-sys}}{}^2\, T_{\text{Sweep}} \lambda^2} \text{SNR}_{\text{Meas},ij} \tag{4.7}$$

where $\left\| \vec{C}_{ij} \right\|$ is the radial distance between the radar sensor and the ith scattering point, and $\text{SNR}_{\text{Meas},ij}$ is the measured SNR for SP_{ij}. It can be calculated by using Equation 3.7 and the measured noise level of the Radar system ($N_{\text{Meas,Rad-sys}}$) in Section 3.6 as

$$\text{SNR}_{\text{Meas},ij} = \frac{S_{\text{Meas},ij}}{N_{\text{Meas,Rad-sys}}} = \frac{|\overline{sl}_{ij}|}{N_{\text{Meas,Rad-sys}}} \tag{4.8}$$

where $S_{\text{Meas},ij}$ is the magnitude of the measured signal level ($\overline{sl}_{ij}$) related to SP_{ij}. Accordingly, the object list matrix (**OL**) from the collected radar data in azimuthal rotation angle of β_j can be expressed as

$$\mathbf{OL}_{\text{OUT},St}(\beta_j) = \begin{bmatrix} x''_{1j} & y''_{1j} & z''_{1j} & \text{RCS}_{1j} & \varphi_{1j} & \theta_{1j} & \overline{sl}_{1j} \\ \vdots & \vdots & \vdots & \vdots & \vdots & \vdots & \vdots \\ x''_{ij} & y''_{ij} & z''_{ij} & \text{RCS}_{ij} & \varphi_{ij} & \theta_{ij} & \overline{sl}_{ij} \\ \vdots & \vdots & \vdots & \vdots & \vdots & \vdots & \vdots \\ x''_{Pj} & y''_{Pj} & z''_{Pj} & \text{RCS}_{Pj} & \varphi_{Pj} & \theta_{Pj} & \overline{sl}_{Pj} \end{bmatrix} \tag{4.9}$$

where P is the total number of extracted scattering points in each radar viewing angle of the object under test. Finally, the high-resolution radar model of VRU

in each azimuthal rotation angle can be made by using the RCS values of the extracted points and their corresponding coordinates. In addition, the 3-D radar model of the VRUs can be constructed by the combination of the extracted **OL** matrices over the whole 360°.

Figures 4.2 show the signal processing chains for extracting the **OL** matrix of the object under test (OUT) in each β_j. The initial scattering point matrix $[\mathbf{SP}(\varphi_{ij}, \theta_{ij}, \beta_j)]$ can be extracted by basic signal processing steps in Figure 4.2(a) which its rows include φ_{ij}, θ_{ij}, βj, $\left\|\vec{C}_{ij}\right\|$, $\overline{sl}_{ij}$, and RCS$_{ij}$. The signal processing chain in Figure 4.2(a) starts with windowing. The windowing step is done by the normalized Dolph-Chebyshew window, and then, the fast fourier transform (FFT) processes $S_{\text{if}}(\varphi_{ij}, \theta_{ij}, \beta_j)$ to determine the spectrum of the FFT $[\underline{S}_{\text{if}}(\varphi_{ij}, \theta_{ij}, \beta_j)]$. The radar targets are detected by applying the CFAR algorithm on the magnitude of $\underline{S}_{\text{if}}(\varphi_{ij}, \theta_{ij}, \beta_j)$ and a subsequent RCS calculation for each detected scattering point by utilizing Equations 4.7 and 4.8. N$_{\text{Meas}}$ is the measured noise level of the Radar system.

Figure 4.2(b) shows the signal processing chain and the necessary calibration procedures to extract the **OL** matrix of the object under test (**OL**$_{\text{OUT},St}$) in the static situation. Before starting the high-resolution RCS measurement procedure for a specific VRU, the Radar system scans the empty test environment to collect the raw data from an empty room measurement $[S_{\text{if,emp}}(\varphi_{ij}, \theta_{ij}, \beta_j)]$. In the second step, a standard TCR with a specific RCS value is measured to normalize the amplitude of the measured values for the VRU. $S_{\text{if,cr}}(\varphi_{ij}, \theta_{ij}, \beta_j)$ is the measured raw data from the standard TCR with an analytical RCS value of 0 dBsm. After the prerequisite calibration steps, the VRU is positioned in the measurement setup to collect the radar raw data from measuring the object under test $S_{\text{if,OUT}}(\varphi_{ij}, \theta_{ij}, \beta_j)$. The discussed procedure is necessary to obtain only reflections from the object under test. It is worth mentioning that the RCS values are not varying with the distance between the object and the radar; in other words, it is a commutative variable.
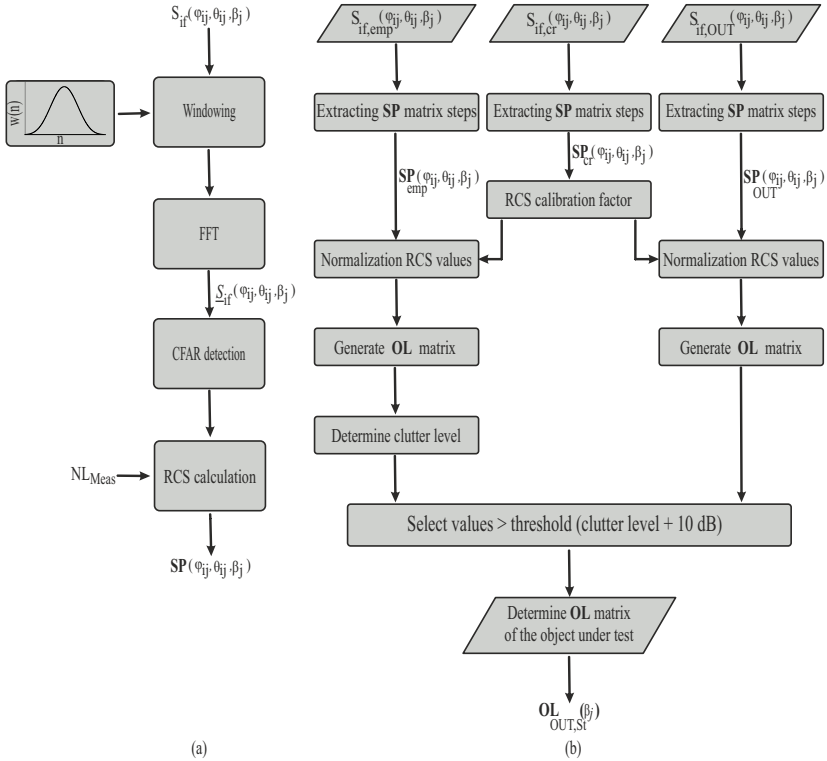
Figure 4.2: (a) Signal processing chain for determining the initial scattering points matrix in the location of the object under test. (b) Signal processing chain for extracting the object list matrix from the high-resolution measurement data in each radar viewing angle.

4.2 Extracted Radar Model of Human in Static Situation

The high-resolution monostatic RCS measurement setup, described in the previous chapter, is used to measure the five different-sized volunteer persons and a human dummy. Then, the principle for extracting the scattering points of VRUs, discussed in the earlier section, is utilized to analyze the measurement results. In another validation step, the extracted scattering points are analyzed to derive the physical sizes of the measured persons. The volunteer persons have been measured in a static situation. One of the challenges for the high-resolution measurement of the person arises when the person should not move for a long time. The measurement time depends on the resolution of the radar scanning angles and azimuthal rotation angle, which can increase the measurement duration to more than two hours. The size of the volunteer test persons characterizes them into five categories, i.e., skinny (A), small (B), kid-size (C), tall (D), and thickish (E).

As mentioned, a high-resolution RCS measurement of a person is time-intensive for extracting its complete 360° radar model and thus leads to errors due to the unintended motions of the person under test. Moreover, dangerous traffic maneuvers can not be tested with a real human in the field. For the mentioned reasons, these issues cannot be addressed with human objects. The objective is to test a dummy human instead of a real test person to replace the human in costly and more time-consuming experiments. Accordingly, an experiment is conducted using a synthetic foam-based dummy of similar sizes to person (A). Considering the similarity in their physical dimensions, it is expected that the extracted radar models of the person (A) and the dummy show nearly identical locations for the main scattering points as long as the models show a similar reflection coefficient. Test person (A) is measured with an increased resolution and the results are compared to the results of the dummy.

The two relevant automotive radars working frequencies are 25.5 GHz and 78.5 GHz; as a consequence, the radar waves have a short wavelength. Therefore, the penetration depth of the radar waves into a body or cloth material is very low [CKC13], and subsequently, the main reflections of a human body in traffic environments are attributable to the cloth material of the person under test. In [CC14], the absorption of mm-Waves radar signals through dry and thin clothes are evaluated in the frequency band of 76-81 GHz, and it has been demonstrated

that the radar wave penetration is negligible in the mentioned circumstance. Nevertheless, the thickness and composition of the clothes, e.g., weather, bike protection clothing, or work clothing, has an influence on the positions of the peaks and nulls in the RCS patterns of the human under test. Furthermore, Schubert and Yamada [SKM$^+$13, YTN05] investigated the influence of the cloth material, with different fabrics and sizes, on the RCS patterns of a human. It was concluded that a person dressed up with cotton has nearly similar RCS to a human without clothes. Therefore, the test persons and the dummy are dressed in dry shirts and pants of thin cotton material in high-resolution measurements. This enables the development of a more realistic back-scattering model of the human body in which the impact of the cloths and surface materials on the reflection characteristics of the human can be assumed as a marginal impact on the RCS values. In different scenarios, the influence of human clothes can be considered by adding a small amount of reflectivity to the RCS values of the extracted scattering points. The literature already contains several reports presenting the influence of different clothes on the RCS values [SKM$^+$13, CKC13]. Additionally, it is worth emphasizing that all models are specified homogeneous since the electromagnetic waves at the working frequencies of the Radar system do not penetrate through the skin layer [CKC13] and the clothing, respectively.

It should be noted that the radar test environment is characterised before measuring the test persons and dummy to introduce the clutter level (CL) of the test environment. The maximum value of the measured RCS in the absence of the object is -45 dBsm which is defined as the clutter level (CL) of the test environment. In the post-processing of the measurement results with the object, the values which are above TH $= -35$ dBsm are considered as the relevant scattering points of the object under test.

The radar models of the categorized test persons and the dummy are computed [$\mathbf{OL}_{\text{OUT},St}(\beta_j)$] to determine the SPs of the object under test and analyze the RCS characteristics of these VRUs. The main information, which the extracted radar models provide, is the location of the scattering points over the body surface and their corresponding RCS values. The radar models are extracted from conducting the high-resolution RCS measurement for persons (A) to (E) and dummy over the whole 360° azimuthal rotation angle with different step widths ($\Delta\beta$). In order to investigate the backscattering behavior of a human on its different sides, the person must stand in the measurement setup for

a relatively long time. It takes in average ~20 min for the scanning of each azimuthal rotation angle (β_j). Therefore, the measurements are conducted for the persons (B) to (E) with 90° step width. This measurement resolution is still adequate to detect certain parts of the body, as will be shown in further discussion. The high-resolution RCS measurements are done with finer step widths on the person (A) and dummy, which enables a comparative analysis of their backscattering behavior. The step width of the azimuthal rotation angle is configured 10° when the dummy is positioned in the measurement setup. The measurements are performed with a rotation step size of 30° for the person (A). The whole measurement takes a long time, although it is endurable.

For measuring the high-resolution monostatic RCS of the human body or dummy, the test objects are positioned in the measurement setup (Figure 3.22). Then, the Radar system scans them in elevation direction with steps of $\Delta\theta = 1°$ to cover the whole height of the object under test. The width of the object under test defines the azimuth scanning range in the measurement configuration, and all the objects are scanned with $\Delta\phi = 1°$. In this manner, it can be expected that assigned scanning areas cover the whole dimension of the radar targets.

It is essential to methodically examine the extracted models of the persons and dummy human under test. For this reason, the four major human body parts, i.e., head, shoulder, elbow, and knee, are defined as the reference. Figure 4.3 shows these reference parts.

Figures 4.4 show the reconstructed radar models for the dummy (DU) and the persons under test (A) to (E) based on the measured data in different radar viewing angles, respectively. It should be mentioned that the abbreviation "DU" and "PA" to "PE" in this Figure are defined for the dummy and the persons (A) to (E). In the measurement setup, the rotation stage turns clockwise around the z-axis in the VRU coordinate system (Figure 4.1), and the rotation angle of $\beta = 0°$ is defined as the direction where the object front is towards the Radar system. The Radar system scanning angles in $\phi = 0°$ and $\theta = 0°$ are aligned to the middle of the body under test. According to the pre-calculated TH value for the test environment, the figures are plotted for scattering points with RCS values higher than -35 dBsm.

The depicted radar models of the dummy and test persons in Figures 4.4 are extracted from measured radar data in the front side ($\beta = 0°$), left side ($\beta = 90°$), back side ($\beta = 180°$), and right side ($\beta = 270°$) of the body, respectively.
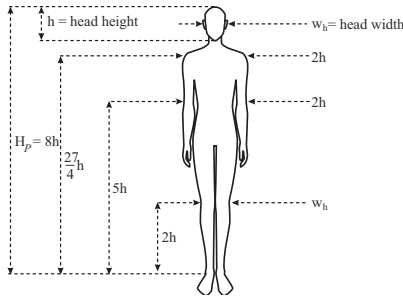
Figure 4.3: The cardboard person [Lan02, JBY96] model to show the details of each region of the human body with respect to the height of the head (h) and its width (w_h). The overall height of the human body (H_P) is 8 heads. The expected height for the shoulders is ($\frac{27}{4}h$) and the shoulder width is 2 times of the head height. The elbows have a height of 5 heads and a width of 2 heads. The knees height is 2 times of the head height and their width is equal to the width of the head (w_h) (Figure based on [1], ©IEEE).

Although different rotation angles of the person (A) and dummy have been measured and investigated, for the sake of clarity, only their extracted radar models at the mentioned sides are shown, here. It is observed that the contour and the orientation of persons or dummy under test can be interpreted from the extracted models.

The back-scattering behavior of the human and the dummy can be examined comparatively from the depicted radar models in Figures 4.4(DU) and (PA) for the dummy and person (A) in their different side views (stage rotation angles of $\beta = 0°, 90°, 180°$, and $270°$). Their extracted radar models are considered at similar sides with the corresponding SPs, and subsequently, the estimated RCS values of the extracted SPs in $\mathbf{OL}_{\text{OUT}}(\beta_j)$ matrix are investigated. Table 4.1 lists the maximum RCS values from the extracted radar models in the mentioned sides of the dummy and person (A). Considering the depicted radar models of the person (A) and its dummy in the front, left, back, and right views, their outlines and orientations can be seen very well in each view. Furthermore, the examined $\mathbf{OL}_{\text{OUT}}$ matrix of the person (A) and its dummy show a good agreement between the estimated RCS values for their SPs.

Table 4.1: The maximum RCS values from the extracted SPs for the dummy human and person (A) in the different viewing angles.

Side view (β)	RCS (dBsm)	
	Dummy Human	Person (A)
Front view ($\beta = 0°$)	-14.5	-14.1
Left view ($\beta = 90°$)	-14.4	-16.9
Back view ($\beta = 180°$)	-15.2	-13.5
Right view ($\beta = 270°$)	-13.6	-16.9

4.2.1 Algorithm for Extracting the Measured Size of Different Human Region

A dedicated algorithm is used to derive the physical sizes of the measured test persons and dummy from their reconstructed models. Furthermore, this algorithm enables assessment process to analyze the extracted positions of the SPs of different human parts. In the next step, the calculated sizes from the measurements can be compared with their actual sizes to analyze the extracted models quantitatively. The utilized fundamental for developing the algorithm is the cardboard model (human body proportions theory) [JBY96, HHD98]. The cardboard model (shown in Figure 4.3) is also the employed model for human tracking in video sensor based systems [SEA06]. This model is defined with reference to the proportions of human body parts [Lan02] which determines the relative positions and sizes of the body parts based on the height of the head (h) with a high degree of accuracy. In the cardboard model, it is presumed that the human body parts can be assumed as a set of connected planar patches [JBY96]. This model estimates the location of each region of the human body to illustrate their height and position details as shown in Figure 4.3. This Figure shows a model of a person in an upright standing situation. The human body proportions theory states that the total height of a person (H_p) is 8 times the head height (h). Then, it defines the location and size of different body regions, i.e., shoulders, elbows, and knees, based on the head height. The shoulders are located at the height of $\frac{27}{4}$ with a width of $2h$. The elbows are placed at the height of around 5 heads, and their width is roughly the same as the shoulder width. Finally, the knees are located at the height of $2h$ with the same as the head width (w_h). The

inputs of the algorithm are the human proportional body model and the 3-D radar model of the person under study, which is extracted from the measured data and combining the extracted $\mathbf{OL}_{OUT,St}(\beta_j)$ matrices over the whole 360°. Then, the algorithm calculates the total height of the human body under test (H_p) from the reconstructed data, which is essential to proceed to the next
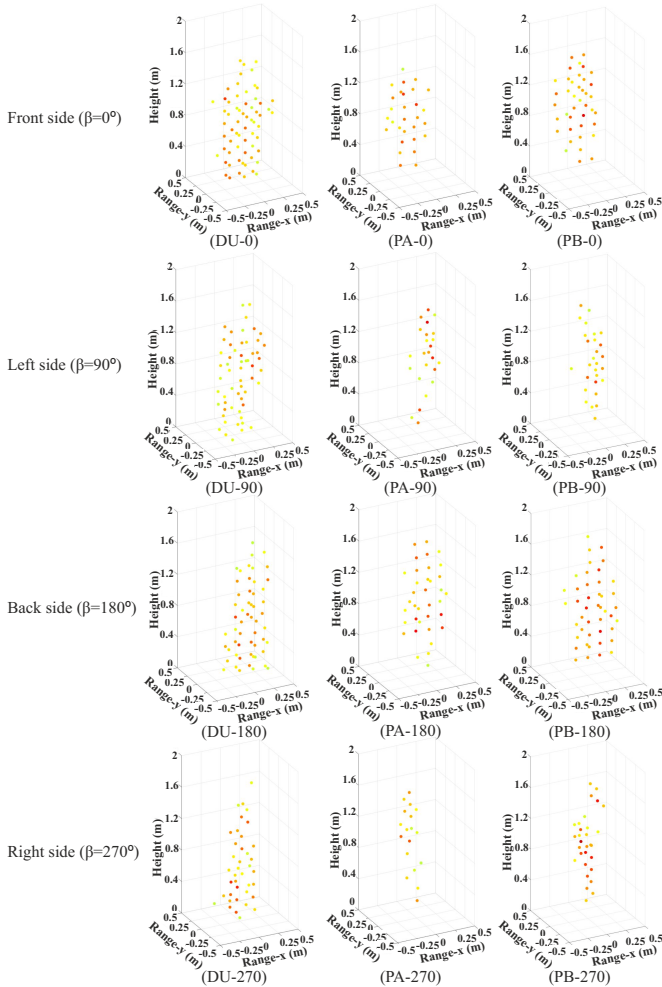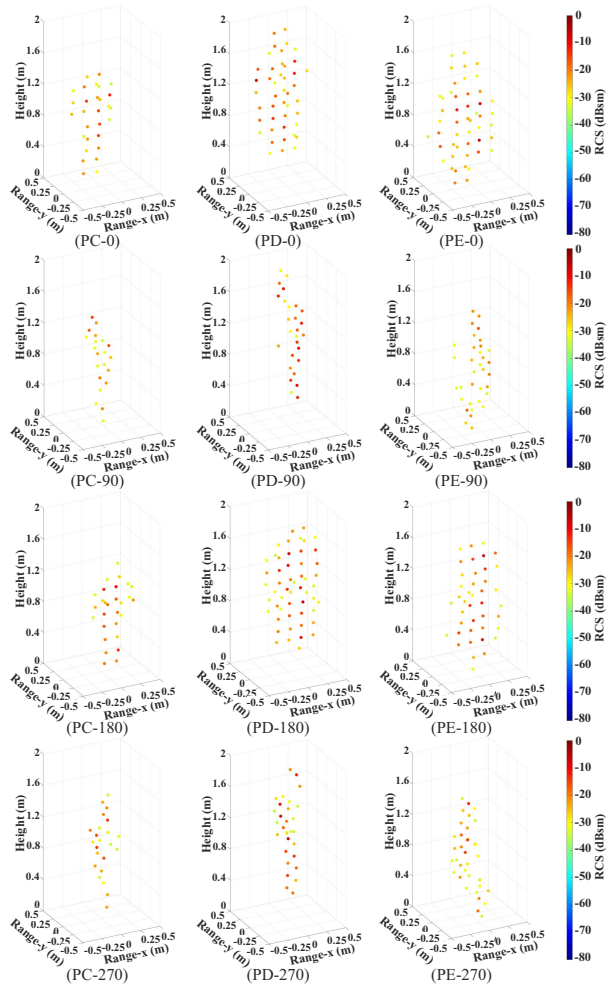
Figure 4.4: Extracted radar models of the different-sized human bodies and dummy human in different views, i.e., front, left, back, and right side. (DU) human dummy; (PA) person (A); (PB) person (B); (PC) person (C); (PD) person (D); (PD) person (E).

steps. In accordance with the explained model, the algorithm approximates the location of the body regions (knees, elbows, shoulders, head) based on their expected heights and searches for the relevant points in the extracted $\mathbf{OL}_{\text{OUT},St}$ matrix. Subsequently, the coordinates of the corresponding right and left sides of each body region ((x_R'', y_R'', z_R'') and (x_L'', y_L'', z_L''), respectively) are specified to determine their width. Figure 4.5 summarizes the signal processing steps of the explained algorithm, which estimates the physical sizes of the measured person.
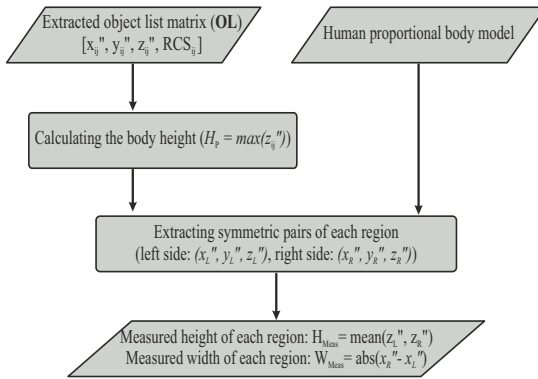
Figure 4.5: Signal processing chain for extracting the measured size of different human region (Figure based on [1], ©IEEE).

The height and width of individual body parts can be calculated from their determined symmetric pairs. The algorithm estimates the height (H_{Meas}) of each region by averaging the height of the region in the left and right sides. It can be followed by

$$H_{\text{Meas}} = \frac{z_R'' + z_L''}{2} \tag{4.10}$$

and concurrently, the width (W_{Meas}) of every region can be estimated by

$$W_{\text{Meas}} = |x_R'' - x_L''|. \tag{4.11}$$

The measured physical sizes of the test persons and the human dummy are calculated from their corresponding radar models for the mentioned points in Figure 4.3. Accordingly, the measured and actual sizes of the measured objects can be found in Table 4.2.

Table 4.2: Comparison of the actual and measured (in parenthesis) physical dimensions of different human objects and dummy human for 76 GHz bis 81 GHz monostatic RCS data collection. (Table based on [1])

Human model	Sizes (cm)						
	Height	Shoulder height	Shoulder width	Elbow height	Elbow width	Knee height	Knee width
DU	170 (173)	136 (138)	42 (34)	111 (107)	48 (32)	52 (43)	21 (16)
PA	170 (163)	144 (148)	40 (32)	103 (116)	47 (47)	50 (53)	21 (16)
PB	173 (181)	147 (135)	44 (48)	112 (118)	50 (48)	54 (54)	20 (16)
PC	158 (156)	134 (124)	43 (47)	94 (108)	45 (48)	47 (45)	18 (16)
PD	192 (199)	165 (152)	47 (48)	126 (136)	52 (48)	57 (56)	30 (32)
PE	180 (177)	149 (145)	45 (48)	115 (130)	58 (48)	60 (66)	30 (32)

From comparing the reported values in Table 4.2, it can be observed that the mismatch between the measured and actual sizes of the body regions has a maximum difference of 16 cm. Considering the HPBW of 1.3° for the Radar system and fixed R in the measurement setup, the expected illuminated area of the body under test is 20 cm × 20 cm. Consequently, the observed tolerance in the measured values in comparison with the actual values are acceptable and is appertained to the measurement resolutions. It is worth emphasizing that

this comparison proves the accuracy of the measurements and post-processing steps.

For a more detailed quantitative analysis, the back-scattering behavior of the test persons is investigated based on their RCS values in the different parts. In that regard, the human body, depicted in Figure 4.3, is divided into three major parts, i.e., head, torso, and legs. The head part contains the region within the range of $7h$ and $8h$. The human body regions within the range of $4h$ and $7h$ are defined as the torso part, and the area within the range of 0 and $4h$ forms the legs part. Then, the RCS values of the related part can be calculated by utilizing the extracted object list matrix ($\mathbf{OL}_{\mathrm{OUT},St}$) for each test person and dummy. The sum of all measured RCS values of the extracted SPs within each body part is introduced as the RCS value of the related part. Table 4.3 lists these values for every test person and the dummy in their different parts. By comparing the calculated RCS values of different parts of the measured human models, it is noticeable that the torso has the strongest influence on the back-scattering behavior of the human body. The next substantial scattering behavior can be attributed to the legs part, and the weakest scattering area in human body parts is related to the head part. Moreover, the comparison between the RCS values of the same body part from different test persons indicates that the bigger body parts result in larger RCS values. As an example, the test person (E) has a larger torso compared to other test persons; therefore, the RCS of its torso is the largest value. On the other hand, the smallest RCS values are attributed to the skinny (A) and kid-size (C) persons, as they have smaller body parts. This comparison illustrates the influence of body size on its RCS value.

In another validation step, the RCS values of each body part in different azimuthal rotation angles β_j are examined by utilizing the extracted object list matrix in the corresponding viewing angle ($\mathbf{OL}_{\mathrm{OUT},St}(\beta_j)$) for the human dummy and person (A). The calculated RCS values are shown in Figures. 4.6 for the dummy and the person (A), respectively. It should be mentioned that the Dummy human is scanned with $\Delta\beta = 10°$ in the azimuthal direction and the person (A) with $\Delta\beta = 30°$. These Figures clearly demonstrate that the most considerable RCS value is obtained at $\beta = 180°$, which means the strongest scatterings occur in the back side. Furthermore, it can be observed that the smallest RCS values in every part come from the side views, which corresponds to $\beta = 90°$, and $270°$. These results are expected in accordance with the presented results in the lite-

Table 4.3: The corresponding RCS values of three body parts, i.e., head, torso, and legs, from different measured human objects and dummy human for 76-81 GHz monostatic RCS data collection. RCS values of the related body parts are the summation of the measured RCS values for the extracted SPs inside each part. (Table based on [1])

Human model	RCS (dBsm)		
	Head	Torso	Legs
DU	-19.1	-7.6	-9.4
PA	-15.8	-8.3	-8.2
PB	-10.3	-4.8	-6
PC	-16.1	-7	-9.8
PD	-8.7	-2.6	-6.8
PE	-12	-1.4	-3.8
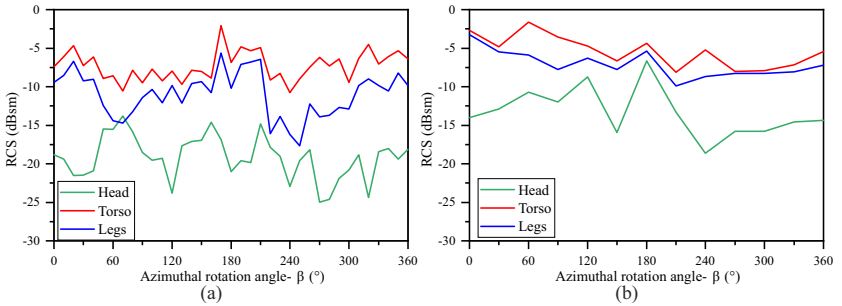
Figure 4.6: The corresponding RCS values of three body parts, i.e., head, torso, and legs, of (a) the dummy human (Figure based on [1], ©IEEE) (b); person (A); in different azimuthal rotation angles (β). The values are the summation of different scattering points within the corresponding region.

rature, and the calculated RCS values for different parts are in good agreement with the reported values in [CC14].

A more detailed comparison in the back-scattering behavior of the person (A) and dummy is provided by inspecting the RCS values of their similar body parts. The investigation of the extracted **OL** matrix for the person (A) and dummy shows that their individual body parts have similar RCS values with a

maximum 2 dB difference. As an example, the extracted RCS value for the right elbow of the human and dummy are -20.0 dBsm and -21.0 dBsm, respectively. On the basis of these results, it can be deduced that person (A) has a similar back-scattering behavior with its similar size dummy. Hence, the dummy can be utilized in the measurement setup with a real human, especially in higher-resolved measurements where the measurement time exceeds several hours. Another advantage of conducting the measurements with a dummy is removing the measurement inaccuracy caused by the unintentional movement of the test persons. Eventually, it can be concluded that the human can be replaced with the dummy in the measurement scenarios for VRUs. That paves the road for the future, where more complex and time-consuming test scenarios should be examined without needing a person as an object.

4.3 Extracted Radar Model of Non-human VRUs in Static Situation

The next step in a more realistic traffic environment modeling is developing the radar model of the other VRUs, which are common in typical traffic scenarios. In this concept, the high-resolution RCS measurement technique is extended to other road users, e.g., motorcycles, bicycles, and cars, in static situations. Besides, the extracted radar models can be employed to study the viability of the proposed measurement technique. As explained previously in Section 4.2.1, the rider of the motorcycle and bicycle can be replaced by the dummy human in the RCS measurements. Therefore, it is possible to perform the angular resolved RCS measurements for a motorcyclist and cyclist over the whole 360° azimuthal rotation angle with an adjustable step width of $\Delta\beta$).

Figures 4.7(a) and (b) show the dummy motorcyclist and cyclists in the measurement setup, respectively. In Figure 4.7(a), the dummy rider of the motorcycle (Honda 900 Hornet) is dressed up in a motorcycle combi suit, and the geometrical size of the object under test is 2.2 m×0.8 m×1.96 m ($L\times W\times H$). The dummy bicyclist in Figure 4.7(b) has the physical dimensions of 1.7 m×0.65 m×1.55 m. The scanning area of the Radar system in the azimuth and elevation directions fully covers the area of interest with an angular resolution of 1°. The dummy motorcyclist and bicyclist are mounted on the turntable, which can rotate with the azimuthal resolution angle of $\Delta\beta = 10°$. These configurations enable
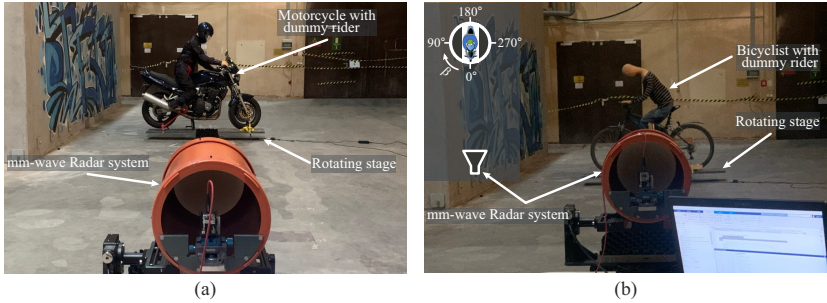
Figure 4.7: Setup for monostatic RCS measurement of motorcyclists and bicyclist to extract their radar model (OUT is placed on top of the rotating stage for extracting its scattering points); (a) dummy rider of Honda 900 Hornet motorcycle in radar viewing angle of 270°, (b) dummy rider of a bicycle in radar viewing angle of 90°.

the measurement setup to detect the scattering points of the mentioned VRUs depending on their azimuthal rotation angle (β) and, subsequently, investigate their full azimuthal radar model. Additionally, these RCS measurements are conducted for the motorcycle and bicycle in the absence of the dummy rider. The corresponding scattering points of the motorcycle and motorcyclist are shown in Figures 4.8 at four main sides of the objects under test. Figures 4.9 determine the location of the scattering points and their RCS characteristics over the body surface of the bicycle and bicyclist. The center of the objects under test corresponds to the range of 0 m. The starting rotation angle of the Radar system ($\phi = 0°$ and $\theta = 0°$) is towards the middle of the objects. The depicted radar models are related to the front side ($\beta = 0°$), left side ($\beta = 90°$), back side ($\beta = 180°$), and right side ($\beta = 270°$) of the objects under test. It is worth emphasizing that the riders in the measurement setups of Figures 4.7 bend on the motorcycle and bicycle to have a proper body position similar to a real rider. Therefore, the number of extracted scattering points of the riders from the front and the back view is less in comparison to the extracted radar model of the measured persons in a standing situation and the same viewing angles. It is especially observable for the extracted radar models in Figures 4.8 and 4.9 for viewing angles $\beta = 0°$ and $180°$.

For extracting the radar model of a typical car (BMW X 1), the high-resolution RCS measurement setup is conducted for collecting its backscattering behavior,
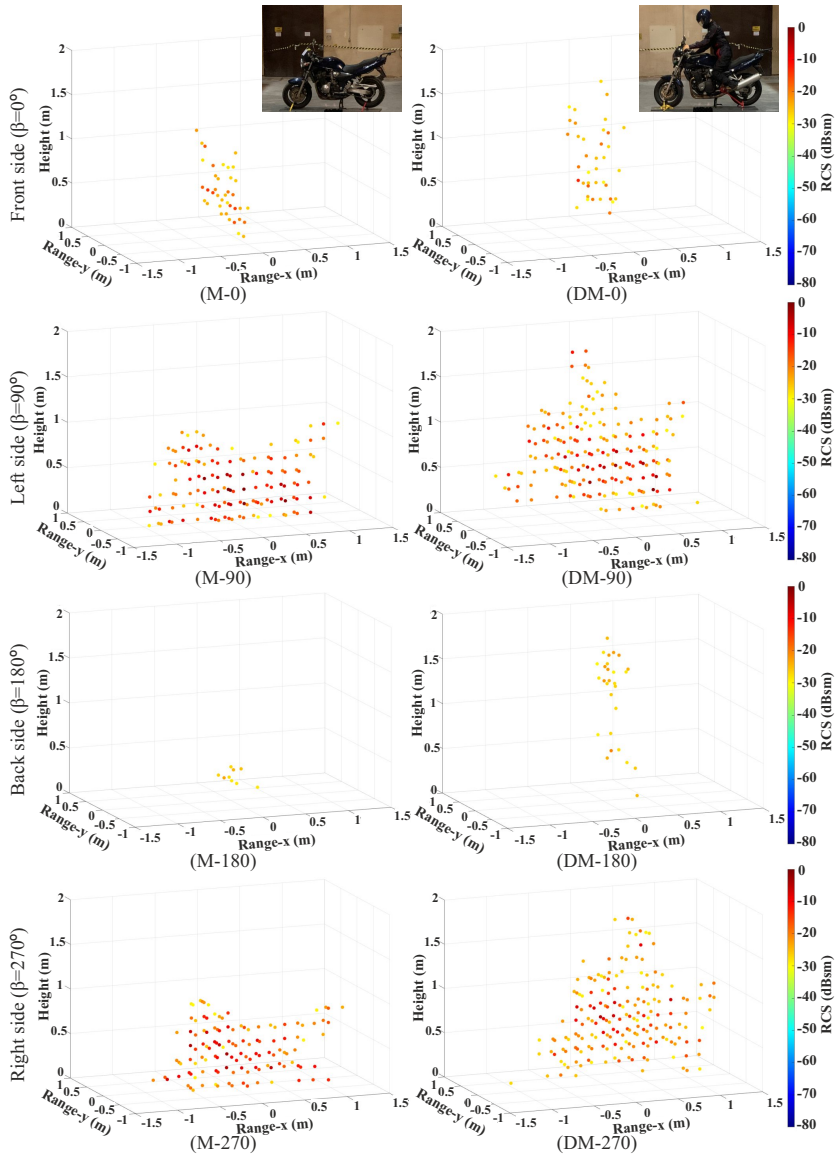
Figure 4.8: Extracted radar model of a motorcycle (M) and a motorcycle with its dummy rider (DM) in different views, i.e., front, left, back, and right side. The insets show the photographs of the corresponding objects as the reference.
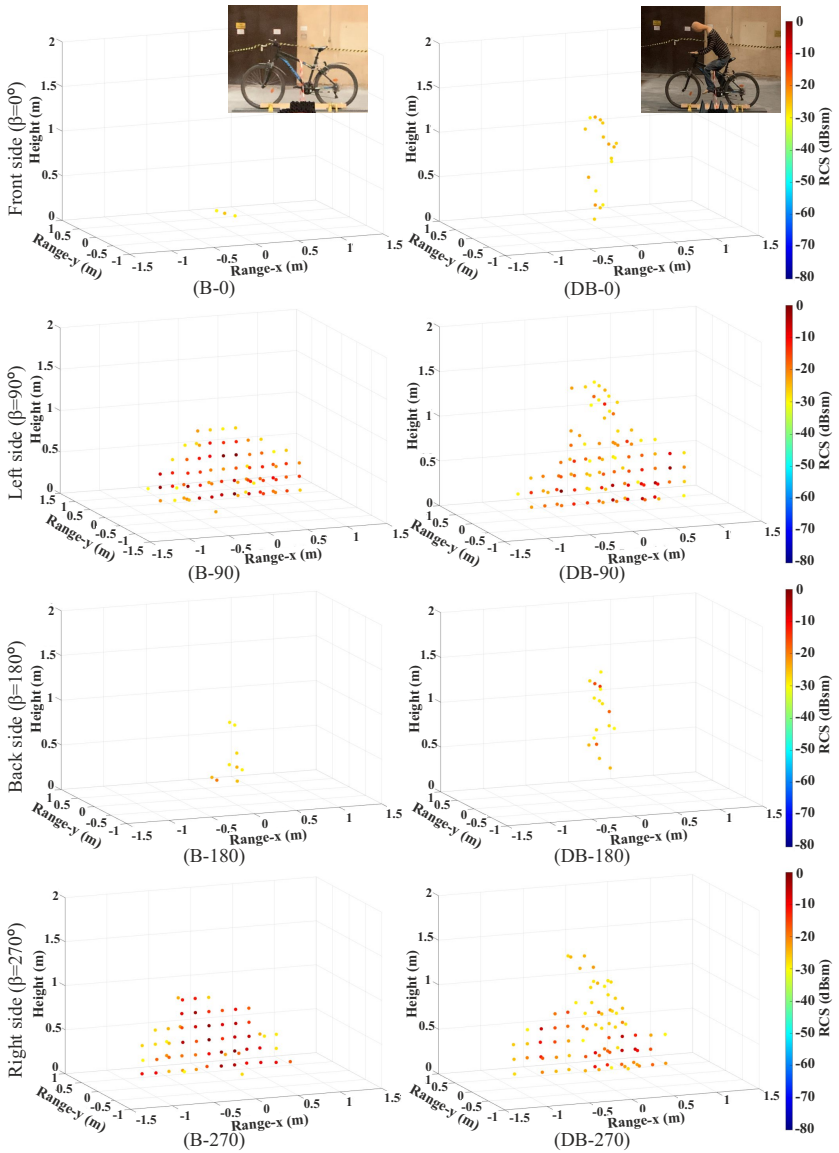
Figure 4.9: Extracted radar models of a bicycle (B) and a bicycle with its dummy rider (DB) in different views, i.e., front, left, back, and right side. The insets show the photographs of the corresponding objects as the reference.

as shown in Figure 4.10(CS). Considering the physical sizes of the car, $4.45 \, \text{m} \times 2.0 \, \text{m} \times 1.61 \, \text{m}$, the measurement is performed in the anechoic chamber of the European Microwave Signature Laboratory (EMSL), Joint Research Center of the European Commission (JRC), Ispra, Italy. In this measurement setup, the measured calibration factor for RCS normalization is $-0.75 \, \text{dBsm}$. It is calculated from the collected measurement data for a TCR with the inner height of $a = 10 \, \text{cm}$. In the next step, the test environment is characterized by measuring the reflected signal levels from the test environment in the absence of the object under test. In the clutter level measurement, the rotating stage moves in the same direction and step width as the RCS measurement with VRUs. The maximum calculated RCS values in each elevation angle of the Radar system (θ) and the azimuthal rotation angle of the stage (β) can be introduced as the clutter level. Then, the clutter level matrix ($\mathbf{CL}(\beta_j)$) from the collected data and calculated object list matrix ($\mathbf{OL}(\beta_j)$) is introduced by

$$\mathbf{CL}(\beta_{\mathbf{j}}) = \begin{bmatrix} \theta_{1j} & \text{RCS}_{1j} \\ \vdots & \vdots \\ \theta_{ij} & \text{RCS}_{ij} \\ \vdots & \vdots \\ \theta_{Pj} & \text{RCS}_{Pj} \end{bmatrix}. \tag{4.12}$$

Afterward, the threshold level corresponding to each β_j and θ_{ij} is determined for later postprocessing.

The car is positioned on the rotating stage in the measurement setup to scan it in different azimuthal rotation angles. Accordingly, the center of the car is placed in the range of $R = 9 \, \text{m}$ from the antenna feed of the Radar system. The rotating stage moves counter-clockwise to scan it with the favorite azimuthal resolution angle ($\Delta\beta = 10°$) so that the azimuthal rotation angle of $\beta = 0°$ corresponds to the front view of the car. The mechanical specification of the measurement setup authorizes the Radar system to scan the whole dimension of the car in elevation and azimuth direction with a step width of $1°$. The extracted radar models of the measured car are shown in Figures 4.10(C-0), (C-90), and (C-180) from the front, side, and back views, respectively.
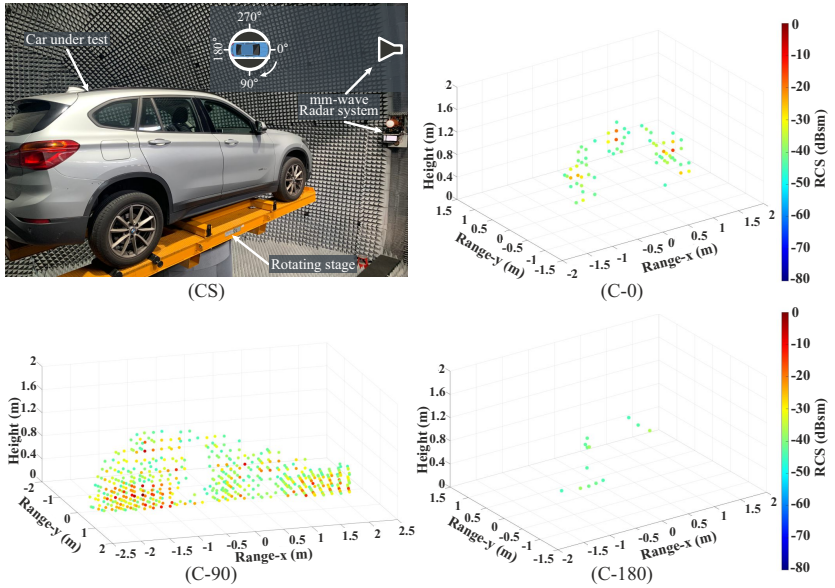
Figure 4.10: (CS) Setup for monostatic RCS measurement of a typical car (C) to extract its radar model. A BMW X 1 is placed in the measurement setup. Extracted radar models of a typical car in (C-0) front view (β =0°); (C-90) side view (β =90°); (C-180) back view (β =180°). The insets also show the photographs of the corresponding objects as the reference. The center of the objects under test corresponds to a range of 0 m. The starting rotation angle of the Radar system (ϕ =0° and θ =0°) is towards the middle of the objects.

The examination of the radar models for full azimuthal rotation angles of the measured objects, i.e., a motorcycle with and without its motorcyclist, a bicycle with and without its cyclist, and a car show that the approximate outline, orientation, and actual sizes of the measured objects can be predicted from the measurement results. Therefore, their extracted radar model can explain their backscattering behavior to use as their radar model in wave propagation simulations. Moreover, the depicted exemplary radar models in Figures 4.8, 4.9, and 4.10 reveal the capability of this technique to differentiate between various VRUs. That means that these models can also be utilized for target classification.

Finally, the discussed investigations and analysis lead to the conclusion that the profile of each object under test is recognizable through the distribution of the SPs. The extraction of SPs is achievable by the employed Radar system in the measurement setup, which enables the preparation of the radar image of the objects under test. As discussed in Chapter 1, this capability of the proposed measurement technique is usable in target classification, more importantly when the significant RCS contributions are considered in conjunction with micro-Doppler signatures. Chapter 5 discusses developing radar models based on the measured RCS and micro-Doppler signatures of the object under test. In view of the fact that different VRUs have distinct spans in the azimuth and elevation directions and besides the extracted radar images containing data in the same directions; therefore, capturing the shape and size of the objects under test is achievable from the measured radar images. For example, a bicycle, motorcycle, or vehicle have a more significant extension in the azimuth direction and a smaller extension in the elevation direction than a pedestrian.

4.4　Comparative Analysis for Extracted Radar Model of Motorcyclists

Reliably and precisely modeling VRUs, such as motorcyclists with many possible variations, is crucial in the virtual simulation environment. As a result, this confirms the consistency between virtual evaluation and reality. This goal can be achieved by comparing the backscattering behavior of different types of one exemplary group of VRUs. Since a VRU with an agile behavior in traffic scenarios can still arise challenges in the simulation environment, analyzing the backscattering behavior of this group of VRUs is worthwhile. For this purpose, this section presents the measured radar models of a motorcyclist who drives different types of motorcycles to examine its backscattering behavior based on the type of motorcycle. Furthermore, this investigation helps to find out the necessary number of measurements in each VRUs group to prepare a reliable radar model for each group of VRUs. Subsequently, it causes a decrease in the residual risk associated with the functionality of the models in wave propagation simulations and machine learning algorithms.

In this context, the high-resolution RCS measurement technique is utilized to collect the radar data from a motorcyclist with three different types of motorcy-

cles, i.e., classic (Honda 900 Hornet), sport (MV Agusta), and cross (Honda XL 250S). The radar models of the measured objects are computed to thoroughly analyze their radar signatures, i.e., SPs and their RCS values. These measurements are conducted in the anechoic chamber of the European Microwave Signature Laboratory (EMSL)- JRC, as discussed for measuring the SPs of the car in the previous section. Figure 4.11 shows an exemplary setup for these measurements. As explained in Section 4.3, a dummy motorcyclist has similar backscattering behavior to a real motorcyclist of the same size. Hence, during the full azimuthal angular resolved RCS measurement, a human motorcyclist can be replaced by a dummy motorcyclist dressed in a motorcycle combi suit. The dummy motorcyclist is fixed on different types of motorcycles, and these combinations are placed on the rotating stage, which moves counter-clockwise with an azimuthal resolution angle of $\Delta\beta = 10°$. The dummy motorcyclists are positioned at the range of R = 9 m in the test setup. Then, the setup configurations enable the Radar system to scan the dummy motorcyclist with a step width of 1° in elevation and azimuth directions and 180° azimuthal angle scanning range from the front to the rear. It is assumed that the object under test is perfectly symmetric along its longitudinal axis.
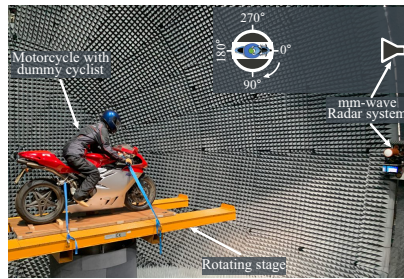
Figure 4.11: Setup for monostatic RCS measurement of motorcyclists with different types of motorcycles to extract their radar model. The dummy motorcyclist is placed on top of the rotating stage to extract its scattering points. The utilized motorcycle in this picture is MV Augusta inside the anechoic chamber of JRC, Ispra.

The extracted radar models of the motorcyclist with each type of motorcycle are shown in Figures. 4.12 from the front, side, and back views, respectively. The front and side views of the motorcyclists correspond to the azimuthal rotation angle of $\beta = 0°$ and $\beta = 90°$. The orientation of the rider with each

motorcycle can be correctly interpreted from the depicted figures. In addition, the outline of the motorcyclist is recognizable from the extracted radar images in Figures. 4.12, which can help to distinguish different types of motorcycles.

In the first step, the measured dimensions of the motorcyclist (from its reconstructed model) are investigated in comparison with its actual sizes based on the motorcycle types. This evaluation is performed at every viewing angle of the radar, and its results are beneficial to study the models quantitatively. The actual physical sizes of the motorcyclists ($L \times W \times H$) with their corresponding measured dimensions can be found in Table 4.4 based on the utilized motorcycle types. The measured and actual sizes are in good agreement with each other considering the discussed measurement accuracy in Section 4.2.1.

Table 4.4: Comparison of the actual and measured physical dimensions of the dummy motorcyclist ($L \times W \times H$) with different type of motorcycles from the extracted radar model over the whole 360° azimuthal rotation angles.

Motorcycle type	Sizes (m)	
	Actual	**Measured**
Classic (H)	$2.2 \times 0.8 \times 1.96$	$2.5 \times 0.95 \times 1.89$
Sport (MV)	$1.9 \times 0.8 \times 1.7$	$1.93 \times 0.78 \times 1.42$
Cross (HXL)	$2.17 \times 0.87 \times 1.85$	$2.11 \times 0.94 \times 1.58$

In the next step, the influence of the motorcycle type on the backscattering behavior of the motorcyclist is inspected. For this purpose, the maximum and summation of the RCS values for the extracted SPs in each azimuthal rotation angle are computed and are shown in Figures 4.13, respectively. It can be realized that the motorcyclist with a classic and cross motorcycle has a more robust reflectivity behavior than riding a sport type. It is matched with the expected scattering behavior considering the physical sizes and the material used in their structure. The utilized classic and cross motorcycles have more significant dimensions than the sporty type, and their structures contain more metallic materials. For a more detailed analysis, the data related to the summation of the RCS values in Figure 4.13(b) are examined for their difference in similar viewing angles. The maximum reported difference is 5 dB. Furthermore, it is observed that the SPs in the extracted radar models have approximately similar RCS values. Therefore, it can be concluded that motorcyclists with different
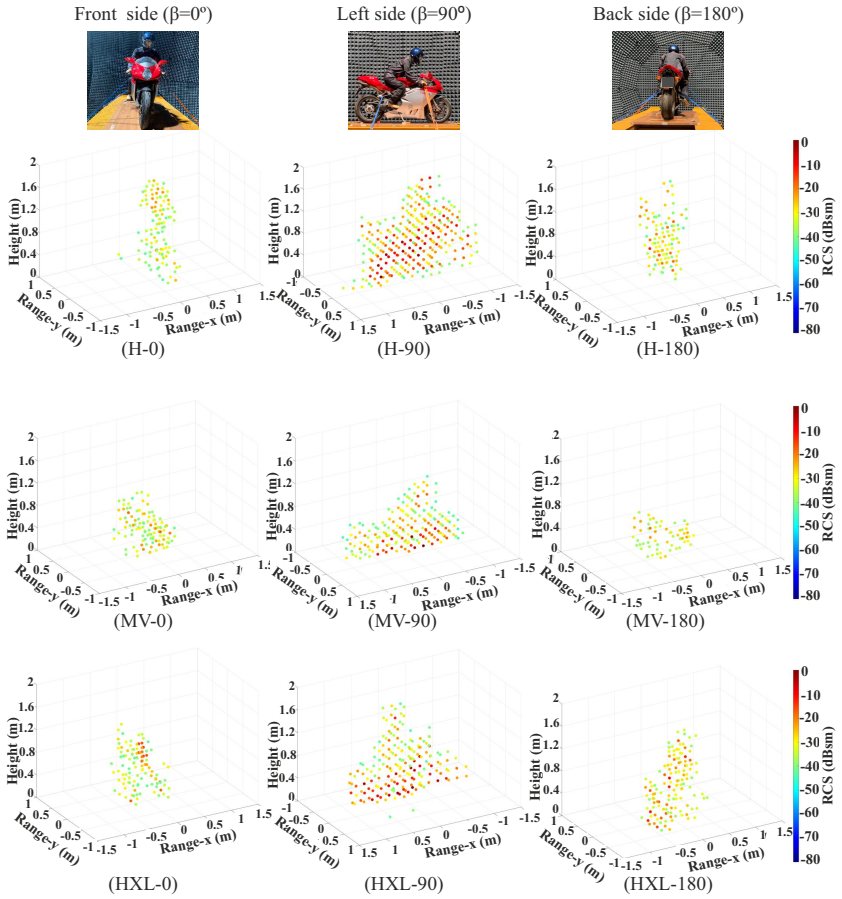
Figure 4.12: Extracted radar model of a motorcyclist on the different types of motorcycles; (H) classic (Honda 900 Hornet), (MV) sport (MV Augusta), (HXL) cross (Honda XL 250 S) in front (β =0°), side (β =90°), and back (β =180°) views. On top, the corresponding orientations of the motorcyclist are shown as a reference. The center of the motorcyclist corresponds to a range of 0 m. The starting rotation angle of the Radar system (ϕ =0° and θ =0°) is towards the middle of the objects. (Figure based on MWCL2022, ©IEEE).

types of motorcycles in the traffic scenarios have analogical backscattering behavior.
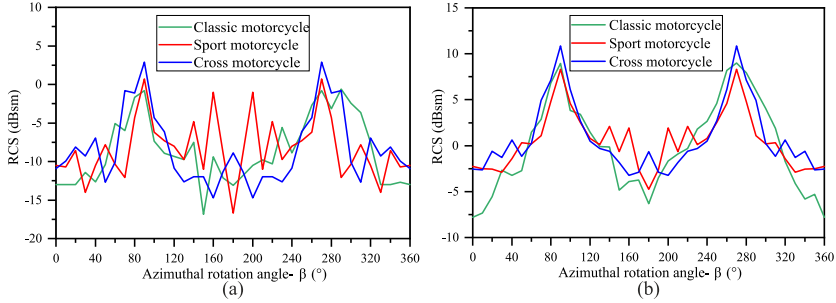
Figure 4.13: The corresponding (a) maximum RCS values, (b) summation RCS values of the motorcyclist with different types of motorcycles in different azimuthal rotation angles (β). (Figure based on MWCL2022, ©IEEE).

For a more detailed comparison, the RCS patterns of the measured motorcyclists are computed from the extracted radar models. This pattern shows the RCS characteristics of the target when it is assumed as a single-point scatterer. A dedicated algorithm is used to accumulate the RCS values of multiple scattering points for the object under test in every viewing angle and presents its RCS patterns. The algorithm has two inputs, and its employed signal processing chain is shown in Figure 4.14. The primary input of the algorithm ($\mathbf{OL}_{\text{OUT},St}(\beta_j)$) is the calculated $\mathbf{OL}$ matrix of the object under test, which is extracted from high-resolution RCS measurements in different azimuthal rotation angle (β_j). Another input of the algorithm is the normalized two-way radiation pattern of the radar sensor [$C_{ij}(\varphi_{ij}, \theta_{ij})$], which is measured in the absence of the high focusing lens. Then, the algorithm utilizes the radar scanning area information (φ_{ij} and θ_{ij}) from $\mathbf{OL}_{\text{OUT},St}(\beta_j)$ and $C_{ij}(\varphi_{ij}, \theta_{ij})$ to generate CF_{ij}. It is a correction factor of the received signal level ($\overline{sl}_{ij}$) of each SP in the corresponding angles of φ_{ij}, θ_{ij}, and β_j.

After that, the algorithm adds all these values together to produce the complex signal level of the object $\overline{sl}(\beta_j)$ in the related radar viewing angle (β_j). One more calibration factor (ΔSL) is used to enable the correct estimation of the signal magnitude in each radar viewing angle as a single point scattering object ($\mathbf{SL}(\beta_j)$). ΔSL is the difference between the measured signal levels for a
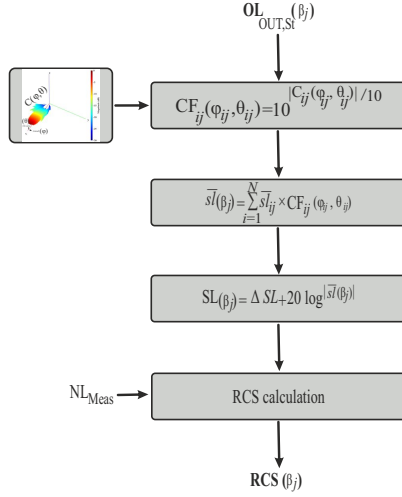
Figure 4.14: Signal processing chain for computing the RCS pattern of the measured object from its calculated **OL** metrics in different azimuthal rotation angles (β_j). (Figure based on MWCL2022, ©IEEE).

standard TCR in the absence and presence of a focusing lens antenna. These calibration measurements are performed for a TCR with an inner height of $a = 10$ cm and positioned in the main beam of the radar or Radar system. The estimated ΔSL is 41 dB, and it should be noted that ΔSL is independent of the measured size of the TCR. The algorithm estimates the RCS value in each azimuthal rotation angle (**RCS**(β_j)) by utilizing the measured noise level in Section 3.6 and radar equation. By comparing Equation 3.7 and 3.8, **RCS**(β_j) can be calculated by

$$\mathbf{SNR}_{\text{Meas}}(\beta_j) = \frac{\mathbf{SL}(\beta_j)}{N_{\text{Meas}}} \tag{4.13}$$

$$\mathbf{RCS}_{\mathrm{Meas}}(\beta_j) = \frac{(4\pi)^3 \; R^4 \; k \; T_{\mathrm{abs}} \; \mathrm{NF}}{P_{\mathrm{Tx}} \; G^2_{\mathrm{radar}} \; T_{\mathrm{Sweep}} \; \lambda^2} \mathbf{SNR}_{\mathrm{Meas}}(\beta_j) \qquad (4.14)$$

where G_{radar} is 20 dBi as discussed in Section 3.3.
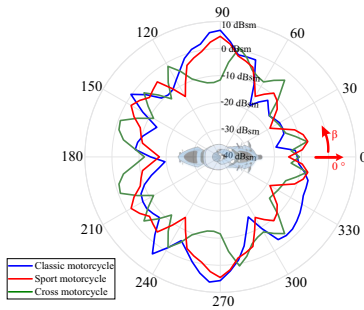
Figure 4.15: Estimated RCS pattern of the measured motorcyclist from its extracted SPs in different azimuthal rotation angles (β) and with different types of motorcycles. (Figure based on MWCL2022, ©IEEE).

The approximated RCS patterns of the motorcyclist are depicted in Figure 4.15 based on the types of riding motorcycles. From comparing the patterns, it can be noticed that the motorcyclist has a higher RCS value in the side views ($\beta = 90°$ & $270°$) than the front or back views ($\beta = 0°$ & $180°$). This observation is the expected result. Figure 4.15 shows that the RCS values of the motorcyclist, as a single point scattering, are within the range of -20 dBsm to 7 dBsm which are in good agreement with the reported values in the literature [GCB+13, KPB+09,KHBS13]. The discussed evaluation in this section leads to the finding that the motorcycle type is not an influential factor for predicting the overall reflectivity behavior of the motorcyclist and only affects the level of the RCS values in different viewing angles. Therefore, it is not necessary to measure the different types of VRUs in each group of VRUs for developing realistic radar models. Instead, it is sufficient to prepare a generic-realistic radar model for one of the types and utilize it as an accurate model in wave propagation simulations.

5 Radar Signature Characterization of VRUs in Motion

Modeling the movement of a person in different poses, especially as a pedestrian or a rider of motorcycles and bicycles, is crucial in the current evolvement of OTA test methods for validating the operational behavior of automotive radar sensors. This group of radar targets contains a large and critical variety of VRUs in developing the safety assurance for ADAS. Their realistic radar models can be achieved by assigning the extracted RCS values to specific micro-Doppler signatures of human motion from the extremities. It is the main motivation for evaluating the range-Doppler behavior of human movements and extracting the RCS and Doppler signatures from the human extremities. The high-resolution RCS measurement in the radial and angular domains is the technique that can be utilized to retrieve the RCS and Doppler signatures of human motions. These data can be applied to micro-motion models of human extremities and significantly improve the radar model of a human in movement.

Therefore, this chapter proposes a measurement technique to estimate the radar reflectivity of human body regions in combination with their dynamic description. This measurement technique amalgamates the high-resolution RCS measurement with the MoCap technology to extract the radar signatures, e.g., range-time, Doppler-time, and range-Doppler, of each scattering point on human body regions. The radar reflectivity of the body regions can be determined by investigating their backscattering behavior based on the extracted scattering points modeling, which is presented in Chapter 4. In this context, the Radar system scans a volunteer person with various human motions. The test person is dressed with MoCap cloth, and the MoCap trackers are attached to previously defined body regions. Then, the collected radar raw data is analyzed by the discussed EFE algorithm in Section 2.3.2 for highly accurate range and either Doppler frequency or velocity characteristic of human activities. Accordingly, this enables assigning the corresponding RCS values and Doppler signatures to the time-varying scattering points originating from a human body's different

extremities and developing a precise radar model of human motions. The Mo-Cap technology is utilized to simultaneously collect human motion data, which its details are explained in Section 5.1.3.

The proposed measurement technique is the first work that combines RCS values of body regions with a micro-Doppler signatures, which is a valuable strategy since the human body can generate high number time-varying scattering points. Modeling based on raytracing methods can not represent these effects in real-time due to excessive computational requirements. This novel approach can generate highly-accurate realistic models of a human in motion for employing in radar channel wave propagation simulations, target recognition, and classification and besides improve VRUs safety.

5.1 Human Motion Parameter Estimation with Radar Signals

Small motions of an object and even its components give rise to micro-Doppler signatures in response to an active emitter such as radar, laser, and even acoustic emitters [PvD08, PJM$^+$14]. In the presence of radar illumination, these micromotions can be observed through the Doppler scattering returns produced by the motions. Human movements in different poses cause micro-motions in the human body regions, which have distinctive micro-Doppler signatures in the reflected signal from the corresponding area. Therefore, human motions can be examined by analyzing the Doppler modulations in radar signatures and subsequently employed for modeling human body parts movements. Similar to the human body modeling in a static situation, the body regions of a human in motion can be modeled as a collection of the time-varying scattering points distributed over the body regions. It means that the measured range to different human body regions, $R_{\mathrm{m}}(t)$, is not constant. These measured ranges swing around R despite assuming that the targets are moving radially toward the Radar system. Accordingly, the estimated range of body parts can be described by a combination of different swing frequency $f_{\mathrm{m}'}$ and amplitude $A_{\mathrm{m}'}$ as

$$R_{\mathrm{m}}(t) = \mathrm{R} + \sum_{\mathrm{m}'} A_{\mathrm{m}'} \cos(2\pi f_{\mathrm{m}'} t) \tag{5.1}$$

where R is radial distance between the radar sensor and the center of the object under test at stationary.

5.1.1 Range and Doppler Determination Using High-Resolution mm-Wave Radar Sensor

The high-resolution monostatic RCS measurement setup is used to determine the RCS and micro-Doppler signatures of the human body regions in motion. The discussed fundamentals in Section 2.3.2 are employed to present the radar signature extraction method from the collected radar raw data in the following sections. For this purpose, the collected IF data is evaluated in the fast-time direction of the stored radar data matrix. The higher measurement rate in the fast-time axis, compared to the slow-time axis, enables the technique to resolve the spatial sensing of multiple simultaneously moving scattering points of an extended object under test.

A combination of two discussed analysis techniques in previous chapters, the EFE technique in Section 2.3.2 and angular resolved RCS measurement in Chapter 3, enables the determination of RCS values from the radar target with high resolution in range and also the velocity. Moreover, the assigned rotational feature to the focused antenna of the Radar system (Table 3.1) attributes the measurement setup to have a high resolution specification in the azimuth and elevation. Consequently, the proposed measurement setup in Section 5.2 is capable to present a highly resolved range-velocity information of each part of a moving body.

5.1.2 Verification of the Utilized Enhanced Frequency Evaluation Algorithm

A dedicated radar measurement with a moving standard target is performed to validate the EFE technique in the analysis of the measured data. This measurement investigates the accuracy of the technique for extracting the range-velocity information of the radar target. The utilized measurement setup is illustrated in Figure 5.1, which includes a linear magnetic track and a moving carriage. A standard TCR, with the inner height $a = 19.9$ cm, is mounted onto a moving

carriage that can move on the linear magnetic track with controllable velocity and acceleration. The TCR moves away from the installed Radar system, which is positioned in front of the linear magnetic track so that its center is aligned with the main beam of the Radar system. Then, the TCR travels 1.5 m along the linear magnetic track which has a maximum displacement range of 2.8 m. The technical specifications of the linear magnetic track are summarized in Table 5.1.
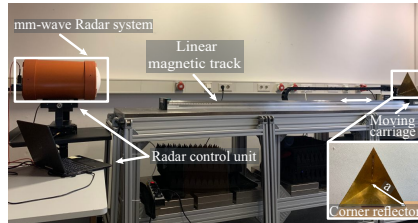
Figure 5.1: Setup for extracting the range-velocity information using a TCR, which can move on the linear magnetic track to verify the EFE algorithm. The TCR is aligned to the main beam of the Radar system. (Figure based on [2], ©IEEE).

In this experiment, the carriage is accelerated to a velocity of $v = 2\,\mathrm{m/s}$ and the Radar system is configured to operate with triangular chirps consisting of 200 ramps with the full ramp period of 5 ms. After that, the carriage continues the movement with a constant velocity, and subsequently, the movement is decelerated with $10\,\mathrm{m/s^2}$ to stop at the end of the trajectory. The maximum number of ramps and the ramp period are assigned in the radar configuration so that the radar measurement time is long enough to evaluate the movement processes of the carriage from the radar data.

In order to validate the utilized EFE algorithm for analyzing the measured radar data, the extracted range-velocity information from the discussed experiment are depicted in Figure 5.2. The movement process of TCR can be realized from the extracted range-velocity and velocity-time information in Figures 5.2(a) and (b), respectively. They reveal that the moving target is placed at the range of 2.52 m to the Radar system at the beginning of the process. After initiation of the moving process, the TCR is displaced 1.5 m and stopped in the range of 3.77 m, which corresponds to the chirp number of 67. Figure 5.2 demonstrates two steps of the

Table 5.1: Linear magnetic track technical specification.

Parameter	Magnetic Track Specification
Maximum displacement range	2.8 m
Positioning repeatability	1 µm
Maximum velocity	5 m/s
Maximum acceleration	30 m/s^2

moving process, i.e., moving with constant velocity and deceleration. Firstly, the TCR is moved with a constant velocity of 2 m/s and a standard deviation of 0.023 m/s. In the last 0.36 m of displacement, the movement is decelerated with 9.9 m/s^2. The performed experiment and plotted results of the algorithm verify that the estimation of the range and velocity information of moving radar target is accurately achievable by utilizing the EFE algorithm on fast axis data.
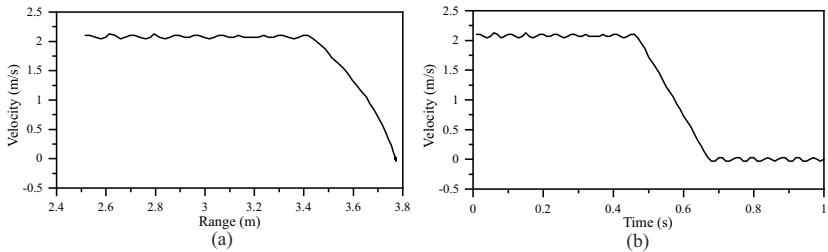
Figure 5.2: Measured radar data of the moving TCR to validate the utilized EFE technique. The TCR is moved with a constant velocity of 2 m/s for 1.14 m and decelerated with 10 m/s^2 for 0.36 m. (a) The velocity-range information of the moving TCR. (b) The calculated velocity of the TCR using the Doppler information from EFE algorithm. (Figure based on [2], ©IEEE.)

5.1.3 Capturing Human Motion

Motion capture (MoCap) is the technique of recording human, animal, or rigid body movements via computers [KW08]. In general, there are three different categories of motion capture systems based on their structure of sensors and data sources. First, inside-out systems use sensors inside the capture volume and external data sources. An example is electromagnetic systems, where sensors attached to a human body move in an externally generated electromagnetic field. Second, inside-in systems use sensors inside the capture volume as well as internal data sources. An example is inertial system, where inertial measurement units (IMUs) are attached to a human body and work as sensors, whereas the body joints can be seen as data sources. The third category is outside-in systems, where sensors are outside, and data sources are inside the capture volume. An example of this category is the optical system, where cameras are the sensors and markers are the data sources [Men11].

The utilized MoCap technique in this work employs NaturalPoint's OptiTrack tracking systems to collect human motion data, which is classified as an outside-in system. NaturalPoint's OptiTrack tracking systems are the industry-leading precision optical motion capture and 3-D tracking systems. This system utilizes the Prime^{X}13 cameras and retro-reflective markers as the MoCap markers to provide tracking data of the body motions. The cameras record the data with a native frame rate of 240 Hz, which is equivalent to a latency of 4.2 ms. Besides, the native resolution of the cameras is 1280 by 1024 pixels. The retro-reflective markers can be tracked up to a depth of 16 m with a 3-D accuracy of ±0.2 mm. The cameras illuminate the markers with infrared LEDs, which have a wavelength of 850 nm and subsequently record the data with an 850 nm band-pass filter. This optical system has a focal length of 5.5 mm [Opt]. Any arbitrary arrangement for the position and orientation of the cameras enables the MoCap system to cover the capture volume as completely as possible. For this reason, sixteen Prime^{X}13 cameras are utilized in two planes with different heights. The OptiTrack system is solved by using its corresponding software, Motive 2.3.0. The applied steps for solving the OptiTrack system are similar steps to match multiple 2-D camera images to reconstruct 3-D information. The first step is processing the two-dimensional camera images by correcting the nonlinear distortion from the lens curvature and rectifying the image due to perspective distortion. Then, the second step is feature matching, where markers

are identified in the camera images. Finally, the last step is triangulation to reconstruct the three-dimensional information of the markers.

The calibration process of the MoCap system includes the calibration of a wand and the angle. That enables the system to gather information about extrinsic parameters, e.g., the global position and orientation, and intrinsic parameters, e.g., focus length. The wand calibration makes use of the retro-reflective markers with a specific size at a well-known distance from each other. Therefore, it is essential to label the markers and assign them to certain body parts. For the calibration, the wand has to be moved through the capture volume, and each camera must record a sufficient number of 2000 to 5000 samples. The calibration angle defines the ground plane and the orientation of the global coordinate system. It consists of three L-shaped markers to determine the z-axis and x-axis, with the y-axis being perpendicular [Cal]. Triangulation is used to reconstruct the 3-D position of a marker based on its center in the 3-D camera images after correction and feature matching. The collected information during the calibration process of the MoCap system is applied for positioning the markers.
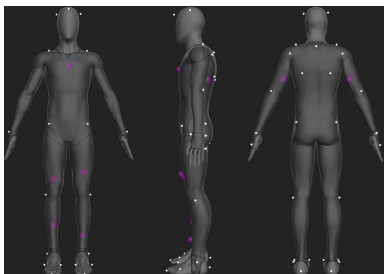
Figure 5.3: Markers setup in Motive 2.3.0. White dots show the attached markers, which are used to create data corresponding to body joints and are placed around them. The purple markers can be seen as additional markers for the segments between the joints, i.e., the bones. (Figure based on [2], ©IEEE.)

As discussed, it is crucial to assign the retro-reflective markers at the defined positions on a person's body. Figure 5.3 shows the markers arrangement for full body tracking. In the further step, the solver uses the previously gathered information about the marker positions to create the skeleton for full-body tracking. Therefore, the markers can be labeled and assigned to specific body

parts. It is worth mentioning that the person must take up a T-pose, which is the well-known pose by Motive's solver. Accordingly, a skeleton of 21 body joints is created as schematically shown in Figure 5.4.
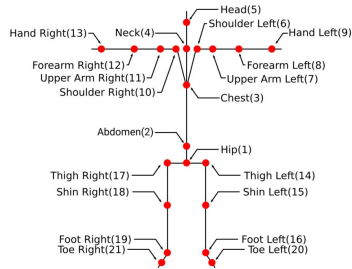
Figure 5.4: Utilized skeleton in the Motive environment for tracking human motions.

5.2 Measurement Setup for Extracting Velocity and RCS Information of a Human Body in Motion

A precise radar model of human motions can be developed based on the backscattering behavior of human body regions which is combined with their dynamic description. A dedicated measurement setup can be exploited to obtain the range, velocity, and RCS information of individual body parts of a human in motion. The collected radar raw data is analyzed by the presented EFE algorithm in Section 2.3.2 to extract the range and velocity information of a moving target. That enables the measurement technique to assign a verified RCS value and Doppler signature to different extremities of a human body. Based on this knowledge, human activities can be characterized to approach a realistic and precise human model in a simulation environment.

In this section, a measurement setup is proposed to extract the radar signature and recognize the human activity. This measurement technique is evolved based on the presented high-resolution monostatic RCS measurement setup, which is hybridized with MoCap data of human motion. A laptop and workstation control

the RCU and MoCap system, respectively, using the MATLAB interface. The Radar system and MoCap communicate via user datagram protocol (UDP) through a synchronization station. The synchronization station sends a trigger message to the MoCap cameras as soon as receiving an initialization message in the RCU system. Then, the MoCap cameras instantly begin the data collection. The Mocap and radar data are collected by assigning appropriate delays to guarantee that these processes happen simultaneously. The MoCap markers and cameras communicate with the MoCap synchronization station wirelessly. The Human body is considered as an electrically large dielectric body, i.e., it is an extended target with multiple scattering points.
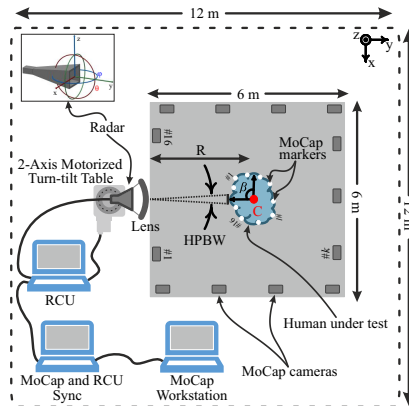
Figure 5.5: Block diagram of measurement setup to detect the scattering points with their corresponding range, velocity, and RCS information of a human in motion for radar model extraction. The rotation angles of the radar in azimuth (φ) and elevation (θ) directions as well as the radar coordinate system are shown in the inset. (Figure based on [2], ©IEEE.)

A block diagram of the proposed measurement setup is shown in Figure 5.5. The measurement is conducted in a motion lab environment with dimension of $12\,\mathrm{m} \times 12\,\mathrm{m} \times 4.5\,\mathrm{m}$ ($L \times W \times H$). This measurement technique is capable of collecting the MoCap data of human movement concurrently with the radar data collection from the human extremities based on high-resolution monostatic RCS measurement. A test person is dressed in a MoCap suit and placed in the range of R from the Radar system in the test setup. As explained in Section 3.9,

the main beam of the Radar system ($\varphi = 0°$ and $\theta = 0°$) is adjusted to the center of the human under test. It is assumed that this reference point corresponds to the half height of the human in the elevation direction and the middle of its shoulder width in the azimuth direction. The explained measurement setup has the capability to extract the range, velocity, and verified RCS values from each region of the human body from the collected unprocessed raw data.

It is worth emphasizing that the retro-reflective markers of the MoCap system are attached to the volunteer person's body on specified positions as discussed in Section 5.1.3. It allows measuring the motion from each extremity of the human under test by the MoCap system and, in parallel, scanning the same region with the Radar system. During human motion measurement, the human body is subdivided into three main regions, i.e., torso-head, hand, and leg, which are illustrated in the inset of Figure 5.6. Furthermore, the left and right sides of each region are scanned separately.
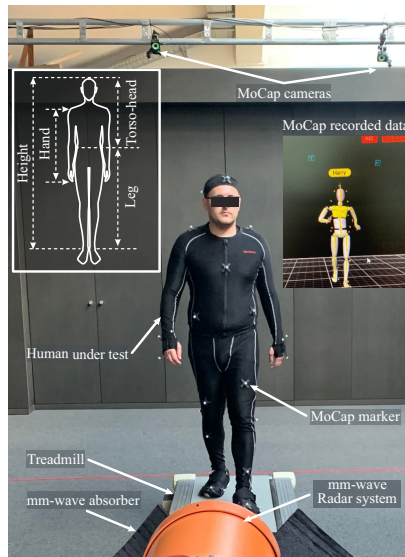
Figure 5.6: Setup for extracting range, velocity, and RCS information of different body parts of a human in motion. The defined corresponding body parts (torso-head, hand, and leg) for measurement of each body region are shown in the inset. (Figure based on [2], ©IEEE.)

Figure 5.6 demonstrates the measurement setup in detail, which is conducted in the motion Lab environment provided by HHVISION company. The test person is positioned in the setup at the distance of 3.5 m from the Radar system, and then the radar starts to collect the range, velocity, and RCS information of the body parts in motion. Moreover, a treadmill with an adjustable speed is employed in the measurement setup to extract the radar signatures of a human in activities like walking or jogging situations. The treadmill is covered with thin and flexible radar absorbers to avoid the influence of undesired reflections. Section 4.2 explains the influence of the surface material on the back-scattering behavior of radar targets. The MoCap suit utilized in this work is very thin and tight; therefore, it does not almost affect the RCS of the body regions.

The following section discusses the performed experiments on a human in walking and jogging situations. The collected radar raw data is examined based on the EFE algorithm to extract the scattering points, rang-velocity information, and verified RCS values of each body region. It is worth noting that the motion data of human movements are gathered simultaneously.

5.3 Extracted Radar Signatures of Human in Motion

For describing the measurement results of a human in motion, the necessary signal processing steps are shown in Figure 5.7. This signal processing chain is used to introduce the scattering points of the human in motion, i.e., a jogging and walking person. As explained in Sections 3.9 and 3.8, a calibration process consisting of two steps is essential to get correct RCS values. Figure 5.7 illustrates the mentioned calibration steps, i.e., clutter level and RCS calibration factor. In the first step, the Radar system scans the test environment in the absence of any test object to store IF data from the measurement environment $[S_{\text{if},emp}(n,q)]$. In the next steps, a standard TCR, with an analytical RCS value of $0\,\text{dBsm}$, is placed in the measurement setup to collect its radar data $[S_{\text{if},cr}(n,q)]$ and later postprocessing. As demonstrated in Figure 5.7, it is the calibration step for normalizing the measured RCS values for the object under test. In the signal processing steps, an additional gating is applied to the stored IF data in its spatial domain to attain only the reflections from the desired targets. The desired target can be either the human under test $[S_{\text{if},Mo}(n,q)]$ or the calibration
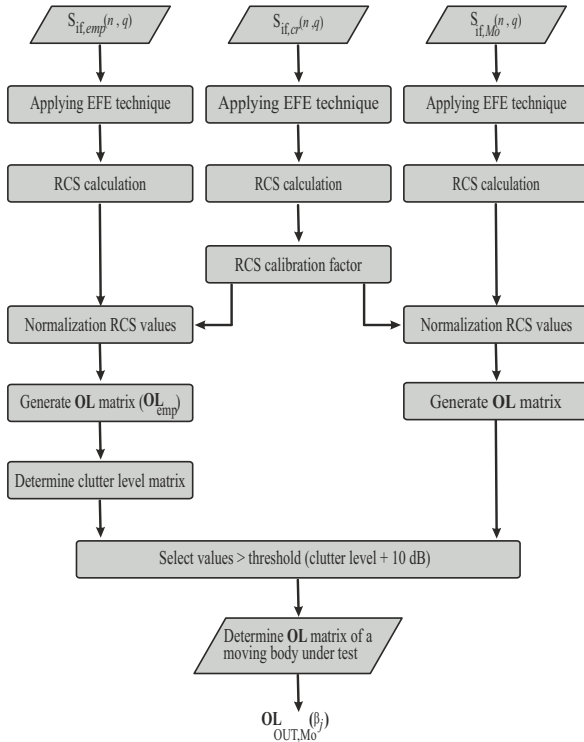
Figure 5.7: Signal processing chain for extracting the SPs of human in motion from the high-resolution measurement data and their corresponding radar signature, i.e., their RCS values, velocity, and micro-Doppler information. (Figure based on [2], ©IEEE.)

target $[S_{\text{if},cr}(n,q)]$. This signal processing chain exploits the combination of the EFE technique and subsequent calibration process to estimate precisely the position of the SPs on the body exterior along with their associated RCS value and velocity. It should be mentioned that the stored IF data is still a function of the scanning parameters, i.e., θ, φ, and β. However, the stored IF data is shown as a function of indexes of fast-time (n) and slow-time (q) for the sake of the simplicity.

For characterizing the test environment, the Radar system scans the environment in the area of $\pm 10°$ in azimuth (φ) and $-19°$ to $17°$ in elevation (θ) directions and also, in the absence of the human under test. In this experiment, the scanned area is defined in accordance with the dimension of the biggest test objects. This experiment is conducted with an angular resolution of $1°$ in both radar scanning directions to gather data from the empty room, $S_{\text{if},emp}(n,q)$, and clutter level calculations. The clutter level matrix $[\mathbf{CL}(\beta_j)]$ is generated by introducing the maximum measured RCS value in every scanned elevation angle.

Eventually, the collected raw data from the radar measurement for the test person with defined motions $[S_{\text{if},Mo}(n,q)]$ is investigated to introduce the object list of human motion in each radar viewing angle (β_j). $S_{\text{if},Mo}(n,q)$ includes the radar signatures of different body regions, which enables the signal processing chain in Figure 5.7 to present an object list of each body region of the human in motion ($\mathbf{OL}_{\text{OUT},Mo}$) with the following structure:

$$\mathbf{OL}_{\text{OUT},Mo}(\beta_j) =$$

$$\begin{bmatrix} x''_{1j} & y''_{1j} & z''_{1j} & \text{RCS}_{1j} & \varphi_{1j} & \theta_{1j} & \overline{sl}_{1j} & f_{D1j} & v_{1j} & t_{1j} \\ \vdots & \vdots & \vdots & \vdots & \vdots & \vdots & \vdots & \vdots & \vdots & \vdots \\ x''_{ij} & y''_{ij} & z''_{ij} & \text{RCS}_{ij} & \varphi_{ij} & \theta_{ij} & \overline{sl}_{ij} & f_{Dij} & v_{ij} & t_{ij} \\ \vdots & \vdots & \vdots & \vdots & \vdots & \vdots & \vdots & \vdots & \vdots & \vdots \\ x''_{Pj} & y''_{Pj} & z''_{Pj} & \text{RCS}_{Pj} & \varphi_{Pj} & \theta_{Pj} & \overline{sl}_{Pj} & f_{DPj} & v_{Pj} & t_{Pj} \end{bmatrix} \quad (5.2)$$

where x''_{ij}, y''_{ij}, z''_{ij} are the coordinates of the ith scattering point on the human extremities of the scanning region in radar viewing angle of β_j, RCS_{ij} is its

measured RCS value, f_{Dij}, and v_{ij} are its measured Doppler shift and velocity, t_{ij} shows the instant of human motion related to the ith scattering point, and P is the total number of extracted points from the human region under study.

The test person is measured in jogging and walking situations over the whole 360° azimuthal rotation angle with an angular resolution of 90°, which corresponds to four viewing sides of the person, i.e., front, right, left, and back view. Then, the scanning area of the Radar system is defined based on the physical dimensions of the human in motion to cover the body region under test as comprehensively as possible. Furthermore, every body region is scanned with step widths of 1° in azimuth as well as elevation directions ($\Delta\varphi = \Delta\theta = 1°$). The chirp number is assigned to 256 in the radar configuration .

As proof of concept, the extracted radar signatures from the measured data for body regions of a jogging person on the treadmill with a speed of 1.94 m/s are depicted in Figures 5.8, 5.9, and 5.10. The measured scattering points in Figures 5.8, 5.9, and 5.10 are along the leg, head-torso, and hand, respectively. The measured points of each body region are illustrated in different subfigures. The radar viewing angle in these experiments is the front side of the test person ($\beta=0°$).

Notwithstanding, the measurements for each body region are conducted with steps of 1° in azimuth and elevation directions, the examined radar signatures of a few elevation and azimuth scanning angles are shown in this chapter. The depicted radar signatures are the range-velocity plots of the region under test, and the measured points from each region are displayed in the inset of each subfigure. The exact measured point of each region is marked with red dot.

The range-velocity plots in Figures 5.8(a)-(f) are related to the different measurement points from the left leg of the person in the jogging situation. The represented information on the x-axis and y-axis of the plots correspond to the range and velocity information, respectively. The RCS values are given by the color code of the points. Figure 5.8(a) reveals that the extracted information from the radar measurement around the waist of the body, which moves slightly during the jogging. The extracted SPs are concentrated in the range of 3.5 m with a velocity close to 0 m/s. Considering the position of the measurement point ($\theta = 0°$) on the waist of the body, it complies with expectations. By evaluating range-velocity plots of more measurement points along the leg and increasing the distance from the torso, it can be realized that the measured points
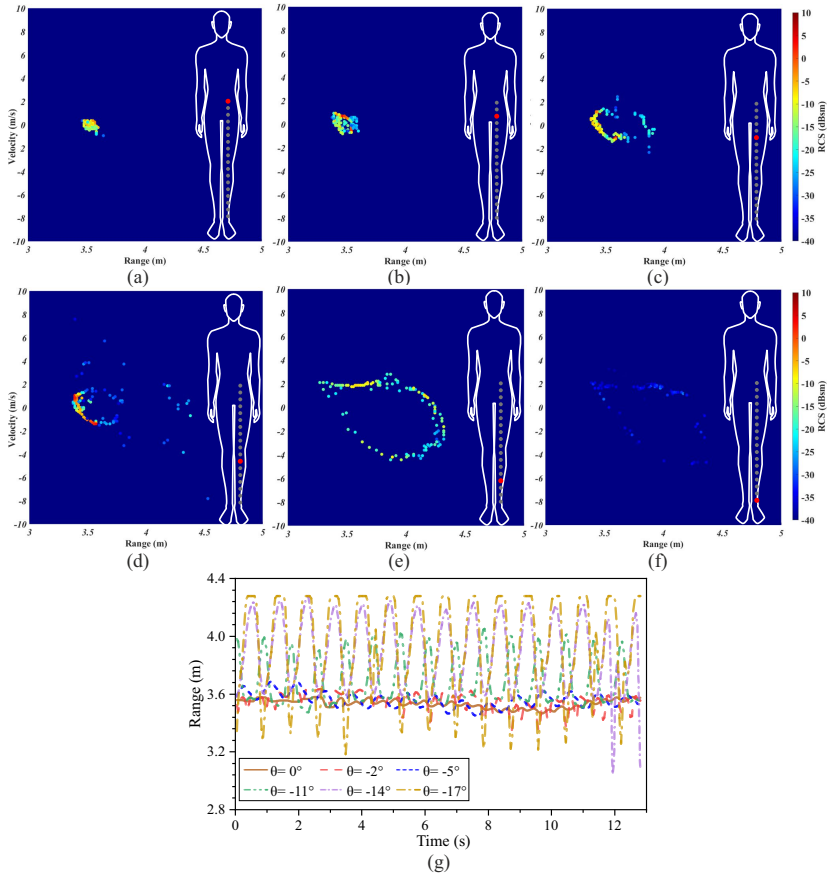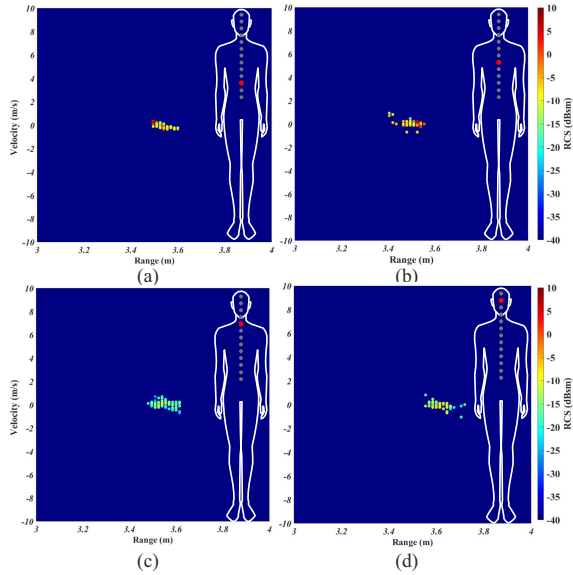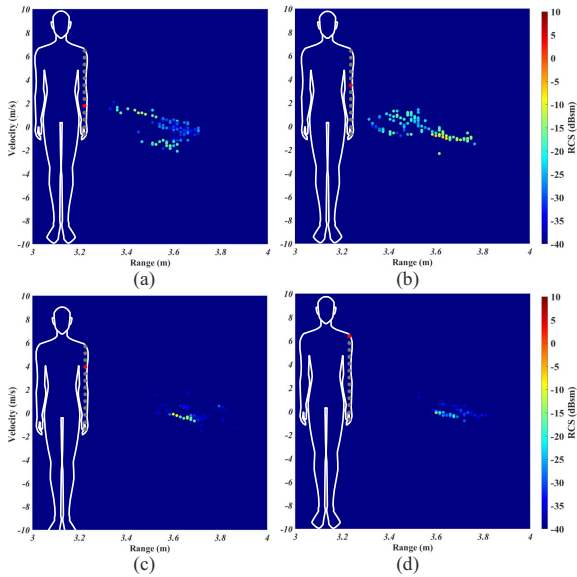
Figure 5.8: Extracted range, velocity, and RCS data of a jogging human with a set speed of 1.94 m/s. The measured scattering points are along the left leg ($\varphi = -1°$) with elevation angles: $\theta = 0°$ (a); $\theta = -2°$ (b); $\theta = -5°$ (c); $\theta = -11°$ (d); $\theta = -14°$ (e); $\theta = -17°$ (f); extracted range data corresponding to sub-figures (a)-(f) from the collected MoCap data (g). (Figure based on [2], ©IEEE.)

have a higher velocity and more significant displacement. This result is clearly observable in Figures 5.8(b)-(f) and is caused by the increasing movement range of the measured points in the mentioned direction. Since the leg moves from the back to the front and again back, a closed curve is recognizable in the plots, e.g., in Figure 5.8(e), which clearly shows an ellipsoidal curve. Furthermore, this induced a smaller and larger distance to the radar and subsequently shows a positive and negative velocity. The variations of the RCS values in these figures show that the measured RCS values depend on the position of the point from the body region and the radar viewing angle during the motion. Moreover, the collected MoCap data are analyzed to extract the range information corresponding to Figures 5.8(a)-(f) and compare with range information from the radar measurement. Figure 5.8(g) shows the extracted range data from MoCap data, which is in good agreement with the radar range data.

The extracted range-velocity information for the torso-head region of the human body under test is shown in Figures 5.9(a)-(d) at the azimuth angle of 0°. The test person is still jogging on the treadmill with the speed of 1.94 m/s. As illustrated in these figures, the dynamic behavior of the torso-head region is less than the leg and hand regions. Considering the RCS values of the detected SPs in plotted range-velocity information, it can be realized that the most robust backscattering behavior comes from the center part of the torso region. Another interpretable result is that the head region (Figure 5.9(d)) has the weakest RCS values, which is predictable.

Figures 5.10(a)-(d) show the investigated measurement result for the left hand-region of the human in motion. The extracted range-velocity plots show the ellipsoidal path in the different elevation angles. The extracted radar signatures in this region show that the velocity of the detected SPs is diminishing with changing the measurement points toward the shoulder, where they have a higher elevation angle.

In the next step, the time-varying RCS values from the human extremities are analyzed quantitatively. For this purpose, the measured RCS values of the jogging person are compared with the static ones in the same body regions. This inspection can be done by the plotted RCS values in Figure 5.11, which correspond to the left leg and torso region of the human under test. The radar scanning area for the left leg region, in this examination, is $\theta = -5°$ and $\varphi = -1°$. For the torso region, the information under study is related to the radar scanning area of $\theta = 6°$ and $\varphi = 0°$. It is observed that the calculated RCS

Figure 5.9: Extracted range, velocity, and RCS data of a jogging human with a set speed of 1.94 m/s. The measured scattering points are along the torso-head ($\varphi = 0°$) with elevation angles: $\theta = 3°$ (a); $\theta = 6°$ (b); $\theta = 9°$ (c); $\theta = 12°$ (d). (Figure based on [2], ©IEEE.)

values of the torso region are higher than the leg region in the static situation. Consequently, the torso has a more robust backscattering behavior than the leg region. Apart from this expected result, from comparing the RCS values of similar body regions with different human motions can be interpreted that the RCS values of human extremities in a motion situation change around the RCS values of the static situation. Figure 5.11 shows that the RCS values of the leg region in the jogging situation vary in the range of ±18 dBsm around the RCS values of the static situation. The RCS values of the torso region for the jogging person vary in the range of ±11 dBsm. Finally, this examination shows that the RCS variation of the torso region is less than the leg region when the person is jogging.

In addition, it is beneficial to analyze the velocity effect of human motion on the extracted radar signatures. Therefore, the test person is also measured in

Figure 5.10: Extracted range, velocity, and RCS data of a jogging human with a set speed of 1.94 m/s. The measured scattering points are along the left hand ($\varphi = -4.5°$) with elevation angles: $\theta = 2°$ (a); $\theta = 5°$ (b); $\theta = 7°$ (c); $\theta = 10°$ (d). (Figure based on [2], ©IEEE.)
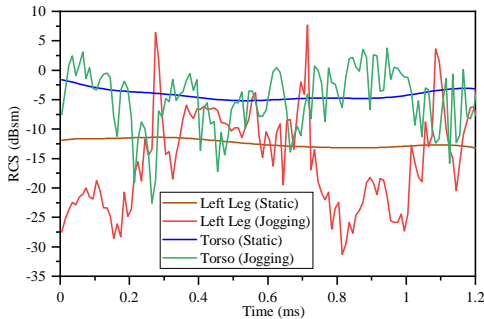
Figure 5.11: Corresponding RCS values of the left leg, in the radar scanning area of $\theta = -5°$ and $\varphi = -1°$, and torso, in the radar scanning area of $\theta = 6°$ and $\varphi = 0°$, of the human body in static and jogging situations. (Figure based on [2], ©IEEE.)

the walking situation (0.69 m/s), and its extracted range-velocity information is compared to the results of the jogging situation (1.94 m/s). The body region for this examination is the left leg. The range, velocity, and RCS of the jogging human in elevation angles of $\theta = 0°$, $\theta = -8°$, and $\theta = -14°$ are demonstrated in Figures 5.12(a)-(c). The analyzed measurement results for a walking person in the same body region and radar scanning angles are shown in Figures 5.12(d)-(f). The comparison of the measurement results shows that increasing the velocity of human motion expands the size of the ellipsoidal path.
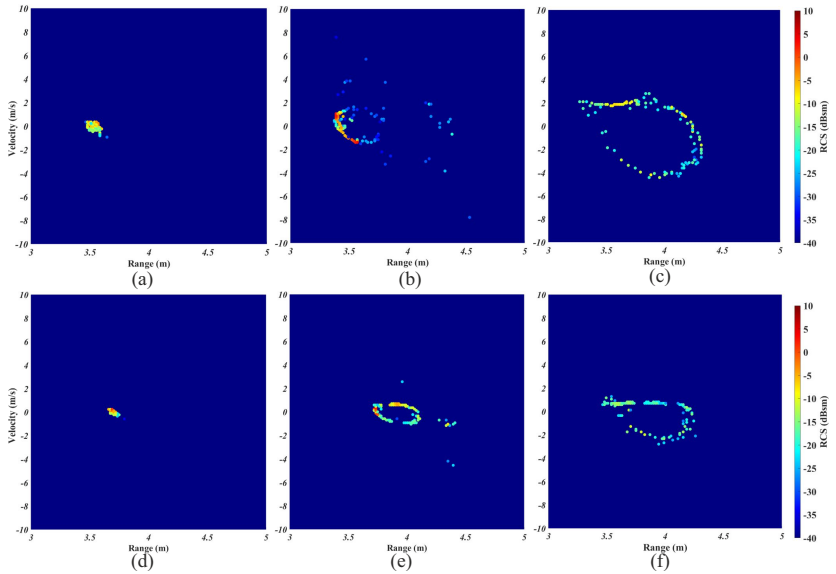
Figure 5.12: Extracted range, velocity, and RCS data along the left leg ($\varphi = -1°$) of a human jogging (1.94 m/s) and walking (0.69 m/s); (a) jogging ($\theta = 0°$); (b) jogging ($\theta = -8°$); (c) jogging ($\theta = -14°$); (d) walking ($\theta = 0°$); (e) walking ($\theta = -8°$); (f) walking ($\theta = -14°$). (Figure based on [2], ©IEEE.)

5.4 Extracted Radar Signatures of Motorcyclist's Extremities in Movement

One of the challenging radar targets in traffic scenarios is bike riders. Hence, modeling human activities during the riding is essential to develop an accurate and realistic backscattering representation of the bikers. Therefore, the proposed measurement technique in Section 5.2 is used for collecting the scattering points of the rider, consisting of the RCS values and range-Doppler signatures from its motion. Furthermore, this section investigates the influence of the motorbike suit and ride pillion on the motorcyclist's radar signatures and backscattering behavior. For this purpose, a volunteer person sits on a motorcycle, which is positioned in the high-resolution RCS measurement setup without maneuver, to imitate the motorcyclist's movements during the ride. These movements are random but similar to the motions of a rider in a real scenario.

The conducted experiments for extracting the radar signatures of a motorcyclist are shown in Figures 5.13. Firstly, the clutter level measurement, shown in Figure 5.13(a), is conducted to characterize the test environment in the absence of the motorcyclist and calculate the CL. Then, the test person, which is dressed with a MoCap cloth, sits on a motorcycle (BMW R 1200 GS), as displayed in Figure 5.13(b). The motorcyclist is located at the range of $R = 6.6\,\text{m}$ in the test setup so that its center is aligned with the main beam of the Radar system ($\varphi = 0°$ and $\theta = 0°$). The size of the motorcyclist together with the motorcycle is $2.2\,\text{m} \times 0.95\,\text{m} \times 1.88\,\text{m}$ ($L \times W \times H$). The measurements are performed in the motion Lab environment provided by the Cologne University of Applied Sciences. In the conducted experiments in this section, the chirp numbers and full ramp period of the radar are configured to 220 and 8 ms, respectively. This configuration provides enough time to sample the movement of the rider. The Radar system scans the object under test with the step width of $1°$ in both azimuth and elevation directions and the assigned scanning areas based on the size of the object under test to cover the complete region of interest.

To prevent any unexpected distortions in optical motion capture sequences of the MoCap markers, reflective surfaces on the motorbike, e.g., painted surfaces or glass, are covered with paper. It should be mentioned that the paper material does not influence the back-scattering behavior of the motorcycle.

Figure 5.13: (a) Setup for measuring the clutter level of the test environment. The Radar system scans the test environment in the absence of a rider. (b) Setup for monostatic high-resolution RCS measurement to extract the range, velocity, and RCS information of different body parts of a motorcyclist in motion. The defined corresponding body parts (torso-head, hand, and leg) for measuring each body region are shown in the inset.

The extracted radar signatures of motorcyclist motion from its exemplary regions, i.e., torso-head in back view and left hand in front view, in a riding situation is examined in Figures 5.14 and 5.15. In real traffic scenarios, the motorcycle rider is dressed in a motorcycle combi suit, which affects the reflected signals from the motorcyclist and, subsequently, the RCS values of its SPs. Analyzing the influence of the reflective material of the combi suit is the motivation to perform the same experiments when the rider wears a motorcycle jacket instead of only the MoCap cloth. Then, this influence can be evaluated by comparing the RCS values of the measured SPs from the same extremity during the measurements with MoCap cloth and motorcyclist jacket. In a further step, a correction factor can be estimated from the collected results to include the influence of the reflective materials on the measured RCS values. The approximated correction

factor is beneficial for correcting the RCS values of the measured SPs when the rider is dressed up only in MoCap cloth. Accordingly, the reconstructed radar models can be known as a more realistic and accurate model of a motorcyclist's movements. It is worth noting that the Radar system scans the body regions with an angular resolution of $\Delta\varphi = \Delta\theta = 1°$ in azimuth and elevation directions; however, only the extracted radar signatures of the motorcyclist in a few scanning angles are represented.

Figures 5.14 and 5.15 show the measured data from the volunteer motorcyclist along its torso-head and left-hand regions in the riding situation of the motorcycle from the back side and front side, respectively. From the range-velocity plots of the torso-head region in Figure 5.14(a)-(f), it can be determined that the points are concentrated around the range of 6.6 m in the radar azimuth scanning angle of $\varphi = 0°$. The measured SPs are spread around the range of 6.6 m with changing the scanning area toward the hand regions. As a result, the extracted points show a higher velocity and more significant range variation around 6.6 m. This observation can also be concluded from the range-velocity plots (Figure 5.15(a)-(d)) of the left-hand region. Additionally, the plotted radar signatures are examined for the reflectivity behavior of the same body extremities with changing the fabric of the motorcyclist. The dressed rider in a motorbike jacket (MJ) shows a stronger reflectivity in comparison to wearing MoCap cloth (M) which is a thin layer with a minimal influence on the backscattering behavior of the body. For quantitative analysis, the measured RCS values during the radar measurement time for each scanned area from the torso-head and left-hand regions are plotted in Figure 5.14(g) and Figure 5.15(e), respectively. These plots also confirm the higher reflectivity from motorcyclists in the presence of a motorbike jacket.

The ride pillion of a motorcycle also is one of the typical VRUs that can affect the motorcyclist's backscattering behavior. Therefore, it is of interest to examine the influence of a ride pillion on the motorcyclist's backscattering behavior. For this purpose, a second volunteer sat behind the rider in the high-resolution monostatic RCS measurement setup, as shown in Figure 5.16. Then, the Radar system scans their different body regions. The extracted range-velocity information of the test persons (MS) along the torso-head and left-hand regions are plotted in Figure 5.17(a)-(c) and Figure 5.18(a)-(c) in the exemplary radar scanning angles. The motorcyclist and its pillion are imitating a riding situation. The radar signatures of the motorcycle (M) with one rider are presented in
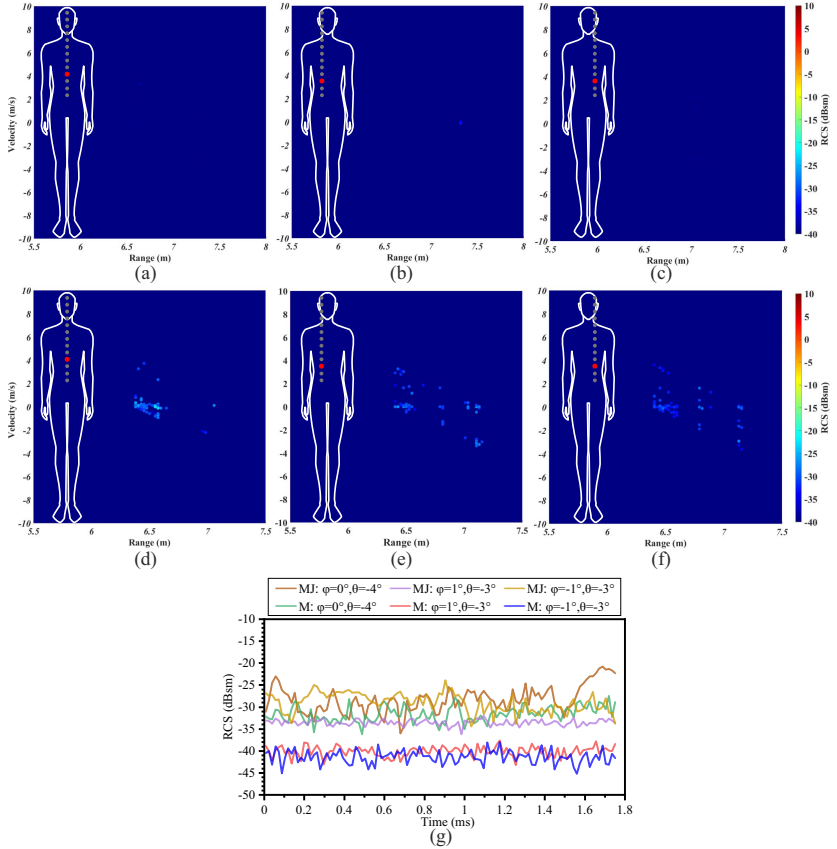
Figure 5.14: Extracted range, velocity, and RCS data of a motorcyclist along the torso from the back view in the moving situation. Collected SPs of Motorcyclist when dressed up in MoCap cloth (a) at $\varphi = 0°$ & $\theta = -4°$; (b) at $\varphi = 1°$ & $\theta = -3°$; (c) at $\varphi = -1°$ & $\theta = -3°$; and in motorbike jacket (d) at $\varphi = 0°$ & $\theta = -4°$; (e) at $\varphi = 1°$ & $\theta = -3°$; (f) at $\varphi = -1°$ & $\theta = -3°$; (g) extracted RCS values corresponding to sub-figures (a)-(f).
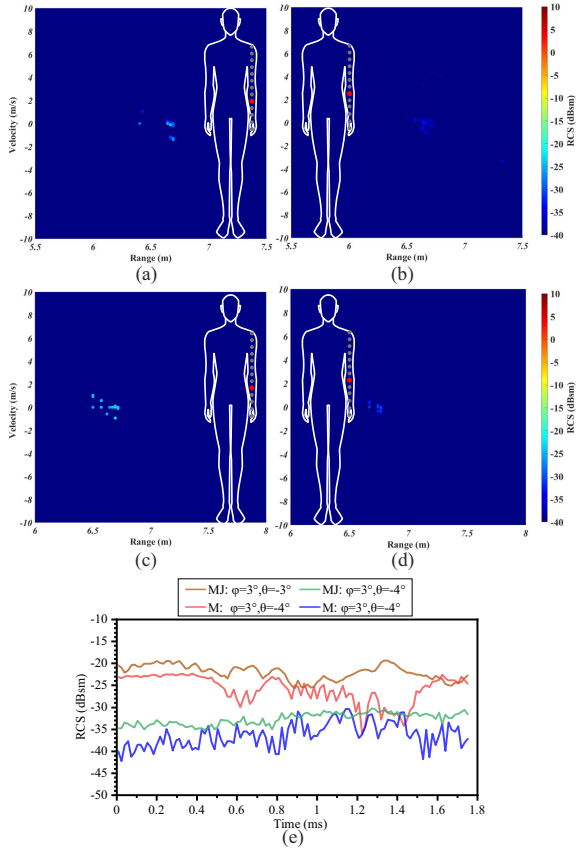
Figure 5.15: Extracted range, velocity, and RCS data of a motorcyclist along the left hand from the front view in the moving situation. Collected SPs of Motorcyclist when dressed up in MoCap cloth (a) at $\varphi = 3°$ & $\theta = -3°$; (b) at $\varphi = 3°$ & $\theta = -4°$; and in motorbike jacket (c) at $\varphi = 3°$ & $\theta = -3°$; (d) at $\varphi = 3°$ & $\theta = -4°$; (e) extracted RCS values corresponding to sub-figures (a)-(d).
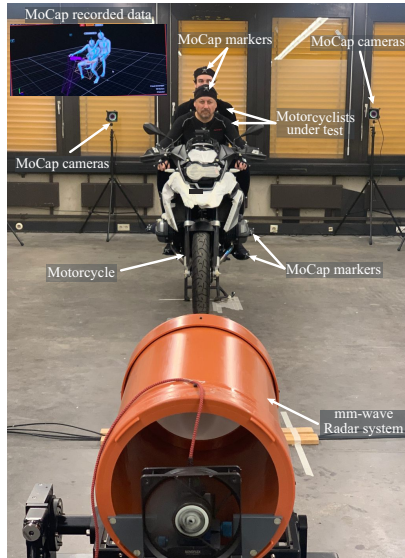
Figure 5.16: Setup for monostatic high-resolution RCS measurement to extract the range, velocity, and RCS information of different body parts of two motorcyclists in motion.

Figure 5.17(d)-(f) and Figure 5.18(d)-(f) at the same scanning area and body regions. It enables investigation of the pillion's influence on the motorcyclist's extracted radar signature. By comparing the plotted range-velocity information, it can be observed that the SPs have not only a larger variation of the range but also stronger backscattering behavior. The measured RCS values from two motorcyclists and a motorcyclist in the same scanned area are depicted in Figures 5.17(g) and 5.18(g) to compare their backscattering behavior quantitatively. It is observed that a motorcycle with a rider and a pillion has higher RCS values compared to the case in which only one rider exists. It was an expected result. Further, the difference between the averaged RCS values during the radar measurement time is calculated for the inspected body regions. The averaged RCS values are changing between $-18\,\text{dB}$ to $20\,\text{dB}$ for the torso region. It is in the range of $-4.1\,\text{dB}$ to $11\,\text{dB}$ for the left hand region. Eventually, a correction factor of $6\,\text{dB}$ and $7.3\,\text{dB}$ is estimated by taking the average of the calculated differences for the torso-head and hand-body regions, respectively. These

correction factors can be added to the extracted RCS values from the measurement with one rider to roughly estimate the pillion's influence in complex scenarios. The extracted radar signatures, especially the variations of the RCS values, have been examined for the influence of the reflective elements in the motorbike jacket and ride pillion. Subsequently, this data can be employed for preparing a highly realistic radar model of motorcyclists' movement in complex traffic scenarios in the wave propagation simulation environment and activity recognition of the radar targets.

As discussed, the knowledge of the backscattering behavior of human body regions and their movement information are utilized to develop a highly realistic radar model of a human in motion. The range-velocity radar signature of human motion is extracted based on the proposed signal processing chains and the required calibration measurements. As a result, an authentic radar model of a human in motion is developed to be later used in wave propagation software.
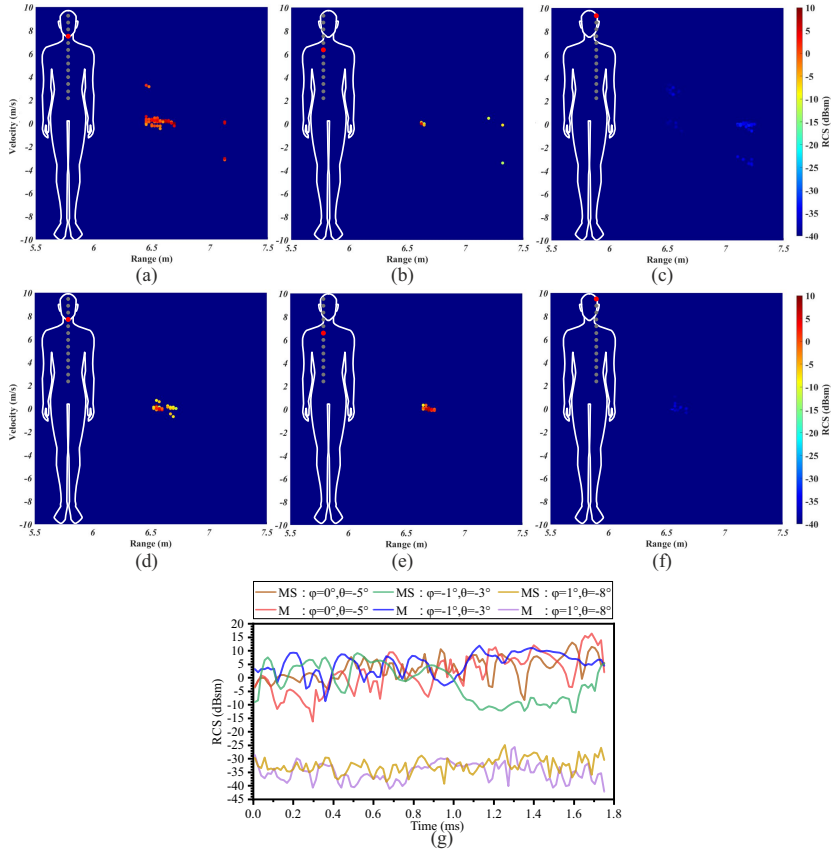
Figure 5.17: Extracted range, velocity, and RCS data of two motorcyclists (a) in $\varphi = 0°$ & $\theta = -5°$; (b) in $\varphi = -1°$ & $\theta = -3°$; (c) in $\varphi = 1°$ & $\theta = -8°$; and a motorcyclist (d) in $\varphi = 0°$ & $\theta = -5°$; (e) in $\varphi = -1°$ & $\theta = -3°$; (f) in $\varphi = 1°$ & $\theta = -8°$; (g) extracted RCS values corresponding to sub-figures (a)-(f). The measured scattering points are along the torso-head region, in which motorcyclists are in the moving situation and dressed up in MoCap cloth.

105
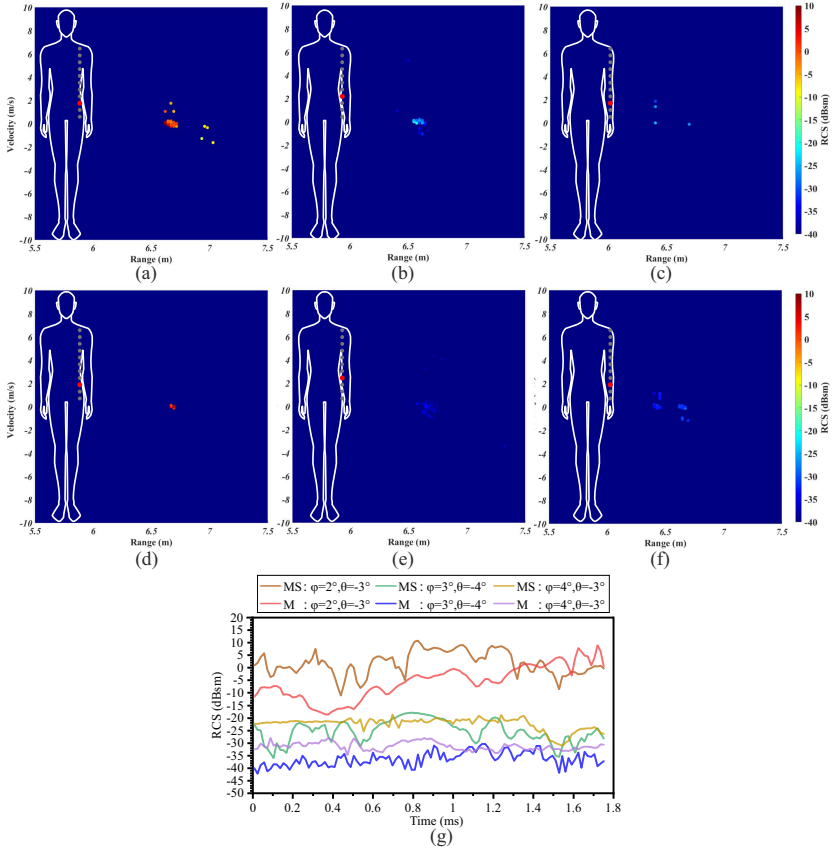
Figure 5.18: Extracted range, velocity, and RCS data of two motorcyclists (a) in $\varphi = 2° \& \theta = -3°$; (b) in $\varphi = 3° \& \theta = -4°$; (c) in $\varphi = 4° \& \theta = -3°$; and a motorcyclist (d) in $\varphi = 2° \& \theta = -3°$; (e) in $\varphi = 3° \& \theta = -4°$; (f) in $\varphi = 4° \& \theta = -3°$; (g) extracted RCS values corresponding to sub-figures (a)-(f). The measured scattering points are along the left hand region, in which motorcyclists are in the moving situation and dressed up in MoCap cloth.

6 Proposal for Extracting the Virtual Scattering Centers from Measured Radar Models

An accurate back-scattering model of the objects is an essential task in the correct wave propagation simulation and, subsequently, the validation and verification of an OTA-ViL system, as discussed in Chapter 1. Utilizing the real-world back-scattering behavior of VRUs is the solution to approach more realistic simulation results, which can be done based on high-resolution monostatic RCS measurements. The realistic radar model development based on the back-scattering behavior of VRUs has been thoroughly explained in Chapters 3, 4, and 5. Since the extracted radar model of VRUs has a plurality of SPs, reducing them to some significant scattering centers (SCs) can minimize the computational effort. In this case, each scattering center (SC) is introduced by its key parameters, i.e., back-scattering specification and virtual SCs.

Additionally, introducing the virtual SCs is another approach for using the data corresponding to each specific high-resolution RCS measurement more generally. For this purpose, a clustering method is exploited and multiple SPs of an object are clustered together. In the next step, the pattern corresponding to each cluster is extracted to introduce the clustered radar model of the VRUs. Furthermore, a more sophisticated VRU model and certain Doppler / micro-Doppler shifts can be assigned to these extracted clusters or SPs. This results in models with a highly accurate description of RCS value and Doppler signature of single parts of the body. These radar models can also be used for traffic scenario wave-propagation simulations with any arbitrary setting parameters, i.e., range and direction.

Furthermore, the intelligence of autonomous vehicles can be improved by collecting more environmental data, which is also mandated by the European new car assessment program (Euro NCAP) [LSM+19]. That necessitates a higher data collection by the radar sensors in the directions of the range, velocity, azi-

muth, and elevation angle of arrival (AoA) (4-D radar data). Therefore, recently many efforts have been accomplished to introduce high-resolution imaging radar sensors that can determine the environmental data as 4-D point clouds [SZ21, CWZ$^+$21, SWM$^+$18, CSCL21, NWC$^+$21, ZCH$^+$21, JXP$^+$22, SRDW22]. Thus, a higher level of data can be utilized for the target classification and recognition [CSCL21]. Concerning that, the signal processing of the radar raw data has a significant influence on the detections of the radar sensors; this high level data collection is also mandatory for approaching a reliable functionality of the 4-D imaging automotive radars and evaluating their necessary signal processing steps and detection algorithms [CSC20, PG18, ZHA$^+$21, WW19, WDW22, WMN$^+$20, CKCP18]. Moreover, clustered models for the point clouds of each radar target have been exploited in the simulation environments [Chi23]. Therefore, the introduced clustering method in this chapter can help to verify the developed models in the literature and their approximation for the required virtual SCs.

This chapter provides a brief theoretical overview of a technique to generate a significantly simplified radar model of the VRUs. This technique uses the greedy algorithm [CLR01] and the extracted SPs from the radar measurements to introduce SCs that may not physically exist but represent the virtual scattering centers with a defined scattering behavior.

6.1 Clustering Algorithm

Since the measured scattering properties of every VRU are a superposition of its SPs in each specific object direction, a 3-D radar model of VRUs is introduced in previous chapters from the measurement results. The modeling based on the scattering points provides a more effective way to describe the complex electromagnetic scattering phenomena of targets, but those can be arranged into scattering clusters. By clustering, the measured radar models can be further simplified to introduce the virtual SCs with their specific characteristics and later employ them in the wave propagation simulation tools and radar channel calculations. This simplification should be done with an algorithm that is able to obtain an optimal solution by making a sequence of choices. This heuristic strategy can be followed by a so-called greedy algorithm [SBW08]. Firstly, the greedy choice arranges the scattering points according to their intensity and

positions. The second choice is sorting the points in proportion to the defined dynamic range and vicinity to the strongest point in the cluster. In the next step, cluster formation will be started, but there is one more greedy choice. The algorithm needs to check the location of the strongest point in every cluster. Suppose the strongest point of every cluster is located closer to a defined limited distance to other clusters. In this case, the algorithm will pick the cluster with the stronger scattering point. Finally, the contribution of the scattering points into a particular direction is considered, and virtual scattering centers for every cluster and their radiation pattern are defined. The following subsection explains every step of the mentioned iterative greedy algorithm.

6.1.1 Proposed Greedy Algorithm

The dedicated steps are proposed based on the greedy algorithm to develop an algorithm and extract the virtual SCs from the measured SPs. These steps are explained in the following.

Search for strongest scattering point

The algorithm starts the cluster formation process by looking for the most robust scattering point. The strongest scattering point is the point with maximum intensity (RCS_{ij}). This value will be used to define the dynamic range or absolute threshold of the algorithm in every iteration until the last iteration. For that reason, this value is named (RCS_{max}). Then the algorithm searches for further scattering points in the surrounding of this point according to the defined cluster geometry. The dynamic range (DR) of the intensity related to the existing scattering points in every iteration can be calculated by

$$DR = 10 \log\left(\frac{\sum_{ij} RCS_{ij}}{RCS_{max}}\right). \tag{6.1}$$

Cluster geometry definition

The greedy choice properties amplify the algorithm to reach a globally optimal solution by locally optimal solutions (greedy choices). That means a greedy strategy reduces each given problem to a smaller one by one greedy choice after another [CLR01]. In accordance with the procedure referred to, the clustering algorithm in this work chooses the shape and location of the clusters adaptively. The cluster shape and size impact the number of introduced SCs. A small cluster size produces considerable numbers of clusters to reach a proper clustering model. On the contrary, a large size of clusters summarizes a large number of scattering points which decreases the influence of some strong enough scattering points in the extracted model. The geometrical structure of the clusters affects the extracted cluster numbers beside their sizes. If the cluster shape does not follow the geometry of the object, then a huge number of clusters is needed to introduce the simplified clustering model. Consequently, the defined shape and size of the clusters can produce a different number of clusters. Therefore the greedy choice in this step should be determined in a manner that can simplify the problem to subproblems and finally yields a globally optimal solution.

The first step of the cluster definition is collecting the geometrical information about the object under study and its top-view geometry. Assume that the size of the object under analysis is $L_{obj} \times W_{obj} \times H_{obj}$. Since the top view of the analyzed objects, in this work, is a rectangle with rounded edges, two different cluster shapes are considered, i.e., upright rectangles with size $l_{up} \times w_{up} \times h_{up}$ and across placed rectangles with the size of $l_{ac} \times w_{ac} \times h_{ac}$. The size of different cluster types is intended to cover every dimension of the object to allow a reasonable number of clusters along the other sides of the object. The geometrical input parameters for defining the size of a cluster, which modify the cluster search, are calculated by

$$
\begin{aligned}
r_{up} &= \frac{w_{up}}{l_{up}} < 1 \\
rd_{up} &= \frac{h_{up}}{w_{up}} > 1 \\
l_{up,max} &< W_{obj} < 2l_{up,min} \\
\delta h_{up} &> \text{R} \tan(\psi_{3dB})
\end{aligned}
\tag{6.2}
$$

$$r_{ac} = \frac{w_{ac}}{l_{ac}} = \frac{L_{obj}}{W_{obj}} > 1$$
$$rd_{ac} = \frac{h_{ac}}{w_{ac}} > 1$$
$$\frac{1}{2}H_{obj} < h_{ac} < H_{obj}$$
$$\frac{1}{3}L_{obj} < l_{ac} < L_{obj} \tag{6.3}$$
$$\delta h_{ac} > \text{R} \tan(\psi_{3dB})$$

where ψ_{3dB} is the half-power beam width of the utilized radar for scanning the objects, r_{up}, rd_{up}, r_{ac} and rd_{ac} are the aspect ratios of the upright rectangles and across placed rectangles, respectively. From Equation 6.3, it can be understood that the aspect ratio of the rectangles across is defined as the same as the aspect ratio of the object.

The variation margins for the geometrical sizes of the defined clusters can be derived from Equations 6.2- 6.3. Subsequently, modifying the cluster sizes inside the achieved boundaries can lead to clusters with a maximum density of scattering points. The last step of the cluster formation is moving each cluster, with its specific shape and size, along $x - y$, $x - z$, and $y - z$ planes with δx, δy, and δz. This movement allows for obtaining an optimum location for the scattering points, which fit in a cluster shape. As an example, Figure 6.1 shows this process for an upright cluster defined on the test person's right side (A). Furthermore, δx, δy, and δz are defined according to the object size and radar range resolution.
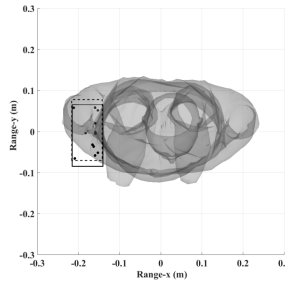
Figure 6.1: Movement process of the defined cluster from the original position (dashed line) to find the optimum fitting place (solid line).

111

Cluster birth

The subsequent step of the algorithm, after the determination of a cluster, is allocating a virtual SC with its location ($\vec{SC}$) and monostatic scattering characteristics (CC). Suppose M_k scattering points are contributed to the formation of the kth cluster in the iteration k^{th} of the algorithm. The center of the kth cluster can be introduced by

$$\vec{SC}_k = \frac{\sum_{i=1}^{M_k} \vec{SP}_i \cdot \text{RCS}_i}{\sum_{i=1}^{M_k} \text{RCS}_i}. \tag{6.4}$$

where $\vec{SP}_i$ is the position of ith SP between M_k contributed SPs in k^{th} cluster and RCS_i is its corresponding RCS value. In Equation 6.4, the center of each SC is calculated by weighting the position of SPs with the intensity of the participated points in the cluster generation. The summation of all complex contributions of M_k scattering points inside the kth cluster presents the back-scattering characteristic of each cluster [$CC_k(\phi, \theta)$],

$$CC_k(\phi, \theta) = \sum_{i=1}^{M_k} \text{RCS}_i \, e^{j(\phi_i + \theta_i)}. \tag{6.5}$$

where ϕ_i and θ_i are the angle of arrival (AoA) information for the ith scattering point in the azimuth and elevation directions, respectively.

Start over the next iteration

Due to the iterative nature of the proposed algorithm, searching for more solutions after the first cluster generation is indispensable. For this reason, after each cluster formation and assigning its virtual SC with its specification, the algorithm omits all scattering points that participated in the previous cluster generation for the next cluster birth. The cluster birth step is continued until

the contribution of the remaining scattering points is below DR (Equation 6.1) regarding the strongest scattering point (RCS_{max}).

In the last step of each iteration, the algorithm investigates the distance between the extracted virtual SCs. Finally, the algorithm introduces the cluster with the maximum density of scattering points per cluster area as an extracted cluster. In the next section, the proposed algorithm is applied to the measured radar model of the test person (A) and dummy in Chapter 4 to extract their virtual SCs.

6.2   Clustering Collected Scattering Points

This section takes advantage of the proposed algorithm for clustering the measured SPs of VRUs and expresses the scattering influence of all points of one cluster in a specific direction. Furthermore, the algorithm weights every scattering point with its RCS value which helps to introduce the virtual SCs based on their location and RCS specifications. In the last part of this section, the procedures of the proposed algorithm are also applied to the collected SPs from the RCS simulation to demonstrate that the proposed algorithm is applicable to the collected SPs either by measurement or simulation.

6.2.1 Extracting the virtual scattering centers from the measured radar model of VRUs

The 3-D radar model of the VRUs is developed based on the high-resolution RCS measurement from the superimposing of the extracted scattering points in different azimuthal radar viewing angles (β_j) with the step width of $\Delta\beta$ in previous chapters. It is worth mentioning that the VRUs are scanned at each viewing angle with the resolution of $1°$ in azimuth (φ) and elevation (θ) directions. The extracted radar models of the test person (A) and dummy human, shown in Figures 6.2(a) and 6.3(a), are used as an input for the proposed clustering algorithm to introduce their virtual SCs. The 3-D radar model of the person (A) and dummy are prepared by scanning them with angular resolution $\Delta\beta = 30°$ and $\Delta\beta = 10°$ in azimuthal aspect direction, respectively. The radar viewing angle in the elevation direction for the mentioned measurements is a perpendicular line to the longitudinal central axis passing through the center

of the object under test. The calculated DR for the objects under analysis is $-30\,\mathrm{dB}$. It should be noted that a finer step width of azimuthal rotation angle ($\Delta\beta$) results in a higher number of extracted clusters and as well the clusters with denser SPs.
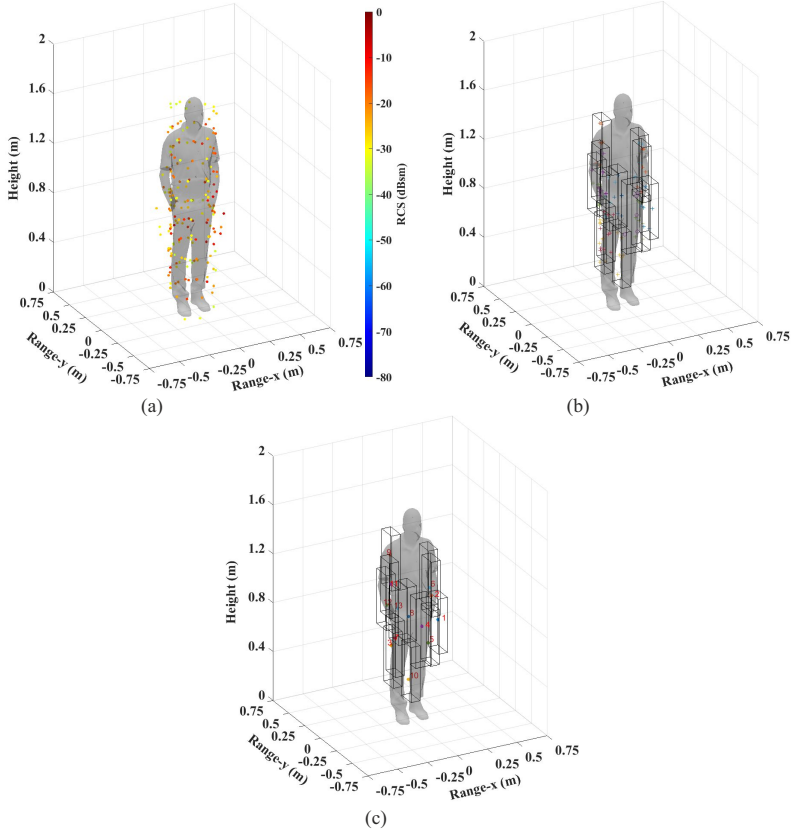
Figure 6.2: (a) The test person (A) with all SPs derived by high-resolution RCS measurement. (b) Clustering the mapped SPs on the body of the person. (c) The test person (A) with extracted SCs of every cluster.

Considering that the largest dimension of the objects under study, i.e., human bodies, is their height, therefore, the rd_{up} and rd_{ac} in the cluster geometry

definition step are defined to assign two or three clusters on their heights. Moreover, δh_{up} and δh_{ac} are established so that the clusters cover at least the extracted scattering points from two consecutive elevation angles. Subsequently, the δx, δy, and δz are defined according to the physical size of the object and radar range resolution, with the following values:

$$\delta x_{up} = 0.011(m), \quad \delta x_{up,step} = 0.03(m)$$
$$\delta y_{up} = 0.03(m), \quad \delta y_{up,step} = 0.03(m) \quad\quad (6.6)$$
$$\delta z_{up} = 0.16(m), \quad \delta z_{up,step} = 0.16(m)$$

$$\delta x_{ac} = 0.03(m), \quad \delta x_{ac,step} = 0.03(m)$$
$$\delta y_{ac} = 0.011(m), \quad \delta y_{ac,step} = 0.03(m) \quad\quad (6.7)$$
$$\delta z_{ac} = 0.16(m), \quad \delta z_{ac,step} = 0.16(m).$$
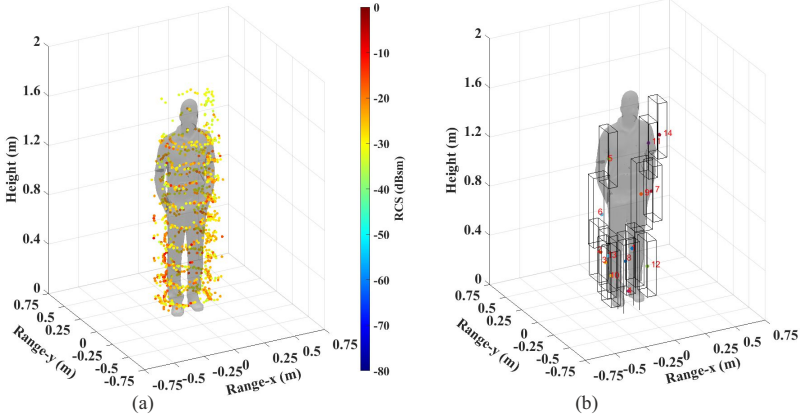
Figure 6.3: (a) The dummy human with the SPs derived by high-resolution RCS measurement. (b) The dummy human with extracted SCs of every cluster.

Each SP in Figures 6.2(a) and 6.3(a) is active for a particular direction with a specific amplitude and phase. Following the explained steps of the algorithm in section 6.1.1, each cluster is generated for the test person and shown in Figure 6.2(b), including the SPs inside each cluster. Finally, the clustered model

115

for the test person (A) and dummy human and their corresponding virtual SCs are depicted in Figures 6.2(c) and 6.3(b). In Figure 6.2(c), the test person (A) is shown with 10 clusters, and Figure 6.3(b) shows 14 virtual SCs of the dummy human. Since the angular resolved RCS measurement for the dummy human is done with a higher resolution than the measurement of the test person (A), the extracted model for the dummy human has more SCs in comparison with the test person. That shows the number of the virtual SCs is not only influenced by the density of the measured SPs but also changes according to the size of the object under test. However, a higher number of virtual SCs causes a more precise radar model for utilizing in simulation environments. The numbers of virtual SCs in every model are ordered according to the reflection of the strongest SP inside the cluster and illustrate the cluster formation order. The algorithm searches for the clusters without foreknowledge about the object structure and only determines them one after the other. This leads to the position of the extracted scattering centers not being symmetric.

The specific characteristics of virtual SCs are their locations and backscattering behavior in the local coordinate system. Table 6.1 summarizes the center location and RCS specifications of the first four clusters for the test person (A). This information is given in Table 6.2 for the human dummy from its measured 3-D radar model.

Table 6.1: Specifications of the extracted virtual SCs based on high-resolution RCS measurement of the test person (A).

Cluster #	X	Y	Z	RCS Specifications
				RCS variation range (dBsm)
1	0.17	-0.19	0.82	-25.5 ... -6.3
2	0.11	-0.14	1.03	-25.0 ... -7.8
3	-0.09	0.12	0.6	-31.2 ... -8.7
4	0.03	-0.19	0.91	-30.5 ... -10.9

As a proof of concept, this chapter utilizes the radar models extracted from the collected radar data in different radar scanning angles, various azimuthal radar viewing angles, and the elevation radar viewing angle corresponding to the normal incidence on the human body, to introduce the virtual SCs of the measured test person and dummy human. In a further step and for a more detailed backscattering model, it is also possible to conduct a high-resolution

Table 6.2: Specifications of the extracted virtual SCs based on high-resolution RCS measurement of the dummy human.

Cluster #	X	Y	Z	RCS Specifications RCS variation range (dBsm)
1	-0.01	-0.01	0.48	-25.8 ... -7.5
2	-0.19	0.07	0.42	-35 ... -9.8
3	-0.13	0.09	0.32	-33.2 ... -10.4
4	-0.04	-0.12	0.13	-34.8 ... -12.7

RCS measurement with different viewing angles of the radar in the elevation direction of the human body under test. The collected radar data contains information corresponding to the different radar scanning angles in the azimuth and elevation directions, as well as different rotation angles of the body under test in the azimuth and elevation directions, i.e., rotating around the *z*-axis and *y*-axis in Figure.3.7, respectively. However, it can be considered as further work. One challenge for this level of high-resolution measurement is the total time required. For example, the full measurement time can exceed several days in the case of a human body. For this purpose, the idea of using a dummy human object, discussed in Chapter4, can be applied. Furthermore, the dummy human must be hovered in the anechoic chamber and in front of the radar so that it can be rotated around its azimuth and elevation directions. Besides, it should also be considered that the radar measurements are not supposed to reconstruct the whole details of the object but should give an accurate model with minimum data size. Thus, more detailed information can be collected using RCS simulations with finer angular resolution.

6.2.2 Extracting the virtual SCs of VRUs based on the SPs from the simulation

The back-scattering behavior of VRUs can be analyzed in the simulation environment. For this purpose, a highly resolved CAD model of the VRUs is necessary, although this leads to a very high computational simulation effort. Then, this complex CAD model has to be employed in a ray-tracing tool to collect the scattering points of the VRU from a monostatic RCS simulation. The uti-

lized ray-tracing software in this work is IHE 3 D-ray-tracing tool [FMKW06]. Feasibility analysis of this concept is conducted by collecting the simulation result for a typical car model, i.e., Ford Focus, as its complex CAD model is available in the software environment.

Figure 6.4 illustrates a monostatic RCS simulation structure in the IHE 3 D-ray-tracing environment to derive the SPs of the complex car model. The car model is positioned in the center of a circle with a radius of 50 m to satisfy the plane wave condition. The SPs of the car, which are collected from the monostatic RCS simulation along the circle with 1° angular resolution for its different viewing angles, are demonstrated in Figure 6.5(a). The SPs are mapped with blue dots on the outline of the car. Each SP is recognizable by its specific amplitude and phase.
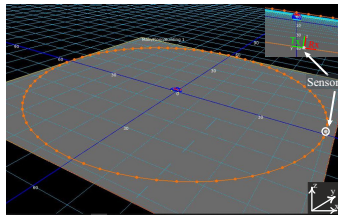
Figure 6.4: Monostatic RCS simulation structure for a complex CAD model in the software environment.(Figure based on [5], ©IEEE).

The proposed clustering algorithm is utilized to simplify the complex CAD model and arrange its SPs to virtual SCs. Figure 6.5(b) shows the generated clusters for the Ford Focus model, including the SPs of each cluster. The assigned DR for the complex model under study is set to −40 dB.

The RCS specification of each cluster can be calculated from the AoA and the attenuation of each SP from the simulation results. The AoA includes the radiation intensity information in azimuth direction $U_\phi(\theta, \phi)$ and in elevation direction $U_\theta(\theta, \phi)$. The RCS specification of each cluster can be calculated by
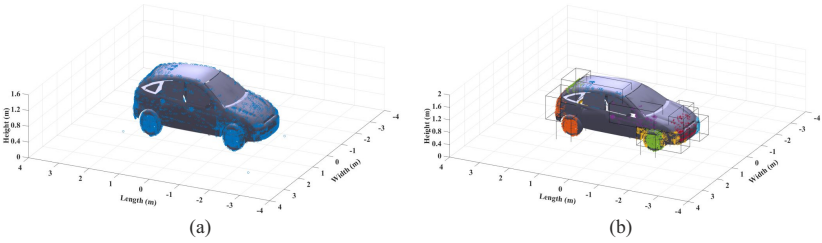
Figure 6.5: (a) Car with SPs derived by monostatic RCS simulation based on ray-tracing tool. (b) Car with clustered SPs. (Figure based on [5], ©IEEE).

$$U_C = \frac{4\pi \times U(\theta, \phi)\big|_{max}}{\int_0^{2\pi} \int_0^{\pi} \left|\vec{U}(\theta, \phi)\right| d\theta d\phi} \tag{6.8}$$

$$\vec{U}(\theta, \phi) = U_\theta(\theta, \phi)\vec{a}_\theta + U_\phi(\theta, \phi)\vec{a}_\phi.$$

The extracted virtual SCs of the analyzed car model with their RCS specifications are shown in Figure 6.6.
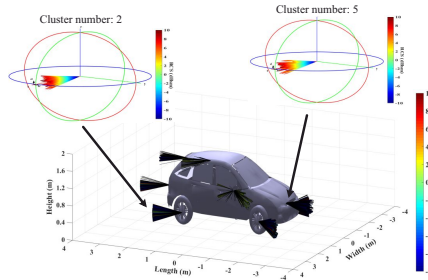
Figure 6.6: Back-scattering model for the Ford Focus with its extracted SCs and their RCS specifications. (Figure based on [5], ©IEEE).

The extracted RCS specifications of the generated scattering clusters are shown in Figure 6.6, and each cluster is positioned in its corresponding SC. Finally,

Table 6.3: Pattern information of the extracted SCs for the car model from the simulation results. (Table based on [5])

Cluster #	X	Y	Z	RCS Specifications
				RCS variation range (dBsm)
1	1.34	0.8	0.38	-25.6 ... 32
2	-1.4	0.8	0.4	-33.8 ... 32
3	1.9	0.75	0.4	-33 ... 31.9
4	-1.46	-0.72	0.37	-25.8 ... 30.8

Table 6.3 lists the first four SCs, which are derived from the simulation results, with their specific centers and RCS specifications.

It can be concluded that the proposed clustering algorithm can summarize the extracted back-scattering behavior of the VRUs by defining their virtual SCs. The input of the algorithm is the gathered SPs either by radar measurements or full-wave simulation results. Finally, the proposed algorithm generates the clusters with their associated positions and scattering patterns, which introduces the simplified radar model of the VRUs. These summarized scattering characteristics can be employed in wave propagation simulations to approach more realistic traffic scenario simulations and additionally speed them up.

7 Conclusions

The research conducted in this work focuses on the determination of the spatially distributed scattering centers of different VRUs based on a high-resolution RCS measurement setup. The main motivation for this work is to prepare realistic target models in wave propagation software which paves the road to realistic simulation results and, consequently, decreases the computational time.

Reliably modeling in the virtual environment is achievable by preparing accurate and realistic target models. In this work, these types of models have been developed based on pre-measured high-resolution angular-radial resolved monostatic RCS results. The scattering points of the object under test and their RCS values were determined by following the dedicated signal processing steps on the collected data during radar measurements.

A high-resolution measurement setup has been constructed, which is based on a mm-wave radar sensor with 5 GHz bandwidth and a center frequency of 78.5 GHz along with a high focusing lens with a half-power beam width of 1.3°. The large bandwidth of the Radar system allows for a high radial resolution of the measured area. Furthermore, the measurement system used mechanical scanning instead of electronic scanning to suppress side lobe interference from other directions and enable highly focused angular scanning capability in azimuth and elevation directions. That enables high-resolution radar measurements in radial, velocity, and angular domains, i.e., the azimuthal rotation angle of VRU and angular scanning area of the Radar system in both azimuth and elevation angles. Therefore, the Radar system enables the collection of unprocessed raw data in 5-D domain. The test environment was characterized by various calibration steps, which consist of clutter level determination and normalization of the measured RCS data. With this measurement setup, a variety of real-world road users and the different-sized VRUs have been measured with a scanning resolution of the Radar system of 1° at different rotation angles of the VRUs. The pedestrians and bikers are the VRUs with the most agile behavior in traffic

scenarios. Therefore, their backscattering behavior was analyzed and modeled in the simulation environment. The measured traffic objects were as follows:

– Human body: in the first step, some test persons with different sizes were scanned to model the backscattering behavior of a static human,

– Dummy human: measuring a dummy human in the corresponding size of one of the measured persons,

– A bicyclist: as one of the nimble road users,

– A motorcyclist: riding different types of motorcycles (classic, sport, and cross),

– A typical car (BMW X1) in the traffic scenarios.

It has been demonstrated that the projected scattering points of the measured VRUs are localized along their outline in each viewing angle of the VRU under test. Their approximate outline, orientation, and actual sizes have been predicted from the measurement results. Furthermore, the radar image of the VRUs has been reconstructed from the collected radar data corresponding to multiple azimuthal rotation angles. The investigation of the extracted radar images of the test persons showed that the relevant scattering points can be clearly detected over the body surface. Therefore, the extracted scattering points were utilized as input for an appropriative algorithm to derive the test persons' physical sizes. It has been shown that their measured physical sizes match very well with the actual physical sizes. The extracted radar models for the dummy and the corresponding test person were investigated, which showed very comparable values in size, distribution of the scattering points, and their RCS values. It enables the development of radar models with even higher resolved RCS data and the mapping of specific RCS values to relevant body parts.

Then, the extracted radar models of different types of exemplary VRUs, i.e., a motorcyclist who rides various types of motorcycles, were analyzed to approximate the necessary number of high-resolution RCS measurements in each group of potential VRUs. The observed backscattering behavior from this comparative study showed that a rider of different types of motorcycles has a roughly similar radar model and the RCS values of the extracted SPs are comparable. Furthermore, the typical RCS patterns of the motorcyclist were approximated from its high-resolution extracted radar models by utilizing a dedicated algo-

rithm. It has been deduced that the motorcycle type does not significantly affect the overall reflectivity behavior of a motorcyclist. It has only influenced the RCS levels from different viewing angles. Thereby, it is sufficient to develop a general realistic radar model for each group of VRUs. In the case of humans, a general model must be developed based on different body sizes.

As a matter of fact, human targets are not stationary, particularly in road scenarios. Therefore, the actual RCS values of the various extremities of a human in motion differ considerably from the extracted values for the respective area of a static human. It is particularly important to recognize and classify the different parts of the body. Accordingly, the high-resolution RCS measurement setup has been combined with the MoCap technique to introduce a high-resolution angular resolved RCS and Doppler measurement technique. This setup is competent for collecting the radar data of a human in motion and simultaneously capturing human movement by several cameras from different viewing angles. That facilitates extracting a highly realistic model of a human body in motion, which assigns micro-Doppler values with verified RCS values to the various extremities of a human body. Therefore, part of the focus in this work was set to collect radar information of the body in motion which, in the next step, was combined with the MoCap model. The range, velocity, and RCS values of distinctive body regions were extracted from the measured raw data by utilizing the validated EFE technique. The procedure was enhanced to measure the movement of body parts of a human in different situations like walking, jogging, and biking (bicycle and motorcycle). The high directive antenna of the Radar system was rotated in 1° steps in both azimuth and elevation directions to scan the various body regions, i.e., torso-head, hands, and legs, of a human in motion and covering the entire body region of interest. In the next step, several measurements were conducted in selected body regions with different situations to extract and investigate their range, velocity, and RCS plots. Finally, the extracted radar signatures were examined, and it was observed that:

- The measured points were clearly distinguished by range and velocity depending on the positions on the body's surface,

- The RCS values of the body parts do not only depend on their position along the body but also on their viewing angle by the radar during the movement.

It is the first time that a comprehensive radar model has been developed, which includes both RCS and the velocity of body parts. This data was utilized to create realistic target models with assigned micro-Doppler and verified RCS values to the different extremities of a human body in wave propagation software.

In order to present a reliable application of the derived radar models, a clustering algorithm was evolved to introduce virtual scattering centers from the extracted scattering points of the performed measurements. The algorithm generated the clusters, the associated virtual scattering centers, and their backscattering specifications. The generated data were used to construct the simplified models of VRUs with a back-scattering behavior similar to their complex CAD models.

As a result, the proposed high-resolution RCS measurement techniques and utilized signal processing algorithms in this work were used to develop enhanced radar models of VRUs, especially highly realistic models for human motion. Moreover, those models can be amalgamated with realistic motion information of body parts. It is worth mentioning that the extracted radar data of the person in motion enables activity recognition, too. As the last point, the enhanced models can later be used for simulation of the radar wave propagation, which is necessary either for software-in-the-loop (SiL), hardware-in-the-loop (HiL), or vehicle-in-the-loop (ViL) testing of ADAS components.

The achievements in this thesis can be taken in several directions for further research. First, the extracted radar models can be employed in the pre-training for deep learning techniques, e.g., generative adversarial networks (GANs). The generated data by GANS technique not only prevent the extra costs, time, measurements, and labeling tasks but also avoid the overfitting problem caused by small data sets. The generated synthetic radar signatures can train the deep learning methods, e.g., convolutional neural network (CNN) and deep convolutional neural network (DCNN). Subsequently, the trained method reinforces the accuracy of target recognition and classification. As a further step, the extracted MoCap models even can be used to develop combined camera-radar models by assigning different colored or textured clothing to them. Those models are mandatory for validating and verifying the multi-sensor fusion systems, which combine camera and radar sensors. This kind of system is helpful for environment perception and increasing the accuracy of detecting and tracking objects in autonomous vehicles.

The achieved virtual scattering centers for VRUs can be implemented in the various wave propagation tools for full radar channel simulation of real traffic scenarios as another area of investigation. It is worth to repeat the same simulations with a different number of the extracted virtual scattering centers and additionally utilizing the deterministic model of each VRU. The radar channel characteristics can be calculated from the simulation results. Then, the accuracy of the simulations with the simplified models can be studied in comparison with the simulation with complex models. That helps to figure out the necessary number of the virtual scattering centers of the VRUs for approaching the similar accuracy of the simulation with the deterministic models and achieving a higher authenticity regarding real traffic scenarios.

A   Appendix

A.1   Technical Specification of Turn-tilt Table

Model	8MG-2SQ200-002
Kinematics and Feedback information	
Axis Ө Y	
Used stage	8MR190-90-4247
Travel range	360°
Maximal rotation speed	48°/s
Resolution in full step	0,6 arcmin (0.01°)
Axis Ө Z	
Used stage	8MR191-28
Travel range	360°
Manual Rotation Range	360°
Maximal rotation speed	60°/s
Resolution in full step	54 arcsec
Load and Transmision information	
Maximum load capacity	4 kg
Control and Communication	
Recommended controllers	8SMC4-USB
Recommended power supply	PUP120-17 (36 V)
Connector	HDB15(M)
Cable length (8MR190-90-4247)	1.6 m
Cable length (8MR191-28)	1.6 m
Additional Details	
System dimensions	468 x 205 x 282 mm
Measurement system	Metric
Weight	10 kg

Figure A.1: Technical specification of the embedded turn-tilt table in the RCU. It is a two-axis motorized turn-tilt table manufactured by STANDA UAB (https://www.standa.lt).
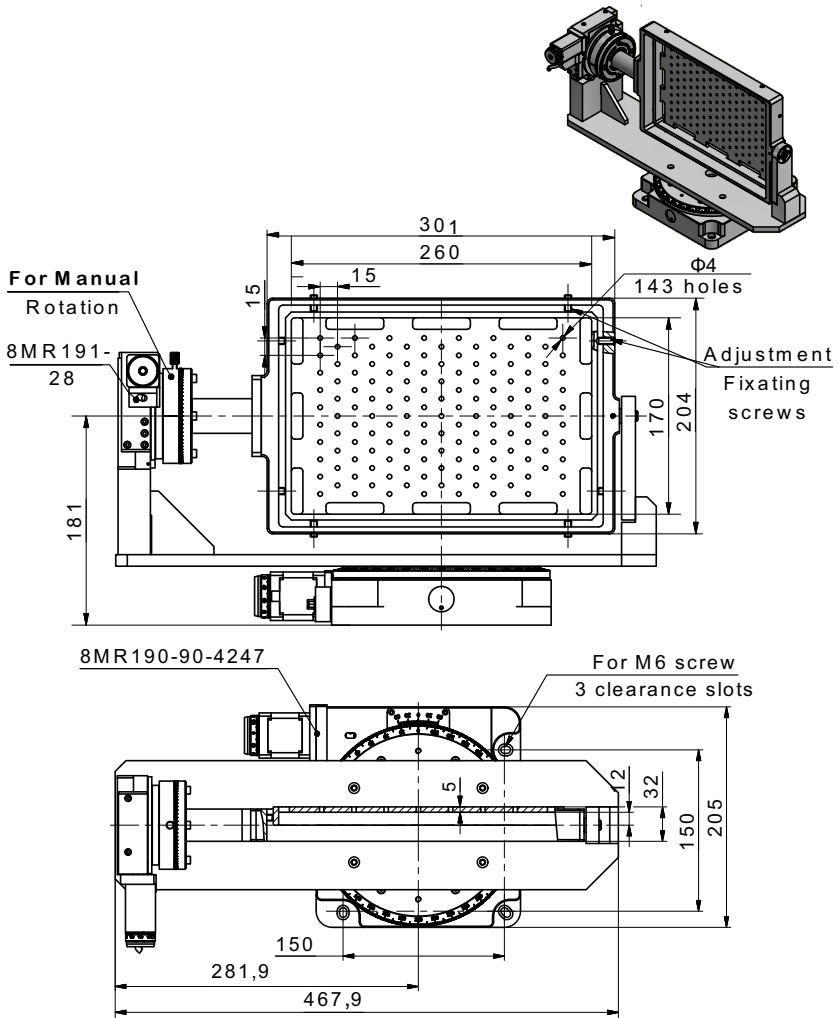
Figure A.2: Technical drawing specification of the embedded turn-tilt table. Dimensions are in mm.

A.2 Technical Specification of Rotating Stage

A sturdy turntable is used for preparing the rotating stage in the high-resolution measurement setup. The technical and drawing specification of the sturdy turntable is presented in Figures A.3 and A.4, respectively. Then, it is optimized by embedding a hybrid stepper motor (QSH4218) from Reichelt for microstepping. Furthermore, an inductive sensor is used for referencing the rotating stage position in 0°.

Max. centrical load	**500/750 kg (standing), 150 kg (hanging)**
Carrying plate diameter	**Ø 40 cm**
Max. diameter presentation disc (advice)	**Ø 125 cm**
Overall height	**12.5 cm**
Dead weight	**22 kg / 24 kg**
Housing material	**Metal construction galvanized (hollow shaft Ø 42 mm)**
Power consumption	**14 Watt**
Power supply	**Operates on 230V (grounded plug with 2 m cord)**
Suitable for outdoor use?	**Optional**
Collecting ring	**Optionally up to 900 W, 4 A**
Rotation speed	**1.0 rotation/minute**
Direction	**Clockwise (clockwise/counter-clockwise switch optional)**
Possible application	**Standing, Hanging**

Figure A.3: Technical specification of the implemented sturdy turntable in the rotating stage of the high-resolution measurement setup. It is manufactured by Pre-Motion presentation systems B.V. (https://www.pre-motion.com).

Turntable MAX 500 - 750 kg

Electric turntable with a maximum load of 500 kg or 750 kg

PRE·MOTION

Specifications
- Diameter: Ø 400 mm
- Height: 125 mm
- Dead weight: 22 kg (without collecting ring) or 24 kg (with collecting ring)
- Housing material: metal construction galvanized
- Speed: 1.0 rotation/min
- Direction: clockwise
- Power consumption: 14 W
- Power supply: 230 VAC, 50 Hz
- Length of grounded plug with cord: 2 metres
- Provided with 6 holes for mounting a presentation disc
- Provided with a slipper clutch
- Hanging or wall-mounted the max. carrying capacity is 150 kg

Types
- MAX 500 kg
- MAX 750 kg

Options
- On-board sliding contact (230 VAC, 900 W, 4 A)
- Various deluxe finishes available (MDF presentation disc, LED lighting or wooden frame)
- Clockwise/counter-clockwise switch
- Outdoor use
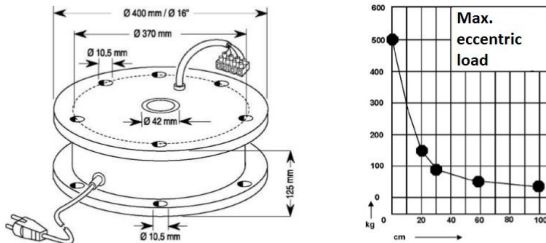
Figure A.4: Technical drawing specification of the implemented sturdy turntable in the rotating stage of the high-resolution measurement setup. Dimensions are in mm (https://www.pre-motion.com).

Figure A.5 shows the implementation of the stepper motor and reference switch inside the structure of the utilized sturdy turntable to have a motorized rotating stage with a favorite resolution angle. The technical specification of the stepper motor and sensor are shown in Figures A.6 and A.7, respectively.

(a)   (b)
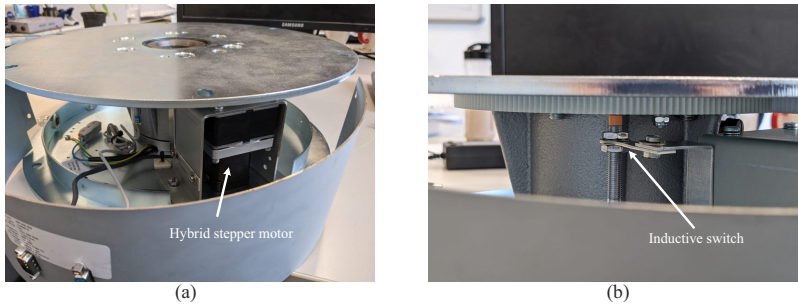
Figure A.5: The optimization process of the sturdy turntable with implementing (a) a hybrid stepper motor and (b) an inductive switch for referencing the start point of the rotating stage.

Product Name	Inductive Proximity Switch
Model	LJ8A3-2-Z/BX
Theory	Inductive Sensor
Wire Type	3 Wire Type (Brown, Blue, Black)
Switch Appearance Type	Cylinder Type, Metal Shell
Output Type	NPN, NO(Normal Open)
Detection Distance	2mm +/- 10%
Electrical Voltage	6-36 V DC
Set Distance	0~1.6mm
Output Current (max)	200mA
Detect objects	Iron
Standard Detection Object	Iron 12x12x1mm
Response Frequency	DC 0.5kHz , AC 25Hz
Column Sensor Diameter	8mm
Thread Diameter	8mm
Total Size	51x8 mm (L * D)
Cable Length	1.24m
External Material	Plastic, Metal
Color	Silver Tone, Gray, Yellow

Figure A.6: Technical specification of the implemented inductive sensor for referencing the rotating stage. The input voltage of the sensor in setup is 5 V (www.ekt2.com).

131

Specifications	Parameter	Units	QSH4218		
			-35-10-027	-41-10-035	-51-10-049
Rated Voltage	V_{RATED}	V	5.3	4.5	5.0
Rated Phase Current	$I_{RMS\ RATED}$	A	1.0	1.0	1.0
Phase Resistance at 20°C	R_{COIL}	Ω	5.3	4.5	5.0
Phase Inductance (typ.)		mH	6.6	7.5	8.0
Holding Torque (typ.)		Ncm	27	35	49
		oz in	38	50	69
Detent Torque		Ncm			
Rotor Inertia		g cm²	35	54	68
Weight (Mass)		Kg	0.22	0.28	0.35
Insulation Class			B	B	B
Insulation Resistance		Ω	100M	100M	100M
Dialectic Strength (for one minute)		VAC	500	500	500
Connection Wires		N°	4	4	4
Max applicable Voltage		V	48	48	48
Step Angle		°	1.8	1.8	1.8
Step angle Accuracy (max.)		%	5	5	5
Flange Size (max.)		mm	42.3	42.3	42.3
Motor Length (max.)	L_{MAX}	mm	34.5	39	49
Rear shaft hole depth		mm	5.0	5.0	5.0
Rear shaft hole diameter		mm	3.0	3.0	3.0
Axis Diameter		mm	5.0	5.0	5.0
Axis Length (typ.)		mm	20.0	20.0	20.0
Axis D-cut (0.5mm depth)		mm	15.0	15.0	15.0
Shaft Radial Play (450g load)		mm	0.02	0.02	0.02
Shaft Axial Play (450g load)		mm	0.08	0.08	0.08
Maximum Radial Force (20 mm from front flange)		N	28	28	28
Maximum Axial Force		N	10	10	10
Ambient Temperature		°C	-20..+50	-20..+50	-20..+50
Temp Rise (rated current, 2phase on)		°C	max. 80	max. 80	max. 80
Related Trinamic PANdrive		type	PD1-xxx-42	PD2-xxx-42	PD3-xxx-42

Figure A.7: Technical specification of the implemented stepper motor in the structure of the sturdy turntable to motorize the rotating stage (https://www.reichelt.de).

Figure A.8: Technical drawing specification of the implemented stepper motor in the structure of the sturdy turntable to motorize the rotating stage. Dimensions are in mm (https://www.reichelt.de).

List of Figures

List of Tables

Bibliography

[AJG00]   R. Abou-Jaoude and M. Grace. Test systems for automotive ra-
            dar. In *IEEE 51st Vehicular Technology Conference Proceedings
            (VTC)*, volume 1, pages 492–495, 2000.

[AOK19]   Ibrahim Alnujaim, Daegun Oh, and Youngwook Kim. Generative
            Adversarial Networks to Augment Micro-Doppler Signatures for
            the Classification of Human Activity. In *IEEE International
            Geoscience and Remote Sensing Symposium (IGARSS)*, pages
            9459–9461, Nov. 2019.

[ARMSF18]   Aleksandar Angelov, Andrew Robertson, Roderick Murray-
            Smith, and Francesco Fioranelli. Practical Classification of Dif-
            ferent Moving Targets Using Automotive Radar and Deep Neural
            Networks. *IET Radar, Sonar & Navigation*, 12(10):1082–1089,
            Oct. 2018.

[ASP+14]   Serdal Ayhan, Steffen Scherr, Philipp Pahl, Thorsten Kayser, Ma-
            rio Pauli, and Thomas Zwick. High-accuracy Range Detection
            Radar Sensor for Hydraulic Cylinders. *IEEE Sensors Journal*,
            14(3):734–746, Oct. 2014.

[ASW20]   Muhammad Arsalan, Avik Santra, and Christoph Will. Improved
            contactless heartbeat estimation in FMCW radar via kalman filter
            tracking. *IEEE Sensors Letters*, 4(5):1–4, Mar. 2020.

[AVC+14]   Andrei Anghel, Gabriel Vasile, Remus Cacoveanu, Cornel Ioana,
            and Silviu Ciochina. Short-Range Wideband FMCW Radar for
            Millimetric Displacement Measurements. *IEEE Transactions on
            Geoscience and Remote Sensing*, 52(9):5633–5642, Jan. 2014.

[AWE22]   Xin An, Jens Wagner, and Frank Ellinger. An integrated pri-
            mary impulse radio ultra-wideband radar for short-range real-
            time localization. *IEEE Transactions on Circuits and Systems*,
            69(8):3190–3201, Apr. 2022.

[Bal05]   Constantine A Balanis. *Antenna Theory: Analysis and Design, Third Edition*. New York: Wiley-Interscience, Jan. 2005.

[Bal12]   Constantine A Balanis. *Advanced Engineering Electromagnetics, Second Edition*. New York: John Wiley & Sons, Jan. 2012.

[BC16]   Domenic Belgiovane and Chi-Chih Chen. Bicycles and human riders backscattering at 77 ghz for automotive radar. In *10th European Conference on Antennas and Propagation (EuCAP)*, pages 1–5, 2016.

[BCC+14]   D. Belgiovane, C. Chen, M. Chen, S. Y. Chien, and R. Sherony. 77 GHz radar scattering properties of pedestrians. In *IEEE Radar Conference*, pages 735–738. IEEE, May 2014.

[BE08]   H. Buddendick and T.F. Eibert. Simplified Modeling of Complex Shaped Objects Using Scattering Center Distributions and Ray Optics. In *IEEE Antennas and Propagation Society International Symposium(APS)*, pages 1–4, Aug. 2008.

[BE10]   H. Buddendick and T. F. Eibert. Acceleration of Ray-Based Radar Cross Section Predictions Using Monostatic-Bistatic Equivalence. *IEEE Transactions on Antennas and Propagation*, 58(2):531–539, Feb. 2010.

[BE12]   H. Buddendick and T. F. Eibert. Incoherent scattering-center representations and parameterizations for automobiles. *IEEE Antennas and Propagation Magazine*, 54(1):140–148, Feb. 2012.

[BGSC10]   V.G. Borkar, A. Ghosh, R.K. Singh, and N. Chourasia. Radar cross-section measurement techniques. *Defence Science Journal*, 60(1):204–212, Mar. 2010.

[BL96]   R. Bhalla and Hao Ling. Three-dimensional scattering center extraction using the shooting and bouncing ray technique. *IEEE Transactions on Antennas and Propagation*, 44(11):1445–1453, Nov. 1996.

[Cal]   Calibration.   [Online].   Available: https://v22.wiki.optitrack.com/index.php?title=Calibration.

[CC14]   M. Chen and C. Chen. RCS Patterns of Pedestrians at 76-77 GHz. *IEEE Antennas and Propagation Magazine*, 56(4):252–263, Aug. 2014.

[CCX⁺20] Y. Chen, S. Chen, T. Xiao, S. Zhang, Q. Hou, and N. Zheng. Mixed Test Environment-based Vehicle-in-the-loop Validation - A New Testing Approach for Autonomous Vehicles. In *IEEE Intelligent Vehicles Symposium (IV)*, pages 1283–1289. IEEE, Oct. 2020.

[CGS21] X. Cai, M. Giallorenzo, and K. Sarabandi. Machine Learning-Based Target Classification for MMW Radar in Autonomous Driving. *IEEE Transactions on Intelligent Vehicles*, pages 1–1, Jan. 2021.

[CH02] C.K. Cheung and J.E.L. Hollis. A new 3d ray-tracing propagation model. In *Third International Conference on 3G Mobile Communication Technologies*, pages 201–205, May. 2002.

[Che08] V.C. Chen. Doppler Signatures of Radar Backscattering from Objects with Micro-motions. *IET Signal Processing*, 2:291–300(9), Sep. 2008.

[Chi23] Ushemadzoro Chipengo. High Fidelity Physics-Based Simulation of a 512-Channel 4D-Radar Sensor for Automotive Applications. *IEEE Access*, 11:15242–15251, Feb. 2023.

[CJ95] S. H. Chen and S. K. Jeng. An sbr/image approach for indoor radio propagation in a corridor. *IEICE Transactions Electron*, E78-C(8):1058–1062, Oct. 1995.

[CJ96] Shin-Hon Chen and Shyh-Kang Jeng. Sbr image approach for radio wave propagation in tunnels with and without traffic. *IEEE Transactions on Vehicular Technology*, 45(3):570–578, Aug. 1996.

[CKC13] M. Chen, M. Kuloglu, and C. Chen. Numerical study of pedestrian RCS at 76–77 GHz. In *Proceeding IEEE Antennas and Propagation Society International Symposium (APSURSI)*, pages 1982–1983, Jul. 2013.

[CKCP18] Stefano M. Canta, Robert A. Kipp, Shawn Carpenter, and L. E. Rickard Petersson. Range-doppler radar signature prediction of wind turbine using sbr. In *12th European Conference on Antennas and Propagation (EuCAP 2018)*, pages 1–4, Dec. 2018.

[CLHW06] V.C. Chen, F. Li, S.-S. Ho, and H. Wechsler. Micro-Doppler Effect in Radar: Phenomenon, Model, and Simulation Study. *IEEE*

Transactions on Aerospace and Electronic Systems, 42(1):2–21, 2006.

[CLR01]   Thomas H Cormen, Charles E Leiserson, and Ronald L Rivest. *Introduction to Algorithms , Second Edition*. Cambridge, Mass: MIT Press, 2001.

[CSC20]   Ushemadzoro Chipengo, Arien Sligar, and Shawn Carpenter. High fidelity physics simulation of 128 channel mimo sensor for 77ghz automotive radar. *IEEE Access*, 8:160643–160652, Sep. 2020.

[CSCL21] Yuwei Cheng, Jingran Su, Hongyu Chen, and Yimin Liu. A new automotive radar 4d point clouds detector by using deep learning. In *IEEE International Conference on Acoustics, Speech and Signal Processing (ICASSP)*, pages 8398–8402, May 2021.

[CWZ+21] Hang Cui, Junzhe Wu, Jiaming Zhang, Girish Chowdhary, and William R. Norris. 3d detection and tracking for on-road vehicles with a monovision camera and dual low-cost 4d mmwave radars. In *IEEE International Intelligent Transportation Systems Conference (ITSC)*, pages 2931–2937, Sep. 2021.

[DAB+14] Juergen Dickmann, Nils Appenrodt, Hans-Ludwig Bloecher, C. Brenk, Thomas Hackbarth, Markus Hahn, Jens Klappstein, Marc Muntzinger, and Alfons Sailer. Radar contribution to highly automated driving. In *Proceeding 44th European Microwave Conference (EuMC)*, pages 1715–1718, 2014.

[DFW18]   Rui Du, Yangyu Fan, and Jianshu Wang. Pedestrian and Bicyclist Identification Through Micro Doppler Signature With Different Approaching Aspect Angles. *IEEE Sensors Journal*, 18(9):3827–3835, Mar. 2018.

[DHR+20] Yoshana Deep, Patrick Held, Shobha Sundar Ram, Dagmar Steinhauser, Anshu Gupta, Frank Gruson, Andreas Koch, and Anirban Roy. Radar Cross-sections of Pedestrians at Automotive Radar Frequencies Using Ray tracing and Point Scatterer Modelling. *IET Radar, Sonar & Navigation*, 14(6):833–844, Jun. 2020.

[DKK+21] A. Diewald, C. Kurz, P. V. Kannan, M. Gießler, M. Pauli, B. Göttel, T. Kayser, F. Gauterin, and T. Zwick. Radar Target Simulation for Vehicle-in-the-Loop Testing. *Vehicles*, 3(2):257–271, May 2021.

[DMW18]   Thomas Dallmann, Jens-Kristian Mende, and Stefan Wald. ATRI-UM: A Radar Target Simulator for Complex Traffic Scenarios. In *MTT-S International Conference on Microwaves for Intelligent Mobility (ICMIM)*, pages 1–4, Apr. 2018.

[DSF+21]   Anand Dubey, Avik Santra, Jonas Fuchs, Maximilian Lübke, Robert Weigel, and Fabian Lurz. A bayesian framework for integrated deep metric learning and tracking of vulnerable road users using automotive radars. *IEEE Access*, 9:68758–68777, 2021.

[DSWW00]   D. Didascalou, T.M. Schafer, F. Weinmann, and W. Wiesbeck. Ray-density normalization for ray-optical wave propagation modeling in arbitrarily shaped tunnels. *IEEE Transactions on Antennas and Propagation*, 48(9):1316–1325, Sep. 2000.

[EGA19]   Baris Erol, Sevgi Z. Gurbuz, and Moeness G. Amin. GAN-based Synthetic Radar Micro-Doppler Augmentations for Improved Human Activity Recognition. In *IEEE Radar Conference (RadarConf)*, pages 1–5, Apr. 2019.

[FJM13]   GUASCH Joaquim FORTUNY and CHAREAU Jean-Marc. *Radar cross section measurements of pedestrian dummies and humans in the 24/77 GHz frequency bands: establishment of a reference library of RCS signatures of pedestrian dummies in the automotive radar bands*. Publications office of the European Union, 2013.

[FMKW06]   Thomas Fugen, Jurgen Maurer, Thorsten Kayser, and Werner Wiesbeck. Capability of 3-D Ray tracing for Defining Parameter Sets for the Specification of Future Mobile Communications Systems. *IEEE Transactions on Antennas and Propagation*, 54(11):3125–3137, Nov. 2006.

[GCB+13]   Kevin Geary, Joseph S. Colburn, Arthur Bekaryan, Shuqing Zeng, Bakhtiar Litkouhi, and Mohannad Murad. Automotive radar target characterization from 22 to 29 ghz and 76 to 81 ghz. In *IEEE Radar Conference (RadarCon13)*, pages 1–6, Apr. 2013.

[GD07]   Franceschetti Giorgio and Riccio Daniele. *Scattering, Natural Surfaces, and Fractals*. Academic Press, sep. 2007.

[GKZ+20]   M. Goldhammer, S. Köhler, S. Zernetsch, K. Doll, B. Sick, and K. Dietmayer. Intentions of Vulnerable Road Users—Detection

and Forecasting by Means of Machine Learning. *IEEE Transactions on Intelligent Transportation Systems*, 21(7):3035–3045, Jul. 2020.

[Gla89]   Andrew S. Glassner. *An Introduction to Ray Tracing*. Academic Press Ltd., 1989.

[GMR15]   V Geethanjali, Thushara Mohan, and I Srinivasa Rao. Beamforming networks to feed array antennas. *Indian Journal of Science and Technology*, 8(S2):78–81, Jan. 2015.

[HCC98]   Shi Cheng Hung, Chien Ching Chiu, and Chien Hung Chen. Wireless communication characteristics for tunnels with and without traffic. In *IEEE 1998 International Conference on Universal Personal Communications*, volume 1, pages 117–122 vol.1, Aug. 1998.

[HHD98]   I. Haritaoglu, D. Harwood, and L.S. Davis. W^4: Who? When? Where? What? A real time system for detecting and tracking people. In *Proceedings Third IEEE International Conference on Automatic Face and Gesture Recognition*, pages 222–227, Apr. 1998.

[IADW18]   Karim Ishak, Nils Appenrodt, Jrgen Dickmann, and Christian Waldschmidt. Human Motion Training Data Generation for Radar Based Deep Learning Applications. In *MTT-S International Conference on Microwaves for Intelligent Mobility (ICMIM)*, pages 1–4, Apr. 2018.

[IADW19]   Karim Ishak, Nils Appenrodt, Jürgen Dickmann, and Christian Waldschmidt. Advanced Radar Micro-Doppler Simulation Environment for Human Motion Applications. In *IEEE Radar Conference (RadarConf)*, pages 1–6, Sep. 2019.

[JBKP14]   Timo Jaeschke, Christian Bredendiek, Simon Küppers, and Nils Pohl. High-precision d-band fmcw-radar sensor based on a wideband sige-transceiver mmic. *IEEE Transactions on Microwave Theory and Techniques*, 62(12):3582–3597, Nov. 2014.

[JBY96]   S.X. Ju, M.J. Black, and Y. Yacoob. Cardboard people: a parameterized model of articulated image motion. In *Proceedings of the Second International Conference on Automatic Face and Gesture Recognition*, pages 38–44, Oct. 1996.

[JXP+22]   Mengjie Jiang, Gang Xu, Hao Pei, Hui Zhang, and Kunpeng
            Guo. High-resolution automotive radar point cloud imaging and
            processing. In *2022 Photonics & Electromagnetics Research
            Symposium (PIERS)*, pages 624–632, Apr. 2022.

[KGG+15]   Cesur Karabacak, Sevgi Z. Gurbuz, Ali C. Gurbuz, Mehmet B.
            Guldogan, Gustaf Hendeby, and Fredrik Gustafsson. Knowled-
            ge Exploitation for Human Micro-Doppler Classification. *IEEE
            Geoscience and Remote Sensing Letters*, 12(10):2125–2129, Jul.
            2015.

[KHBS13]   Mike Köhler, Jürgen Hasch, Hans Ludwig Blöcher, and Lorenz-
            Peter Schmidt. Feasibility of automotive radar at frequencies
            beyond 100 ghz. *International Journal of Microwave and Wire-
            less Technologies*, 5(1):49–54, Feb. 2013.

[Kle93]   K Klemenschits. *Mobile Communications in Tunnels*. University
            Wien, Austria, 1993.

[KPB+09]   Camilla Kärnfelt, Alain Péden, Ali Bazzi, Ghayath El Haj Shhadé,
            Mohamad Abbas, and Thierry Chonavel. 77 ghz acc radar simu-
            lation platform. In *9th International Conference on Intelligent
            Transport Systems Telecommunications, (ITST)*, pages 209–214,
            Oct. 2009.

[KW08]   Midori Kitagawa and Brain Windsor. *MoCap for Artists: Work-
            flow and Techniques for Motion Capture, First Edition*. Amster-
            dam: Elsevier/Focal Press, May. 2008.

[KW16]   P. Koopman and M. Wagner. Challenges in Autonomous Vehicle
            Testing and Validation. *SAE International Journal of Transpor-
            tation Safety*, 4(1):15–24, Apr. 2016.

[Lan02]   Édouard Lantéri. *Modelling : a guide for teachers and students*.
            Chapman & Hall Ltd., 1902.

[LKKL16]   Seongwook Lee, Seokhyun Kang, Seong-Cheol Kim, and Jae-
            Eun Lee. Radar cross section measurement with 77 ghz automo-
            tive fmcw radar. In *EEE 27th Annual International Symposium on
            Personal, Indoor, and Mobile Radio Communications (PIMRC)*,
            pages 1–6, Dec. 2016.

[LLHL16]   Jau-Jr Lin, Yuan-Ping Li, Wei-Chiang Hsu, and Ta-Sung Lee.
            Design of an FMCW radar baseband signal processing system
            for automotive application. *SpringerPlus*, 5(42), Jan. 2016.

[LS22] Yuanzhi Liu and Costas D. Sarris. Efficient propagation modeling for communication channels with reconfigurable intelligent surfaces. *IEEE Antennas and Wireless Propagation Letters*, pages 1–5, 2022.

[LSM+19] Gang Li, Yoke Leen Sit, Sarath Manchala, Tobias Kettner, Alicja Ossowska, Kevin Krupinski, Christian Sturm, and Urs Lubbert. Novel 4d 79 ghz radar concept for object detection and active safety applications. In *12th German Microwave Conference (GeMiC)*, pages 87–90, Mar. 2019.

[LYLK17] S. Lee, Y. J. Yoon, J. Lee, and S.C. Kim. Human–vehicle classification using feature-based SVM in 77-GHz automotive FMCW radar. *IET Radar, Sonar & Navigation*, 11(10):1589–1596, Aug. 2017.

[Mau05] J Maurer. *Strahlenoptisches Kanalmodell für die Fahrzeug-Fahrzeug- Funkkommunikation*. Karlsruhe university (TH), 2005.

[MBF+13] M. Murad, I. Bilik, M. Friesen, J. Nickolaou, J. Salinger, K. Geary, and J. S. Colburn. Requirements for next generation automotive radars. In *IEEE Radar Conference (RadarConf13)*, pages 1–6, 2013.

[MDW+18] Emidio Marchetti, Rui Du, Ben Willetts, Fatemeh Norouzian, Edward G. Hoare, Thuy Yung Tran, Nigel Clarke, Mikhail Cherniakov, and Marina Gashinova. Radar Cross-section of Pedestrians in the Low-THz Band. *IET Radar, Sonar & Navigation*, 12(10):1104–1113, Sep. 2018.

[Men11] Alberto Menache. *Understanding Motion Capture for Computer Animation, Second Edition*. Burlington, MA: Morgan kaufmann, Dec. 2011.

[MGLW15] M. Maurer, J. C. Gerdes, B. Lenz, and H. Winner. Autonomes Fahren - Technische, Rechtliche und Gesellschaftliche Aspekte. *Wiesbaden, Germany: Springer Vieweg*, May 2015. [Online]. Available: https://doi.org/10.1007/978-3-662-45854-9.

[MLD94] P. Mariage, M. Lienard, and P. Degauque. Theoretical and experimental approach of the propagation of high frequency waves in road tunnels. *IEEE Transactions on Antennas and Propagation*, 42(1):75–81, Jan. 1994.

[MMH18]   F. Michael Maier, Vamsi P Makkapati, and Martin Horn. Environ-
            ment Perception Simulation for Radar Stimulation in Automated
            Driving Function Testing. *e & i Elektrotechnik und Informations-
            technik*, 135(4):1613–7620, Aug. 2018.

[NHAZ21]   Alexandros Ninos, Jürgen Hasch, Mario Emilio Pizano Alvarez,
            and Thomas Zwick. Synthetic radar dataset generator for macro-
            gesture recognition. *IEEE Access*, 9:76576–76584, May. 2021.

[NWC+21]   Jia Niu, Ya Fei Wu, Yu Jian Cheng, Lun Wei Mou, Ting Jun Li,
            Hai Ning Yang, Shi Liang Pu, Lin Jie Shen, Lin Shen, and Tong
            Qian. A sparse array for 77 ghz 4d high-resolution imaging radar
            based on entropy model and convex optimization. In *2021 IEEE
            International Workshop on Electromagnetics: Applications and
            Student Innovation Competition (iWEM)*, volume volume1, pages
            1–3, Jun. 2021.

[NZ15]   Ram M. Narayanan and Matthew Zenaldin. Radar micro-Doppler
            Signatures of Various Human Activities. *IET Radar, Sonar &
            Navigation*, 9(9):1205–1215, Dec. 2015.

[Opt]   OptiTrack.   [Online].   Available:
            https://optitrack.com/cameras/primex-13/specs.html.

[Org18]   World Health Organization. *Global Status Report on Road Safety*.
            2018.

[PG18]   Peng Peng and Lixin Guo. A facet-based simulation of the mul-
            tipath effect on the em scattering and doppler spectrum of a low-
            flying target at maritime scene. *IEEE Geoscience and Remote
            Sensing Letters*, 15(10):1495–1499, Oct. 2018.

[PHO+18]   Robert Prophet, Marcel Hoffmann, Alicja Ossowska, Waqas Ma-
            lik, Christian Sturm, and Martin Vossiek. Pedestrian Classificati-
            on for 79 GHz Automotive Radar Systems. In *Proc. IEEE Intell.
            Vehicles Symp. (IV)*, pages 1265–1270, Jun. 2018.

[PJ12]   James Park and Joel T. Johnson. Measurements and Simulations
            of Multi-Frequency Human Radar Signatures. In *Proceedings
            of IEEE International Symposium on Antennas and Propagation*,
            pages 1–2, Jul. 2012.

[PJA12]   Nils Pohl, Timo Jaeschke, and Klaus Aufinger. An ultra-wideband
            80 ghz fmcw radar system using a sige bipolar transceiver chip

stabilized by a fractional-n pll synthesizer. *IEEE Transactions on Microwave Theory and Techniques*, 60(3):757–765, Jan. 2012.

[PJK+18]   N. Pohl, T. Jaeschke, S. Küppers, C. Bredendiek, and D. Nüßler. A compact ultra-wideband mmWave radar sensor at 80 GHz based on a SiGe transceiver chip (Focused session on highly-integrated millimeter-wave radar sensors in SiGe BiCMOS technologies). In *22nd International Microwave and Radar Conference (MIKON)*, pages 345–347. IEEE, May 2018.

[PJK+19]   L. Piotrowsky, T. Jaeschke, S. Kueppers, J. Siska, and N. Pohl. Enabling High Accuracy Distance Measurements With FMCW Radar Sensors. *IEEE Transactions on Microwave Theory and Techniques*, 67(12):5360–5371, Dec. 2019.

[PJM+12]   J. Park, J. T. Johnson, N. Majurec, M. Frankford, E. Culpepper, J. Reynolds, J. Tenbarge, and L. Westbrook. Software Defined Radar Studies of Human Motion Signatures. In *IEEE Radar Conference*, pages 0596–0601, Jun. 2012.

[PJM+14]   James Park, Joel T. Johnson, Ninoslav Majurec, Mark Frankford, Kyle Stewart, Graeme E. Smith, and Lamar Westbrook. Simulation and Analysis of Polarimetric Radar Signatures of Human Gaits. *IEEE Transactions on Aerospace and Electronic Systems*, 50(3):2164–2175, Dec. 2014.

[PMR17]   M. Pieraccini, L. Miccinesi, and N. Rojhani. RCS measurements and ISAR images of small UAVs. *IEEE Aerospace and Electronic Systems Magazine*, 32(9):28–32, Sep. 2017.

[PP21]   L. Piotrowsky and N. Pohl. Spatially Resolved Fast-Time Vibrometry Using Ultrawideband FMCW Radar Systems. *IEEE Transactions on Microwave Theory and Techniques*, 69(1):1082–1095, Jan. 2021.

[PRM+09]   Nils Pohl, Hans-Martin Rein, Thomas Musch, Klaus Aufinger, and Josef Hausner. Sige bipolar vco with ultra-wide tuning range at 80 ghz center frequency. *IEEE Journal of Solid-State Circuits*, 44(10):2655–2662, Sep. 2009.

[PSRB18]   R. Pérez, F. Schubert, R. Rasshofer, and E. Biebl. Single-Frame Vulnerable Road Users Classification with a 77 GHz FMCW Radar Sensor and a Convolutional Neural Network. In *19th*

International Radar Symposium (IRS), pages 1–10. IEEE, Jun. 2018.

[PTWM17]   S. M. Patole, M. Torlak, D. Wang, and A. Murtaza. Automotive radars: A review of signal processing techniques. *IEEE Signal Processing Magazine*, 34(2):22–35, Mar. 2017.

[PvD08]   F.C.A. Groen P. van Dorp. Feature-based human motion parameter estimation with radar. *IET Radar, Sonar & Navigation*, 2:135–145, Apr. 2008.

[Rem93]   Bernhard Rembold. Simulation of radio transmission in a tunnel. *Frequenz*, 47(11-12):270–275, Nov. 1993.

[RKK$^+$15]   Fabian Roos, Dominik Kellner, Jens Klappstein, Juergen Dickmann, Klaus Dietmayer, Klaus D. Muller-Glaser, and Christian Waldschmidt. Estimation of the orientation of vehicles in high-resolution radar images. In *2015 IEEE MTT-S International Conference on Microwaves for Intelligent Mobility (ICMIM)*, pages 1–4, Apr. 2015.

[RL08]   Shobha S. Ram and Hao Ling. Microdoppler signature simulation of computer animated human and animal motions. In *IEEE Antennas and Propagation Society International Symposium*, pages 1–4, Jul. 2008.

[RMGI22]   Angelica Reyes-Munoz and Juan Guerrero-Ibanez. Vulnerable road users and connected autonomous vehicles interaction: a survey. *ISensors (Basel)*, 22(12), Jun. 2022.

[RR19]   N. K. Ragesh and R. Rajesh. Pedestrian Detection in Automotive Safety: Understanding State-of-the-Art. *IEEE Access*, 7:47864–47890, Apr. 2019.

[RSH10]   M. A. Richards, J. A. Scheer, and W.A. Holm. *Principles of Modern Radar: Basic principles*. SciTech Publishing, Inc., . 2010.

[SBW08]   K. Schuler, D. Becker, and W. Wiesbeck. Extraction of Virtual Scattering Centers of Vehicles by Ray-Tracing Simulations. *IEEE Transactions on Antennas and Propagation*, 56(11):3543–3551, Nov. 2008.

[SEA06]   K. Sato, B. L. Evans, and J. K. Aggarwal. Designing an Embedded Video Processing Camera Using a 16-bit Microprocessor for a

151

Surveillance System. *Journal of VLSI Signal Processing*, 42:57–68, Oct. 2006.

[SFGT+11]   T. Schipper, J. Fortuny-Guasch, D. Tarchi, L. Reichardt, and Zwick T. RCS measurement results for automotive related objects at 23-27 GHz. In *Proceedings of the 5th European Conference on Antennas and Propagation (EUCAP)*, pages 683–686. IEEE, Apr. 2011.

[SHDW18]   O. Schumann, M. Hahn, J. Dickmann, and C. Wöhler. Semantic Segmentation on Radar Point Clouds. In *21st International Conference on Information Fusion (FUSION)*, pages 2179–2186. IEEE, Sep. 2018.

[SKM+13]   E. Schubert, M. Kunert, W. Menzel, J. Fortuny-Guasch, and J. Chareau. Human RCS measurements and dummy requirements for the assessment of radar based active pedestrian safety systems. In *14th International Radar Symposium (IRS)*, pages 752–757. IEEE, Jun. 2013.

[Sko01]   M.I. Skolnik. *Introduction to Radar Systems*. Electrical engineering series. McGraw-Hill, 2001.

[SMKM15]   Eugen Schubert, Frank Meinl, Martin Kunert, and Wolfgang Menzel. High resolution automotive radar measurements of vulnerable road users – pedestrians & cyclists. In *IEEE MTT-S International Conference on Microwaves for Intelligent Mobility (ICMIM)*, pages 1–4, Apr. 2015.

[SRDW22]   Dominik Schwarz, Nico Riese, Ines Dorsch, and Christian Waldschmidt. System performance of a 79 ghz high-resolution 4d imaging mimo radar with 1728 virtual channels. *IEEE Journal of Microwaves*, 2(4):637–647, Aug. 2022.

[SRL08]   Shobha Sundar Ram and Hao Ling. Simulation of human microDopplers using computer animation data. In *IEEE Radar Conference*, pages 1–6, May. 2008.

[SRV18]   Akash Deep Singh, Shobha Sundar Ram, and Shelly Vishwakarma. Simulation of the Radar Cross-section of Dynamic Human Motions Using Virtual Reality Data and Ray tracing. In *IEEE Radar Conference (RadarConf18)*, pages 1555–1560, Apr. 2018.

[SSGW21]   Pirmin Schoeder, Benedikt Schweizer, Alexander Grathwohl, and Christian Waldschmidt. Multitarget simulator for automotive ra-

dar sensors with unknown chirp-sequence modulation. *IEEE Microwave and Wireless Components Letters*, 31(9):1086–1089, Jun. 2021.

[SSM+17]   Martin Stolz, Eugen Schubert, Frank Meinl, Martin Kunert, and Wolfgang Menzel. Multi-target Reflection Point Model of Cyclists for Automotive Radar. In *14th European Radar Conference (EURAD)*, pages 94–97, Oct. 2017.

[SW09]   Christian Sturm and Werner Wiesbeck. Ray-tracing in a virtual drive for mobile communications. In *3rd European Conference on Antennas and Propagation*, pages 1937–1939, Jun. 2009.

[SWM+18]   Martin Stolz, Maximilian Wolf, Frank Meinl, Martin Kunert, and Wolfgang Menzel. A new antenna array and signal processing concept for an automotive 4d radar. In *15th European Radar Conference (EuRAD)*, pages 63–66, Sep. 2018.

[SZ21]   Shunqiao Sun and Yimin D. Zhang. 4D Automotive Radar Sensing for Autonomous Vehicles: A Sparsity-Oriented Approach. *IEEE Journal of Selected Topics in Signal Processing*, 15(4):879–891, May 2021.

[TEV13]   Karsten Thurn, Randolf Ebelt, and Martin Vossiek. Noise in homodyne fmcw radar systems and its effects on ranging precision. In *IEEE MTT-S International Microwave Symposium Digest (MTT)*, pages 1–3, Jun. 2013.

[Tic90]   T.E. Tice. An overview of radar cross section measurement techniques. *IEEE Transactions on Instrumentation and Measurement*, 39(1):205–207, Feb. 1990.

[TS88]   J. Tsao and B.D. Steinberg. Reduction of sidelobe and speckle artifacts in microwave imaging: the CLEAN technique. *IEEE Transactions on Antennas and Propagation*, 36(4):543–556, Apr. 1988.

[VDG03]   P. Van Dorp and F. C.A. Groen. Human walking estimation with radar. *IET Radar, Sonar & Navigation*, 150(5):356–365, Oct. 2003.

[WDW22]   S. Wald, T. Dallmann, and F. Weinmann. Ray-tracing-based micro-doppler simulation for 77 ghz automotive scenarios. In *18th European Radar Conference (EuRAD)*, pages 281–284, Apr. 2022.

[WG98]   Werner Wiesbeck and Norbert Geng. *Planungsmethoden für die Mobilkommunikation.* Berlin: Springer, sep. 1998.

[WGSW21]   Alexander Willecke, Keno Garlichs, Fynn Schulze, and Lars C. Wolf. Vulnerable road users are important as well: Persons in the collective perception service. In *IEEE Vehicular Networking Conference (VNC)*, pages 24–31, 2021.

[WM14]   Christian Waldschmidt and Holger Meinel. Future trends and directions in radar concerning the application for autonomous driving. In *Proceeding 44th European Microwave Conference (EuMC)*, pages 1719–1722, Oct. 2014.

[WMN+20]   Stefan Wald, Torsten Mathy, Sreejith Nair, Carlos Moreno Leon, and Thomas Dallmann. Atrium: Test environment for automotive radars. In *IEEE MTT-S International Conference on Microwaves for Intelligent Mobility (ICMIM)*, pages 1–4, Nov. 2020.

[WW19]   Stefan O. Wald and Frank Weinmann. Ray tracing for range-doppler simulation of 77 ghz automotive scenarios. In *13th European Conference on Antennas and Propagation (EuCAP)*, pages 1–4, Mar. 2019.

[YTN05]   N. Yamada, Y. Tanaka, and K. Nishikawa. Radar cross section for pedestrian in 76GHz band. In *35th European Microwave Conference (EuMC)*, pages 1018–10228. IEEE, Oct. 2005.

[ZCH+21]   Rui Zhou, Jixin Chen, Yan Huang, Gang Xu, Bangjie Zhang, Debin Hou, and Wei Hong. A two-chip cascaded fmcw radar for 2d angle estimation. In *2021 IEEE MTT-S International Wireless Symposium (IWS)*, pages 1–3, Aug. 2021.

[ZFW02]   T. Zwick, C. Fischer, and W. Wiesbeck. A stochastic multipath channel model including path directions for indoor environments. *IEEE Journal on Selected Areas in Communications*, 20(6):1178–1192, Aug. 2002.

[ZGWF22]   Liting Zhu, Xin Guo, Wen Wu, and Da-Gang Fang. One-dimensional high-gain beam-scanning transmitarray fed by phased array with continuous electronic scan and low scan loss. *IET Microwaves, Antennas & Propagation*, 16(7):465–476, Apr. 2022.

[ZHA+21]   Luoyan Zhu, Danping He, Bo Ai, Zhangdui Zhong, Fusheng Zhu, and Zhigang Wang. Measurement and ray-tracing simulation for

millimeter-wave automotive radar. In *IEEE 4th International Conference on Electronic Information and Communication Technology (ICEICT)*, pages 582–587, Sep. 2021.

[ZHK98]   Y.P. Zhang, Y. Hwang, and R.G. Kouyoumjian. Ray-optical prediction of radio-wave propagation characteristics in tunnel environments. 2. analysis and measurements. *IEEE Transactions on Antennas and Propagation*, 46(9):1337–1345, Sep. 1998.

Publications

Journal Publications

[1] S. Abadpour, S. Marahrens, M. Pauli, J. Siska, N. Pohl, and T. Zwick. Backscattering behavior of vulnerable road users based on high-resolution rcs measurements. *IEEE Transactions on Microwave Theory and Techniques (MTT)*, 70(3):1582–1593, Dec. 2021.

[2] S. Abadpour, M. Pauli, C. Schyr, F. Klein, R.Degen, J. Siska, N. Pohl, and T. Zwick. Angular resolved RCS and Doppler analysis of human body parts in motion. *IEEE Transactions on Microwave Theory and Techniques (MTT)*, 71(4):1761–1771, Nov. 2022.

[3] S. Abadpour, M. Pauli, J. Siska, N. Pohl, and T. Zwick. Comparative study of extracted high-resolution rcs models of motorcyclists in w-band. *Submitted in IEEE Microwave and Wireless Technology Letters (MWTL)*, ...(...), ... 2023.

Conference Publications

[4] S. Abadpour, A. Diewald, S. Marahrens, M. Pauli, and T. Zwick. Back Scattering of Traffic Participants Based on an Automotive Radar Measurement. In *2020 17th European Radar Conference (EuRAD)*, pages 99–102, Jan. 2020.

[5] S. Abadpour, A. Diewald, B. Nuss, M. Pauli, and T. Zwick. Extraction of Scattering Centers Using a Greedy Algorithm for Traffic Participants. In *2020 14th European Conference on Antennas and Propagation (EuCAP)*, pages 1–5, Mar. 2020.

[6] S. Abadpour, A. Diewald, M. Pauli, and T. Zwick. Extraction of Scattering Centers Using a 77 GHz FMCW Radar. In *2019 12th German Microwave Conference (GeMiC)*, pages 79–82, Mar. 2019.

[7] S. Abadpour, M. Pauli, M. Kretschmann, H. Igbal, P. Aust, and T. Zwick. Dielectric Material Characterization of Traffic Objects in Automotive Radar Applications. In *2023 17th European Conference on Antennas and Propagation (EuCAP)*, pages 1–5, Mar. 2023.

[8] S. Abadpour, M. Pauli, X. Long, and T. Zwick. Automotive radar channel simulation based on a high-resolution backscattering model of a motorcyclist. In *2023 IEEE Radio and Wireless Symposium (RWS)*, pages 48–51, Jan. 2023.

[9] S. Abadpour, M. Pauli, C. Schyr, F. Klein, R.Degen, , J. Siska, N. Pohl, and T. Zwick. Analyzing the Movement of Motorcyclist's Extremities based on its Angular Resolved RCS Measurement. In *2023 20th European Radar Conference (EuRAD) (Accepted)*, Sep. 2023.

[10] J. Kowalewski, I. Mehinovic, S. Abadpour, J. Mayer, and T. Zwick. A Pattern Reconfigurable Antenna System for Automotive MIMO Applications. In *2018 11th German Microwave Conference (GeMiC)*, pages 29–32, Mar. 2018.

[11] M. Pauli, S. Abadpour, A. Diewald, and T. Zwick. RCS Measurements for the Implementation in Radar Target Simulators. In *2021 International Conference on Electromagnetics in Advanced Applications (ICEAA)*, pages 311–311, Aug. 2021.

Die Bände sind unter www.ksp.kit.edu als PDF frei verfügbar oder als Druckausgabe bestellbar.

During the evolvement of autonomous driving technology, obtaining reliable 3-D environmental information is an indispensable task in approaching safe driving. The operational behavior of automotive radars can be precisely evaluated in an over-the-air vehicle-in-the-loop environment by modeling its surrounding, specifically vulnerable road users (VRUs), as realistic as the real test environment. Such a detailed model can be generated based on the radar cross section (RCS) and Doppler signatures of a VRU in different situations. This information can be retrieved by the collected radar data from high-resolution RCS measurements in the radial and angular domains. Therefore, this work proposes a high-resolution RCS measurement technique to determine the relevant scattering points of different VRUs with high radial and angular resolution to develop a realistic radar model of VRUs.

Sevda Abadpour joined the Institute of Radio Frequency Engineering and Electronics (IHE), Karlsruhe Institute of Technology (KIT), Karlsruhe, Germany, in 2017 to pursue a Ph.D. in electrical engineering. Her current research interests include automotive radar channel modeling and electromagnetic wave propagation. Her work focuses on RCS measurement for traffic participants and the development of radar models for the use in over-the-air (OTA) vehicle-in-the-loop (ViL) test method.